UNIVERSITY OF OKLAHOMA

GRADUATE COLLEGE

THERAPEUTIC APPLICATIONS OF BIOCONJUGATES IN HUMAN DISEASE

A DISSERTATION

SUBMITTED TO THE GRADUATE FACULTY

in partial fulfillment of the requirements for the

Degree of

Doctor of Philosophy

By

PATRICK HUGH MCKERNAN
Norman, Oklahoma
2018

THERAPEUTIC APPLICATIONS OF BIOCONJUGATES IN HUMAN DISEASE

A DISSERTATION APPROVED FOR THE
STEPHENSON SCHOOL OF BIOMEDICAL ENGINEERING

BY

____
Dr. Roger Harrison, Chair

____
Dr. Vassilios Sikavitsas

____
Dr. Edgar O’Rear

____
Dr. Matthias Nollert

____
Dr. Chuanbin Mao

Acknowledgements

I would like to thank my committee, Dr. Edgar O'Rear, Dr. Vassilios Sikavitsas, Dr. Matthias Nollert, Dr. Chuanbin Mao, and especially Dr. Roger Harrison. Thank you for your invaluable advice, kind words, and continual support the last four years. I would also like to thank the many collaborators who have contributed to these projects including Dr. Ricardo Prada Silvy and Dr. Rajagopal Ramesh. Furthermore, the work in this dissertation could not have been possible without the generous support and assistance of the Oklahoma Center for the Advancement of Science and Technology, the University of Oklahoma Office of Technology Development, the Jean Wheeler and Baxter Abbott Sparks Breast Cancer Research Fund, Stephenson Cancer Center, and the National Institute of Allergy and Infectious Disease's Biodefense and Emerging Infections Repository. Lastly, I would like to thank my all fellow colleagues, especially Needa, James, Cortez, and Julien; without your assistance and friendship I could not have succeeded.

Table of Contents

List of Figures

Chapter 1: Introduction

Targeted Delivery

Annexin A5

The unifying element tying together the therapeutics presented in this thesis is annexin A5. The protein, annexin 5 (ANXA5), is a membrane management protein that specifically binds to apoptotic cells. The natural ligand of ANXA5 displayed by apoptotic cells is phosphatidylserine. The aminophospholipid phosphatidylserine (Ptd-L-Ser) is a universal marker of mammalian cell stress. The expression of Ptd-L-Ser is triggered by a diverse range of cellular pathologies, most notably cellular trauma, oncogenesis, or infection. Annexin plays several critical roles in the pathogenicity of these disease states. Notably, members of the annexin family mediate coagulation, enable macrophage-dependent phagocytosis, and participate in immune cell activation [1, 2]. During participation in these biological processes, ANXA5 binds and recognizes Ptd-L-Ser in a Ca^{2+}-dependent manner [3, 4]. The unique bow shape of ANXA5, formed by 4 repeating domains of 5 alpha helixes each, facilitates the recruitment of calcium and the polymerization of ANXA5 trimers (Figure 1) [5]. Our previous work has demonstrated that ANXA5 derived therapeutics can be targeted to Ptd-L-Ser expression [6-8]. In this thesis I build on this work, targeting several novel bioconjugates to Ptd-L-Ser expression.

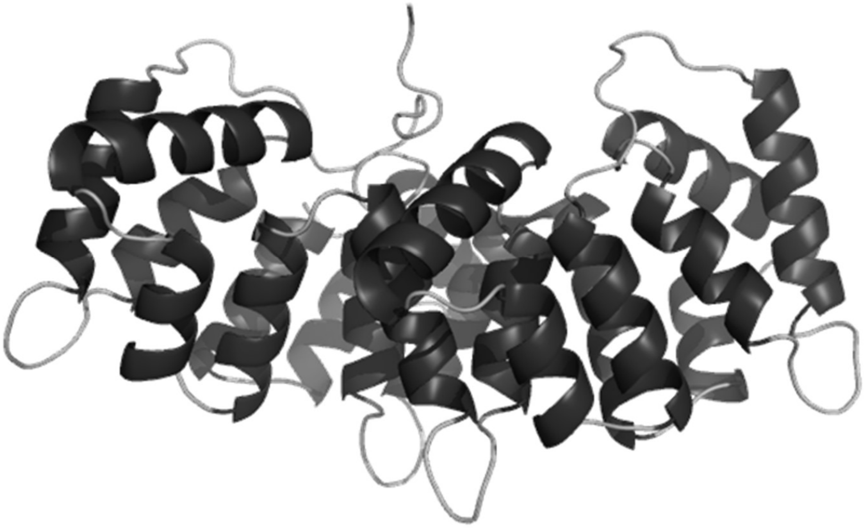

Figure 1: The structure of human annexin A5 protein from RCSB Protein Data Bank (www.rcsb.ord).

Phosphatidylserine

The aminophospholipid Ptd-L-Ser is an integral component of the eukaryotic plasma membrane. Sharing the hydrophilic phosphate head and twin hydrophobic fatty acid tails common to all phospholipids, Ptd-L-Ser can be differentiated from its lipid brethren by a single amino acid, serine, which caps the phosphate head (Figure 2). Unlike many phospholipids, the distribution of Ptd-L-Ser across the plasma membrane is not uniform. Ptd-L-Ser is sequestered solely to the inner leaflet of the plasma membrane of healthy cells by members of the flippase, floppase, and scramblase transporter families [9]. In a diverse range of cellular pathologies, most notably cellular trauma, oncogenesis\ or infection Ptd-L-Ser is translocated to the outer leaflet of the plasma membrane. There the expression of Ptd-L-Ser serves as a “dead man’s switch”, signaling that the cell is dying. The expression of Ptd-L-Ser on dying cells is recognized by host immune elements, triggering cell clearance by phagocytosis [1, 10, 11]. In contrast to its normal role as a mediator of the host immune system, Ptd-L-Ser expression is hijacked by many diseases to promote disease progression.

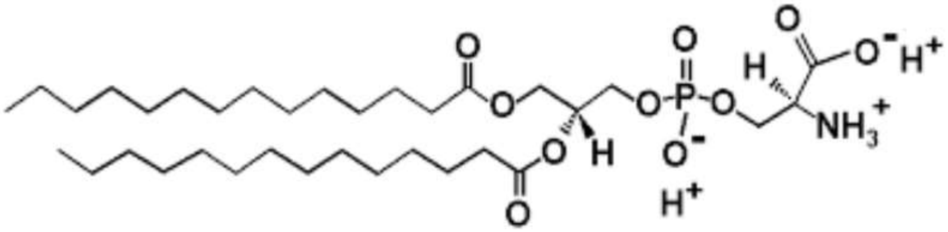

Figure 2: Phosphatidylserine (Ptd-L-Ser).

In cancer, the expression of Ptd-Ser is a necessary part of oncogenesis. All lethal tumors share several etiological hallmarks including: uncontrolled proliferation, failure of apoptosis, angiogenic activity, evasion of the immune system, and metastasis. One antigen intrinsically tied to each of these hallmarks is the membrane phospholipid Ptd-L-Ser. During oncogenesis, Ptd-L-Ser promotes uncontrolled proliferation through PI3K/Akt/mTOR activation [12, 13]. Furthermore, during oncogenesis Ptd-L-Ser expression mediates cell survival by blocking T-cell mediated apoptosis [14]. Additionally, Ptd-L-Ser expression promotes tumor growth by M2 macrophage dependent angiogenesis [15, 16]. In a similar manner, Ptd-L-Ser expression suppresses immune recognition of the tumor by promoting immunosuppressive phagocytosis [17]. Finally, phosphatidylserine promotes metastasis by increasing the fluidity of the cellular membrane [18-20].

In malaria, the expression of Ptd-L-Ser is a hallmark of cellular infection [21-23]. When the infected cell is damaged by parasite entry, host cell catabolism, and parasite replication, the damaged membrane expresses Ptd-L-Ser [24, 25]. The expression of Ptd-L-Ser is not only a byproduct of parasite growth, but an intentional survival strategy [9, 22, 26-28]. The expression of Ptd-L-Ser promotes parasite survival and disease progression. For instance, infected cells evade immune recognition by Ptd-L-Ser dependent-sequestration within the vascular endothelium [29, 30]. Furthermore, the increased expression of Ptd-L-Ser signals to the host immune system that the cell is undergoing orderly apoptosis, and encourages immune suppressing phagocytosis, in effect downregulating the host’s innate defenses against infection [11, 31].

Diseases of Interest

Malaria

Malaria is the single most deadly infectious disease, infecting 214 million individuals a year of which almost 438 thousand will die. Discounting direct mortality, malaria represents a significant burden on the health care system of many countries. In malaria endemic countries, malaria accounts for almost one half of all hospital visits [32, 33]. Compounding these issues is the spread of drug resistant malaria. Emerging strains of the Plasmodium parasite responsible for malaria are resistant to all known pharmaceutical treatments [34]. There is a significant need for new antimalarial therapeutics.

Malaria is an infection of the blood characterized by the invasion of host erythrocytes by parasites of the Plasmodium genus. The Plasmodium parasite undergoes a complex multistage lifecycle within its human host and its mosquito vector (Figure 3). In its human host, the parasite primarily infects cells within the blood (Figure 4).

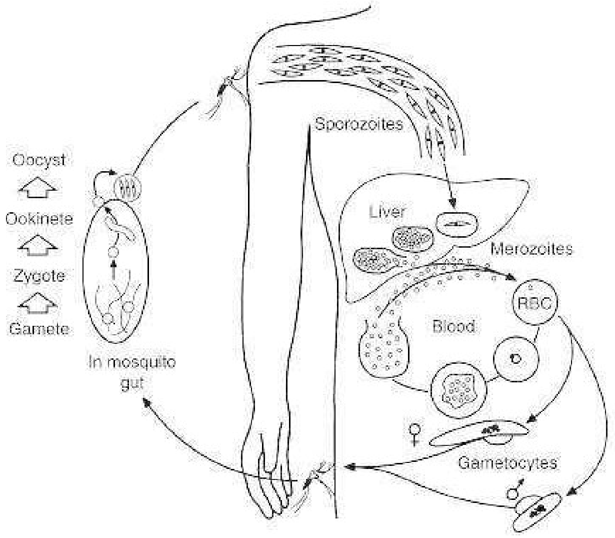

Figure 3: Lifecycle of the malaria parasite [35].

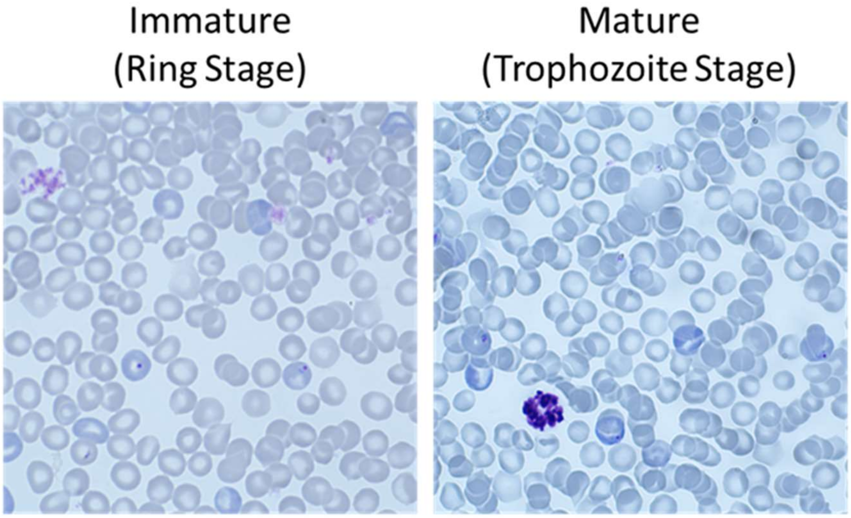
Immature (Ring Stage)

Mature (Trophozoite Stage)

Figure 4: Life stages of the malaria parasite. Giemsa stained blood slides of P. bergei infected BALB/cj mouse blood demonstrating two of the key stages of the plasmodium lifecycle. Young, ring-stage parasites (left) appear as small dots within erythrocytes. Mature parasites (right) appear as dark clusters within iRBC.

The lifecycle stages of the parasite within host erythrocytes are of prime clinical significance as this stage is responsible for the manifestation of disease symptoms and associated mortality [36, 37]. The parasite replicates solely within these host cells. Upon entry into a host erythrocyte, the Plasmodium parasite begins remodeling the cell, using the host cell as camouflage from the immune system, a source of food, and an incubator for its rapid replication [38]. Antimalarial drugs act on the parasite at this stage, while it is replicating within a host cell. Commercial antimalarial drugs exploit the physiological differences between the parasite and healthy cells. The vast majority of drugs interfere with parasite-host cell catabolism and inhibit parasite growth [39].

Breast Cancer

Breast cancer is the most commonly diagnosed cancer among women and is a leading cause of female mortality. When detected early on, patients have a 94% 5-year survival rate, which drops to only 10% once metastasis has occurred. In breast cancer, one of the most significant challenges with traditional treatment modalities is the efficient delivery of chemotherapeutics to the tumor. Less than 0.7% of the dose reaches the tumor [40, 41]. One promising field of anticancer research is the use of targeted biologics to deliver chemotherapeutics to the tumor.

Targeted biologics such as antibody-drug conjugates increase the dose of chemotherapeutic reaching the tumor.

Melanoma

Skin cancer is the most frequently diagnosed form of cancer. However, excepting melanoma, cancers of the skin are responsible for relatively few annual deaths (< 1, 000) [42-44]. Despite its infrequent appearance in dermatology, cutaneous malignant melanoma (CCM) represents the most frequent source of skin cancer related deaths. When CCM metastasizes, patient survival rates fall as low as 5%. Over the last half-decade rapid advances in biologic therapeutics have spawned a new generation of treatments, increasing patient survival and quality of life. A large body of work has focused on combinatorial therapies employing immunostimulation with traditional treatment modalities.

Lymphoma and leukemia

Hematological malignancies such as lymphoma and leukemia are unique among cancers. Typically originating from host immune cells, these malignancies do not form solid tumors, but rather form diffuse “liquid” tumors. Leukemia is the presentation of these cancerous cells within the blood. Lymphoma is the presentation of these cancerous cells within the lymphatic system. Leukemia can be categorized as acute or chronic depending on the time course of progression. Lymphoma can be categorized as Hodgkin’s or Non- Hodgkin’s Lymphoma.

Hodgkin's Lymphoma is characterized by the presence of abnormally large B-cells called Reed-Sternberg Cells, all other types of lymphoma are classified as Non-Hodgkin's Lymphoma.

Targeted Agents

Cystathionine-γ-lyase

The protein cystathionine-γ-lyase (CGL) is a metabolic enzyme with antimicrobial activity. As a key piece of the metabolic sulfur savaging pathway, CGL recycles thiol containing metabolites [45]. Additionally, our lab has undertaken several point mutations of CGL conferring additional methionine lyase activity. In previous work, cystathionine-γ-lyase E58N, R118L, and E338N mutations were introduced to impart nonnative methionine γ -lyase activity, resulting in broader enzyme substrate reactivity [8]. This mutant cystathionine-γ-lyase (mCGL) variant has been employed successfully by our lab in enzyme-prodrug therapy (EPT) along with the methionine analog selenomethionine (setmet)[6, 46]. In EPT, the nontoxic prodrug selenomethionine is converted into highly toxic species by mCGL methioninase activity, destroying target cells.

Single-Walled Carbon Nanotubes

Carbon nanotubes are a promising tool for photothermal tumor therapy due to their high stability, large surface area to weight ratio, and high thermal conductivity. It has been shown that about 84% of the heat generated by radiofrequency excitation within a nanotube is transmitted to its surrounding substrate [47-49]. This property of thermal dispersion can be utilized for cancer ablative therapies to cause temperature-based homeostatic disruption. Once the temperature of a cell rises above 47°C, irreversible cell death by ablation occurs which is characterized by cell necrosis and tissue coagulation [50, 51]. Nanotubes can be single-walled (SWCNTs) or multi-walled (MWCNTs). For a tumor ablative therapy, SWCNTs are preferred over MWCNTs. This electrostatic screening diminishes the incident field within the structure. Studies have shown that the dominant power dissipation from MWCNTs is due to the outermost shell, which results in significantly decreased absorption compared to SWCNTs [52].

Chlorambucil

Chlorambucil (CMB), is the one of the first successful chemotherapeutic drugs ever employed to treat cancer [53, 54]. In modern medicine CMB has remained the standard of care for leukemia for almost one century due to its potent antineoplastic activity and well documented safety [55, 56]. A mustard derivative, CMB, is an alkylating agent with significant reactivity to DNA [57-60]. While DNA interchelation is the primary mechanism of CMB induced apoptosis, to a lesser extent CMB is also capable of alkylating other cellular structures [61]. This process is limited by the formation of an aziridinium derivative of chlorambucil, a process highly dependent on pH [61, 62].

Ampicillin

The beta-lactam penicillin derivative, ampicillin (AMP), was discovered in 1958 by the addition of a single amino group to a benzylpenicillin [63-65]. In contrast to traditional antibiotics such as penicillin, this new therapeutic was active against both gram-positive and gram-negative bacteria. The unexpected gram-negative activity and wide spectrum of antibacterial activity helped to establish AMP as the first choice for the treatment of many diseases including S. aureus, E. coli, H. influenzae and S. pneumoniae. Most notably, AMP is used to treat whooping cough, typhoid fever, and bacterial meningitis. AMP works primarily through suicide inhibition of bacterial transpeptidases, where it covalently modifies a crucial catalytic amino acid residue.

Carboplatin

Discovered in 1972, the bidentate, cyclobutene dicarboxylic acid derivative of platinum, carboplatin, is the standard of care for treating many forms of cancer [66]. Carboplatin is of prime clinical significance due to its remarkably broad anticancer activity in multiple forms of cancer. Synthesized from cisplatin, carboplatin is well tolerated compared to other platinum agents which can be some of the most toxic commercially available chemotherapeutics. Carboplatin's primary mechanism of action is DNA alkylation. Despite its frequent clinical use, carboplatin suffers from significant side effects, and only marginal increases in prognosis.

Scope of Thesis

Bioconjugates are a rapidly growing group of biologically active therapeutics employed in many biomedical disciplines. These therapeutics are synthesized by conjoining biomolecules with agents such as drugs, toxins, or other biomolecules. In much the same way as a complex machine is merely an amalgamation of simple parts, bioconjugates are an amalgamation of simple molecules, and the resulting products are more than the sum of their parts. Bioconjugates consisting of simple molecules can perform novel complex biological functions. This dissertation will be organized into four main chapters titled as follows:

(1) Photothermal Therapy Combined with Checkpoint Inhibition in Cancer Treatment

(2) Antimalarial Activity of Chimeric Fusion Protein

(3) A Novel Cytostatic Drug-Protein Bioconjugate Consisting of Annexin A5 and Chlorambucil

(4) Preliminary Work
    A) Heating of Single-Walled Carbon Nanotubes by Very High Frequency Radiation
    B) Synergistic Enhancement of the Antineoplastic Activity of Docetaxel by Single-Walled Carbon Nanotubes
    C) Interaction of Annexin A5 and Drug Resistance in the Presence of the Selecting Drug
    D) Bactericidal Activity of a Novel Protein-Antibiotic Bioconjugate Consisting of Ampicillin and Annexin A5
    E) A Novel Antineoplastic Drug-Protein Bioconjugate Consisting of Carboplatin and Annexin A5

Chapter 2: Photothermal Therapy Combined with Checkpoint Inhibition in Cancer Treatment

Abstract

The selective near-infrared photothermal ablation of EMT-6 tumors with annexin A5 (ANXA5) functionalized single-walled carbon nanotubes (SWCNT) synergistically enhances an anti-CTLA-4 dependent abscopal response. We confirm the selective accumulation of ANXA5-SWCNT in tumor vasculature by fluorescent spectroscopy, and the resulting targeted SWCNT-dependent near-infrared ablation of tumors using thermal imaging. We then demonstrate the synergism between this targeted photothermal ablation modality and immunostimulation in several models of invasive metastatic cancer. Notably in the orthotopic EMT6 model of breast cancer, we observe a synergistic decrease in tumor regrowth and a corresponding increase in survival following the combination of SWCNT-ANXA5 targeted photothermal ablation and anti-CTLA-4 checkpoint inhibition. We observe an increase in splenocytes of the cytolytic CD8(+) T-cell and helper CD4(+) T-cell lineages in mice receiving the combinatorial therapy, may explain both the enhanced tumor rejection and increased survival via an abscopal response.

Introduction

Breast cancer is one of the most lethal forms of cancer, especially in woman, where it is responsible for more deaths than any other form of cancer. When breast cancer metastasizes, patient five-year survival rates fall below 25 percent. Over the last half-decade rapid advances in biologic therapeutics and nanotechnology have spawned a new generation of treatment options providing a rich opportunity to investigate combinatorial therapies. We investigate the combination of selective photothermal ablation and checkpoint inhibition in several models of metastatic cancer. By employing a recombinant protein-nanotube conjugate, consisting of single-walled carbon nanotubes (SWCNTs) and the tumor targeting protein annexin A5 (AXNA5) we selectively target tumor tissue for photothermal ablation using near-infrared (NIR) laser light.

Photothermal ablation is the use of light to heat tissue above 60 °C. Exposure to high temperatures leads to tissue death via necrosis and can be used as an alternative treatment modality for drug resistant tumors. A previous study comparing the response of breast cancer to hyperthermia (39 – 45 °C), a slow heating of tissue, versus ablation showed that ablation temperatures were able to eradicate hyperthermia resistive tumors.

One promising development in the treatment of tumors by ablation is the use of SWCNTs in conjunction with irradiation. SWCNTs are gaining more attention as versatile nanoparticles in diagnostics and therapeutics for drug delivery, photodynamic therapy, and NIR contrast enhancement. SWCNTs have an intrinsic excitation in the NIR range (700–1100 nm). This excitation heats the surrounding tissue inducing cell death via coagulative necrosis, rupturing of cell membranes, and denaturing of proteins. The use of NIR ablation with nanotubes is further enhanced by the presence of a the "biological window", where light easily penetrates several millimeters into tissue.

Harnessing the phosphatidylserine (Ptd-L-Ser) ligand, annexin A5 (ANXA5), we direct a single-walled nanotube-protein conjugate (SWCNT-ANXA5) to Ptd-L-Ser expressing tumor vasculature. The SWCNT-ANXA5 conjugate is generated by conjugating ANXA5 to a SWCNT backbone via a heterobifunctional DSPEG-PEG-malameide linker (Figure 6).

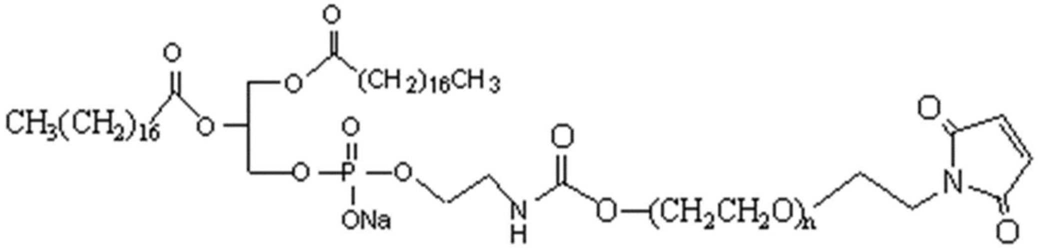

Figure 5: DSPE-PEG-Mal linker.

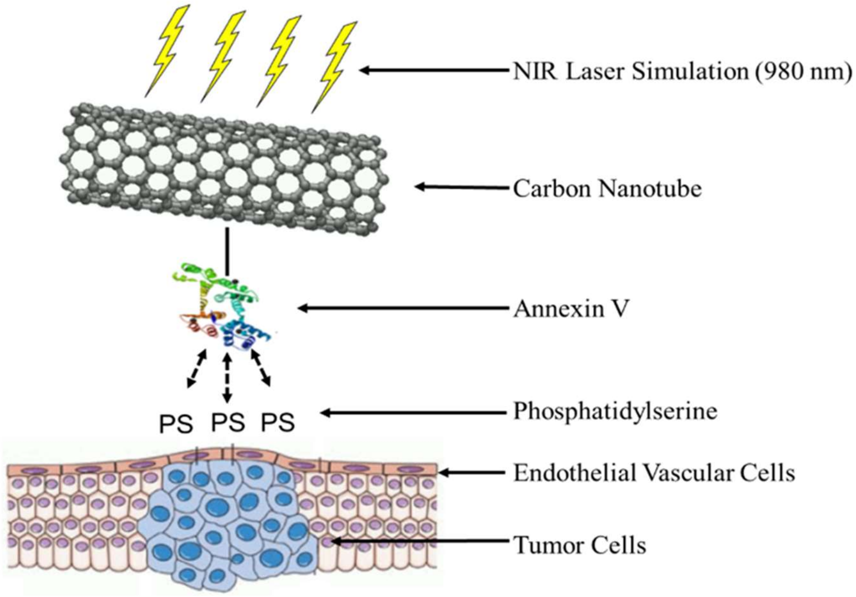

Figure 6: The therapeutic overview of SWCNT photo-ablative therapy. Nanotubes introduced to the blood stream accumulate to Ptd-L-Ser expressing tumor cells and tumor vasculature by ANXA5 dependent binding.

We develop the resulting ANXA5-SWCNT conjugate as part of a photothermal therapeutic modality in vivo in the B16F10 melanoma, 4T1 breast cancer and EMT6 breast cancer cell lines. We further expand on this treatment with the synergistic addition the immunostimlants anti-PD-1, anti-CD-73, anti-CTL-4.

Carbon Nanotubes

While primarily classified as either single-walled (SWCNTs) or multi-walled (MWCNTs), nanotubes can be further characterized by their diameter. Carbon nanotubes can be imagined as sheets of graphene rolled into a tube. Since graphene has a stereospecific structure, the angle at which the carbon nano*tube* is rolled determines the diameter of the sheet. Additionally, since the sheet is comprised of individual ridged bonds of carbon, the diameter of the tube can only decrease or increase by some factor of a carbon bond length and rolling angle [67]. The diameter equation uses the chirality values ‘m’ and ‘n’, where ‘n’ and ‘m’ are the number of hexagonal units along the graphene sheet in two opposite direction. The addition of these vectors represents the imaginary circumference of the carbon nanotube. Diameter can be calculated from chirality according to the following formula.

$$d = 0.0783 * (n^2 + m^2 + nm)^{0.5}$$

SWCNTs have diameters ranging from 0.4 to 2 nm, while MWCNTs have diameters from 1 to 100 nm with wall thicknesses of 0.2 to 2 nm [68, 69]. Nanotubes chirality can be further distinguished based on their chirality into zigzag, armchair, and chiral. Zigzag nanotubes occur when m = 0 and the sheet is rolled along the n-axis. Armchair nanotubes occur when m = n. Chiral nanotubes such as the 6,5-single walled nanotubes employed in this study occur when m ≠ n. The chiral diameter of a carbon nanotube has a huge influence on the nanoparticle's physical properties. For instance, chirality determines if a carbon nanotube is a semiconductor or a metal [69]. The 6,5-SWCNTs employed in this study are semiconductors. More detailed analysis of the chirality, size, and composition of the SWCNT employed in this study can be found in the Appendix D and E.

Materials and Methods

Materials

The AXA5 vector was constructed as part of a pET-30 Ek/LIC plasmid previously, using Gibson fragment assembly cloning[70]. Bovine serum albumin (BSA), Triton X-100, EDTA, β-mercaptoethanol, PMSF, and Tris-acetate-EDTA buffer were from Sigma-Aldrich (St Louis, MO). Sodium phosphate and sodium dodecyl sulfate (SDS) were from Mallinckrodt Chemicals (Phillipsburg, NJ). HPLC grade ethanol was from Acros Organics (Waltham, MA). His-trap columns were from GE Healthcare (Chicago, IL). Flow cytometry staining buffer, fixation/permeabilization buffer, permeabilization buffer, and Slide-A-Lyzer dialysis cassettes (3.5 kDa) were from Thermo Fisher Scientific (Waltham, MA). The 2 and 100 kDa dialysis membranes were from Spectrum Laboratories (Rancho Dominguez, CA). Roswell Park Memorial Institute cell medium (RPMI-1640) and Hank's balanced salt solution were from ATCC (Manassas, VA). Fetal bovine serum (FBS) was from Atlanta Biologicals (Lawrenceville, GA). Tryptone, yeast extract, and kanamycin monosulfate were obtained from Alfa Aesar (Ward Hill, MA). Sodium hydroxide, potassium chloride, and sodium chloride were from VWR Inc (Radnor, PA). HRV-C3 protease was from Sino biologics (Portland, OR). All antibodies were obtained from Biolegend (San Diego, Ca. Single-walled carbon nanotubes (SWCNT) were obtained from CHASM (Boston, MA).

Cell Lines and Cell Culture

Drug resistant, triple-negative 4T1 breast cancer cells were transfected with tdTomato (Td) by Krais et al. as previously described [42]. B16F10 melanoma and 4T1-Td breast cancer cells from ATCC (Manassas, VA) were cultured in Roswell Park Memorial Institute (RPMI-1640) medium supplemented with 10 % fetal bovine serum (FBS) and 1% penicillin/streptomycin antibiotics (100 U mL-1 and 100 μg/mL-1 respectively). EMT6 breast cancer cells from ATCC (Manassas, VA) were cultured in Waymouth's MB 752/1 medium with 2 mM L-glutamine supplemented with 15% fetal bovine serume (FBS). All cells were grown at 37 ° C and 100% humidity under 5 % CO2. All cells were passaged using 0.25 % (w/v) Trypsin in 0.53 mM EDTA.

Nanotube Conjugation

The SWCNT-ANXA5 conjugate was prepared as previously described [70]. In brief, SWCNTs were solubilized in 1% sodium dodecyl sulfate (SDS) by repeated cycles of sonication and centrifugation. SWCNTs were then functionalized with a heterobifunctional 1,2-distearoyl-sn-glycero–3–phosphoethanolamine–N- maleimide (polyethylene glycol) (DSPE-PEG-MAL) linker. The sulfur reactive heterobifunctional linker was then capped with the protein annexin A5 (ANXA5). An in depth nanotube conjugation protocol can be found in Appendix C.

Mouse Tumor models

B16F10 melanoma, 4T breast cancer, and EMT6 breast cancer tumor models were employed in this study. C57/bl6 and Balb/cj mice were obtained from JAX (Frenchman Bay, ME). Primary tumors were induced by an orthotopic injection of 10^6 cells in the case of EMT6 and 4T1 tumors, and by a s.c. flank injection of 10^6 cells in the B16F10 model. The B16F10 tumor model furthermore required artificial induction of pulmonary metastasis by i.v. inoculation of 10^6 cells [71]. All other models spontaneously metastasized. Tumor model setup and treatment timelines can be found in Appendix C.

Flow Cytometry

Immunophenotypic antibodies and cytometric analysis was conducted as described previously [72]. A detailed protocol of sample preparation and staining can be found in Appendix C.

NIR Irradiation

Mice were irradiated 3 hours post treatment with SWCNT-ANXA5 with a diodeVET-50 NIR (980 nm) laser at an energy and power level of 175 J/cm^2 and 1 W/cm^2 respectively for 175 seconds. The NIR beam was set to irradiate an area 5 mm outside the tumor.

IR Temperature Analysis

Temperature was monitored in mice receiving NIR irradiation using a handheld FLIR TG165 Spot Thermal Camera from Raymarine ITC (Fareham, UK) set to auto scan for maximum detected temperature.

Therapeutic Antibodies

In the B16F10 model antibodies and immunomodulators were first given 48 hours before treatment. Checkpoint inhibiting anti-PD-1 (clone: J43; 12.5 mg/kg) was give twice weekly. Nucleotidase depleting anti-CD-73 (clone: TY/23; 5 mg/kg) was given twice weekly. The immunomodulatory drug cyclophosphamide (50 mg/kg) was given weekly. In the EMT6 model of breast cancer anti-CTLA-4 (clone: 9H10; 100 µg) was given twice per week.

Ex Vivo SCWNT Detection

Single-walled carbon nanotubes were detected in ex vivo tissue samples using a NS3 nanospectralyzer from Applied NanoFluorescence (Houston, TX). Standards can be found in Appendix D: Characterization of SWCNT.

Statistical Analysis

Data was analyzed with Graphpad Prism software. Statistical significance was assessed using a one-way ANOVA and Tukey-Kramer multiple comparisons test. Statistical significance of survival curves was determined by the Mantel-Haenszel log-rank test. Multiple comparisons were corrected by the Bonferroni threshold. Unless otherwise listed, all samples were n = 5 not including outliers as determined by the Tietjen-Moore test. Error is represented graphically as standard error unless error did not exceed the size of the plotted mean point symbol, in which case the bars were excluded for clarity.

Results and Discussion

SWCNT Dose-Dependent Ablation

Increasing doses of SWCNT-ANXA5 enhance targeted photothermal ablation of B16F10 tumors (Figure 8). C57BL6/j B6 albino mice were inoculated with B16F10 cells on day zero and tumor size was monitored until a size of 5 mm in diameter was reached. Mice were then given SWCNT-ANXA5 conjugate by i.v. injection and irradiated 3 hours later. Tumor volumes were then monitored twice weekly. Increasing doses of SWCNT-ANXA5 increased the efficacy of targeted photothermal ablation. After photothermal therapy, the tumor was undetectable at doses of 0.8 mg/kg. However, tumor regrowth occurred at all doses of SWCNT-ANXA5.

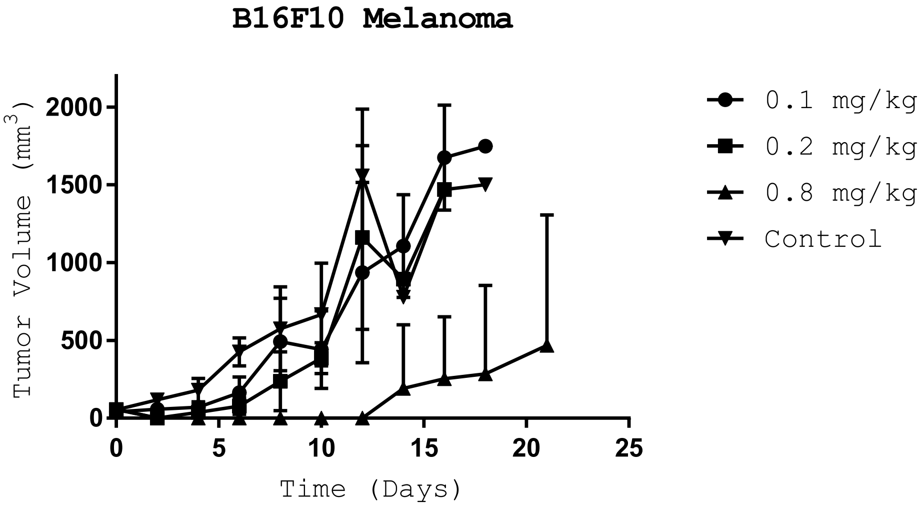

Figure 7: Dose-dependent tumor regrowth. C57/BL6 albino mice were inoculated with 10^6 B16F10 melanoma cells and tumors were allowed to reach 5 mm in diameter. Tumor volumes were recorded for 2 weeks in B6 albino mice following targeted ablation at varying doses of SWCNT-ANXA5. On day 0, mice received varying i.v. doses of SWCNT-ANXA5, and 3 hours later the tumors were stimulated with NIR irradiation at an energy and power density of 175 J/cm^2 and 1 W/cm^2, respectively (t = 175 s). Data is presented as mean ± SE (n = 7).

Following unsuccessful eradication of tumors in the B16F10 model at low doses of ANXA5-SWCNT, a repeat experiment was performed in the 4T1 model of breast cancer, employing higher doses of ANXA5-SWCNT. BALB/cj mice were given an orthotopic inoculation of 10^5 4T1 cells, and tumor growth was monitored twice weekly. When tumors reached a diameter of 5 mm, mice received various doses of SWCNT-ANXA5, and the primary tumor was irradiated as previously described (Figure 9). At doses of SWCNT-ANXA5 greater than 0.8 mg/kg, complete tumor eradication was observed. At doses of 1.2 mg/kg SWCNT-ANXA5 no tumor regrowth was observed. Moving forward, we choose the lowest dose capable of complete tumor eradication (1.2 mg/kg) as the standard for all following experiments.

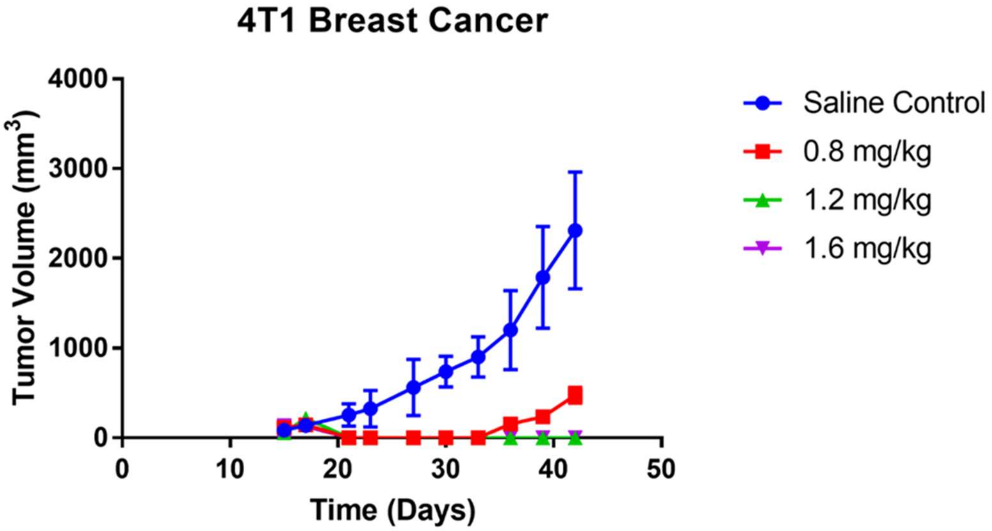

Figure 8: The growth of primary tumors following SWCNT-NIR photoablation as a function of SWCNT dose. Tumor volumes were recorded for 7 weeks in BALBcj albino mice following targeted ablation at varying doses of SWCNT-ANXA5. Cancer cells were inoculated on Day 0. On day 15, mice received varying i.v. doses of SWCNT-ANXA5, and 3 hours later the tumors were stimulated with NIR irradiation at an energy and power density of 175 J/cm^2 and 1 W/cm^2, respectively (t = 175 s). Data is presented as mean ± SE (n = 5).

Thermal Kinetics

Having determined that a dose of 1.2 mg/kg SWCNT-ANXA5 was necessary to eradicate tumors, we examined the heating profile of tumors during photothermal ablation (Figure 10). BALB/cj mice bearing EMT6 tumors of at least 5 mm in diameter were given a dose of 1.2 mg/kg SWCNT-ANXA5. Three hours after the administration of SWCNT-ANXA5 tumors were irradiated as described previously. During irradiation, tumor temperature was recorded with an infrared FLIR thermal imager. Mice who received a dose of 1.2 mg/kg SWCNT-ANXA5 prior to irradiation (right) had significantly high temperature profiles within the tumor then control mice (left). Over the period of irradiation, the maximum temperature reached temperatures as high as 60 ºC (Figure 11). This temperature was sufficient to eradicate the tumor without causing lasting harm to the animal (Figure 12).

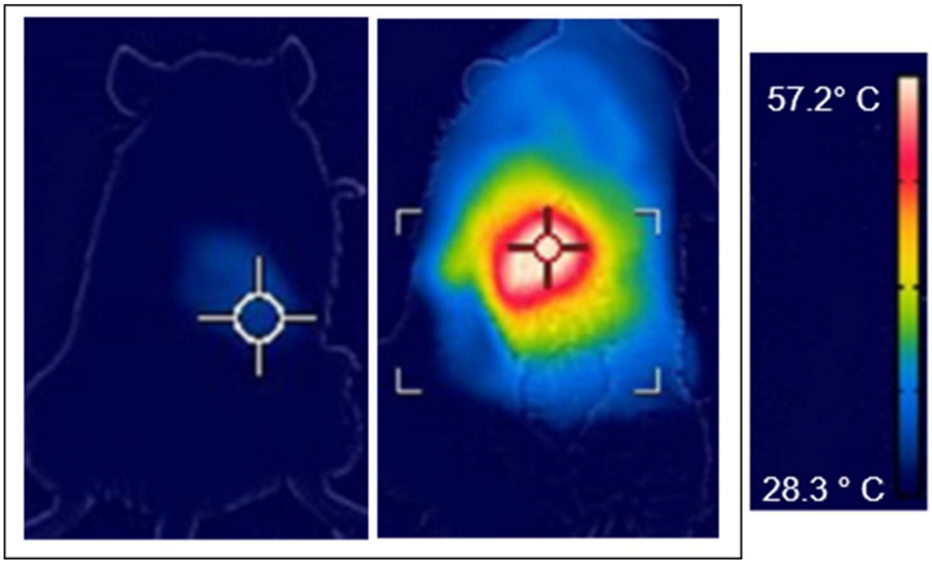

Figure 9**:** Temperature profile of the tumor and surroundings of mice after phothermal therapy. B16F10 tumors (d = 5 mm) were irradiated (175 J/cm^2 and 1 W/cm^2; d = 15 mm) and the temperature was recorded using a handheld infrared imager for mice receiving a saline control dose (left), and mice which received a dose of 1.2 mg/kg SWCNT (right) 3 h prior to irradiation.

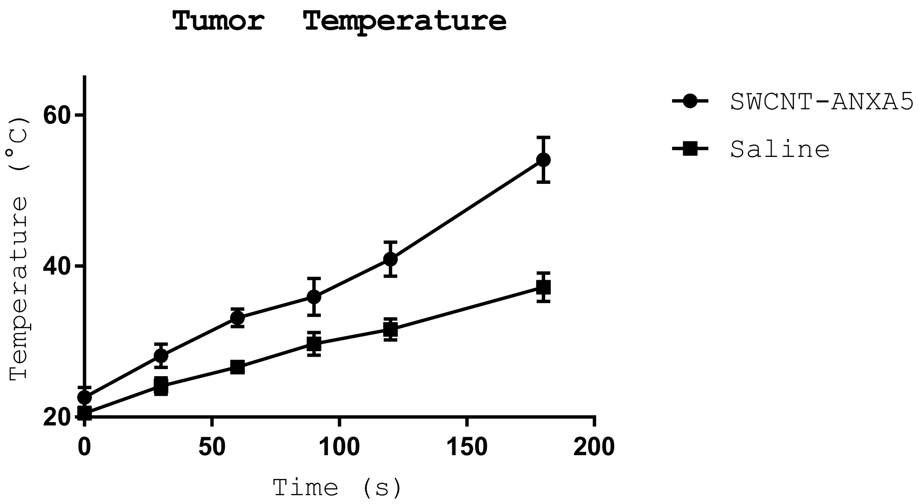

Figure 10: Mice bearing EMT6 tumors were irradiated and the max temperature of the tumor was recorded. Balb/cj mice bearing EMT6 tumors of at least 5 mm in diameter were injected by i.v. with 1.2 mg/kg SWCNT-ANXA5. Three hours later tumors were irradiated with a NIR laser at an energy and power density of 175 J/cm^2 and 1 W/cm^2, respectively (t = 175 s). The temperature of tumors from mice receiving SWCNT was singnificantly higher then controls at t = 175 s ($P \leq 0.005$) Data is presented as mean ± SE (n = 3).

At the conclusion of irradiation for mice which received SWCNT, the average max tumor temperature was 54.7 ° C, this temperature was sufficient to ablate the tumor [50]. The temperature of tumors in the saline control group remained below 40 °C, a temperature which provides minimal therapeutic benefit [73-75]. In the SWCNT-ANXA5 treated group, visible ablation of the tumor was characterized by the rapid discoloration of the tumor. Following discoloration of the tumor the skin began to tighten taking on a shriveled appearance. Within 48, hours a significant eschar formed at the site of photothermal ablation. Complete skin regrowth took several weeks. (Figure 12).

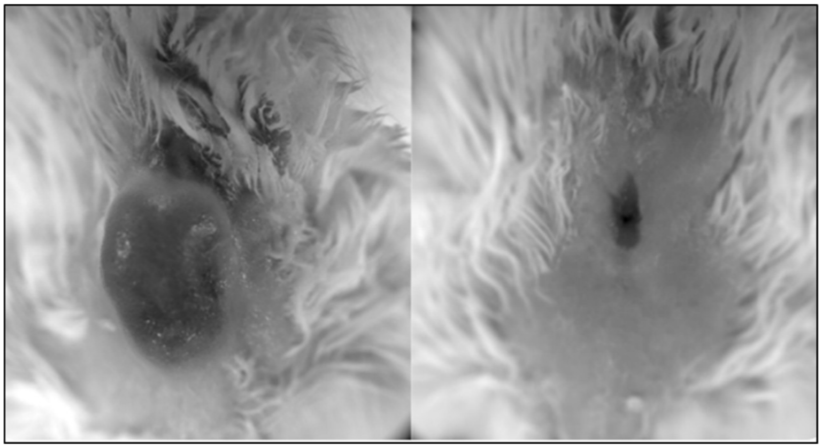

Figure 11: Photothermal therapy combining SWCNT-ANXA5 and NIR irradiation lead to the complete tumor regression as seen 2 weeks following treatment. A representative s.c. melanoma tumor before (left) and 3 weeks after (right) targeted laser stimulation in conjunction with a SWCNT-AV dose of 1.2 mg/kg. Tumors had a diameter of d = 4.6 ± 0.2 (mean ± SE) mm.

Biodistribution

Following the successful identification of a dose of SWCNT-ANXA5 capable of permanent tumor eradication, we undertook a biodistribution assay (Figure 13). Balb/cj mice (n = 5) were treated with 1.2 mg/kg SWCNT-ANXA5 and at select times mice were euthanized for tissue collection. Samples were prepared as described previously [76]. Samples were first compared on the basis of the percent injected dose detected in each organ. We observed the majority of SWCNT-ANXA5 accumulation primarily in the liver, heart, spleen, kidneys, tumor and lungs. In mice with EMT6 tumors we observed SWCNT-ANXA5 accumulation within the tumor as well. Trace amounts of SWCNT-ANXA5 were detected in the brain, large intestines and small intestines.

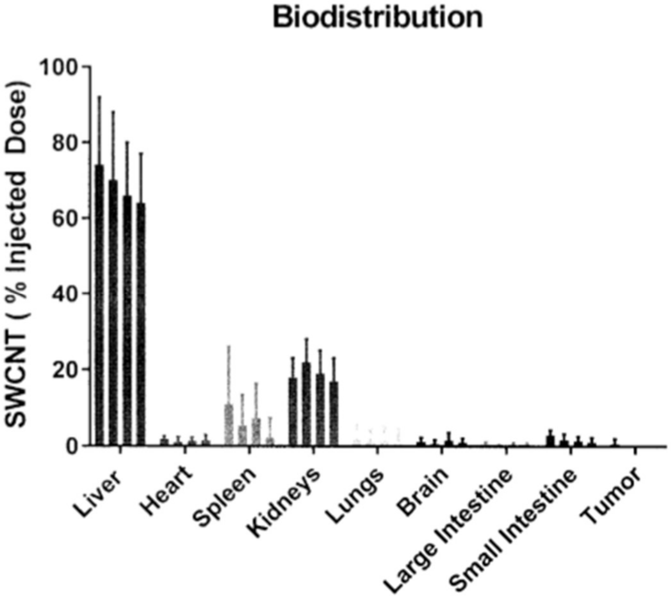

Figure 12: Biodistribution of SWCNT-ANXA5. Following an i.v. injection of 1.2 mg/kg SWCNT-ANXA5 in BALB/cj mice, tissue was excised at 1,2,3 and 4 months after inoculation, and SWCNTs were detected in the liver, spleen, kidneys and lungs. Trace amounts of SWCNTs (<1% I.D) were detected in the heart, brain, and small intestine. Data is presented as the mean ± SE (n = 3).

It is important to note that the biodistribution of SWCNT on the basis of %ID, does not correlate well with the absolute concentration of SWCNT within a target tissue. This is primarily due to the differences between organ weights. For instance a given % ID within an organ will correspond to a higher concentration within smaller organs, and smaller concentrations within larger organs. Comparing samples on the basis of SWCNT reveals that the highest concentrations of SWCNT within the kidney, followed closely by the liver and spleen (Figure 1 4). High concentrations of SWCNT can be detected in the heart, lungs and kidneys as well. Trace amounts of SWCNT were detected in the brain and intestines.

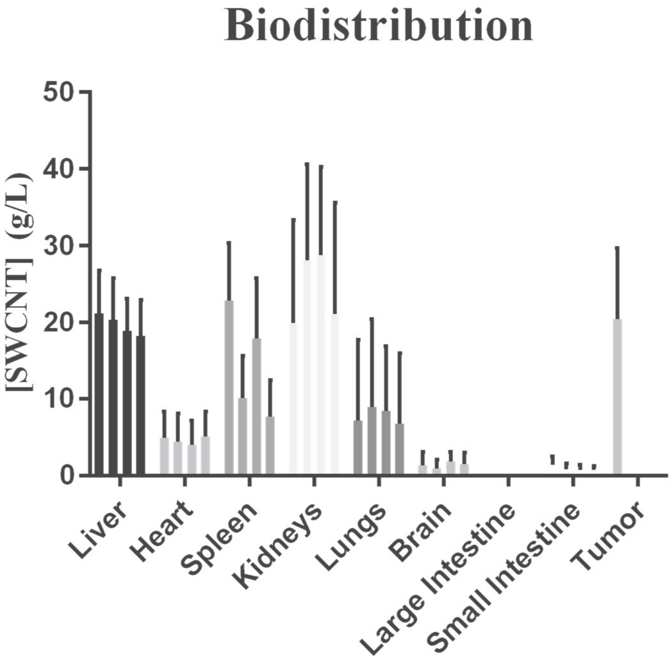

Figure 13: Biodistribution of SWCNT-ANXA5. The SWCNT-ANXA5 conjugate was i.v. injected in Balb/cj mice as at a dose of 1.2 mg/kg, and the concentration of SWCNT was then measured at 3 hours in the tumor. The SWCNT concentration was measured in various organs of mice without tumors after 1, 2, 3 and 4 months (left to right). Data is shown as mean ± SE (n = 3).

Abscopal Effect

Enhanced survival and reduced tumor growth was observed in mice receiving a combination of SWCNT-ANXA5 directed photothermal therapy and anti-CTLA-4 checkpoint inhibition (Figure 16). Mice were inoculated with EMT6 and treated as described in Figure 15. Photothermal therapy exceled at destroying orthotopic EMT6 primary tumors but failed to enhance survival overall survival. Immunostimulation with α-CTLA-4 enhanced overall survival but failed to eradicate primary tumors. The synergistic combination of SWCNT-ANXA5 directed photothermal therapy and α-CTLA-4 immunostimulation enhanced survival, leading to 55 % survival.

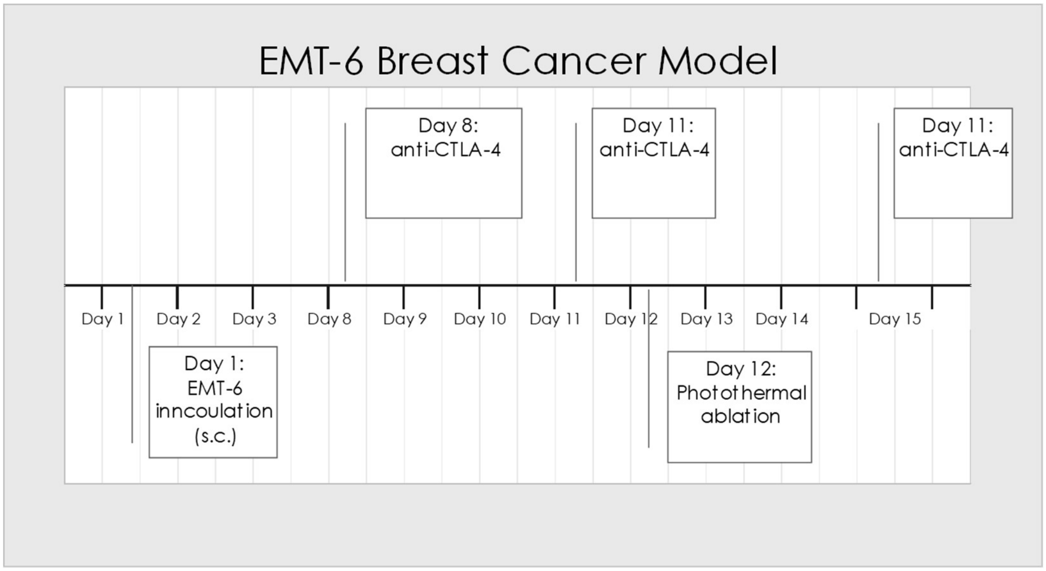

Figure 14: EMT6 breast cancer model timeline. Mice received an s.c. inoculation of 10^6 EMT6 metastatic breast cancer cells on day 1, and then received checkpoint inhibiting anti-CTLA-CTLA-4 antibodies on days 8,11, and 16. Tumors were irradiated on day 12 with SWCNT-ANXA5.

As early as the 1950s, researchers observed that localized tumor irradiation had a significant effect on distant tumors [77]. Mechanistic studies have established that the systemic nature of the abscopal effect is due to the host's immune response [78-81]. While γ-irradiation has been the prime focus of most abscopal research, a growing body of work demonstrates that photothermal therapy can induce an abscopal effect as well. Numerous studies have demonstrated that thermal ablation in combination with the checkpoint inhibitor anti-CTLA-4, produces a heightened immune response [82-88]. We observe an abscopal response following photothermal ablation and anti-CTLA-4 blockade in the EMT6 model of breast cancer.

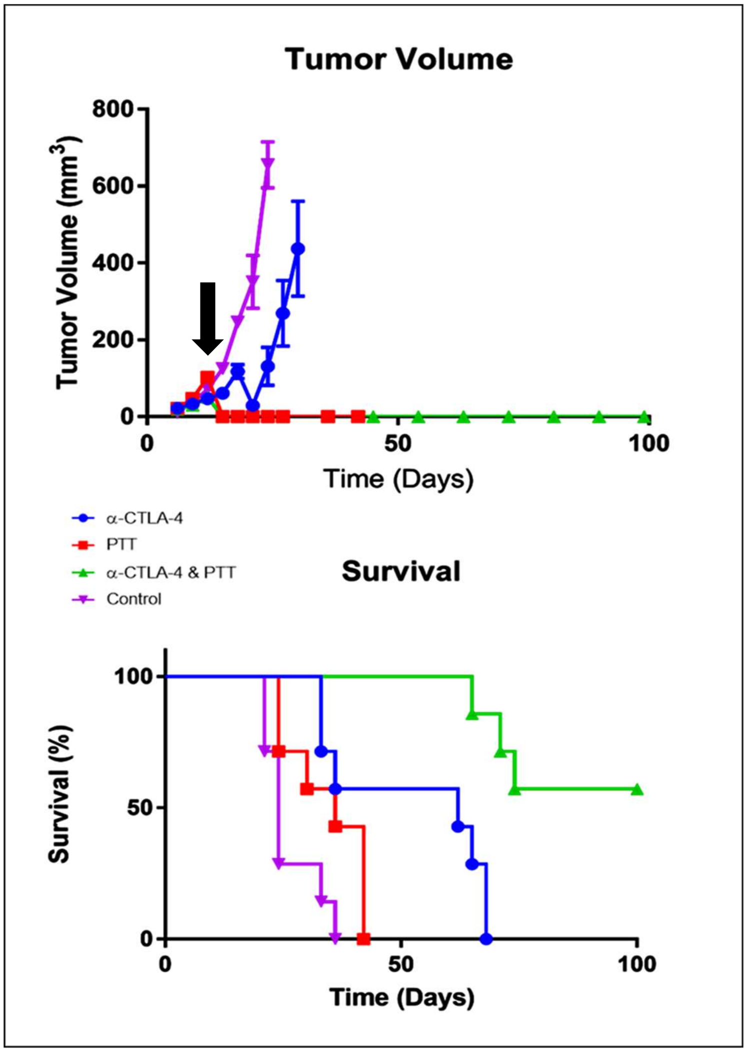

Figure 15: The growth of primary tumors and the survival of mice bearing EMT6 tumors. Mice with well developed orthotopic syngeneic tumors (d ≥ 5 mm) were administered an intravenous systemic dose of 1.2 mg/kg SWCNT-ANXA5. Tumors were then irradiated (arrow) with mild laser light using a Diodevet-50 NIR system for 175 s, at a power density of 1 W/cm^2 on dat 12 (arrow). Anti-CTLA-4 was injected on days 8, 11, and 16 (100 μg per injection). Photothermal therapy eradicated primary tumors, and the combination of photothermal therapy and immune checkpoint inhibition significantly increased survival compared to controls ($P \leq 0.05$). Data is shown as time since tumor inoculation, with tumor volume shown as mean ± SE (n = 7).

Flow Cytometry

Using flow cytometry, we examined the relative populations of immune effector cells in mice (Figure 16, Figure 17, Figure 18). Mice were inoculated with EMT6 and treated as described earlier. Two weeks after treatment mice were sacrificed and we identified both the percentage and relative count of multiple types of immune effector cells.

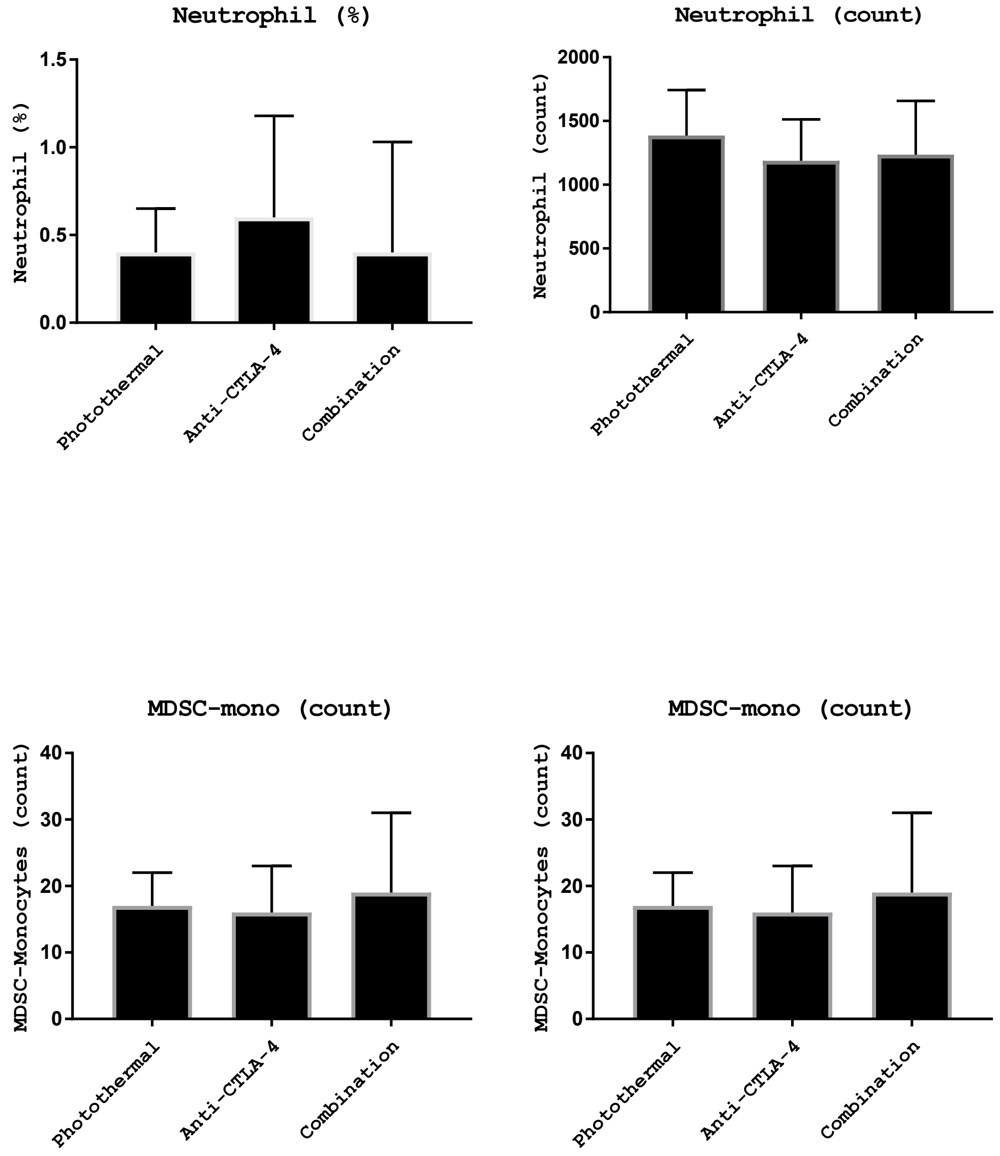

Figure 16: Splenocyte cell populations in mice treated by various treatments. The relative counts and % composition of neutrophils and MDSC monocytic splenocytes was examined 14 days following photothermal treatment. Data is presented as the mean ± SE (n = 3).

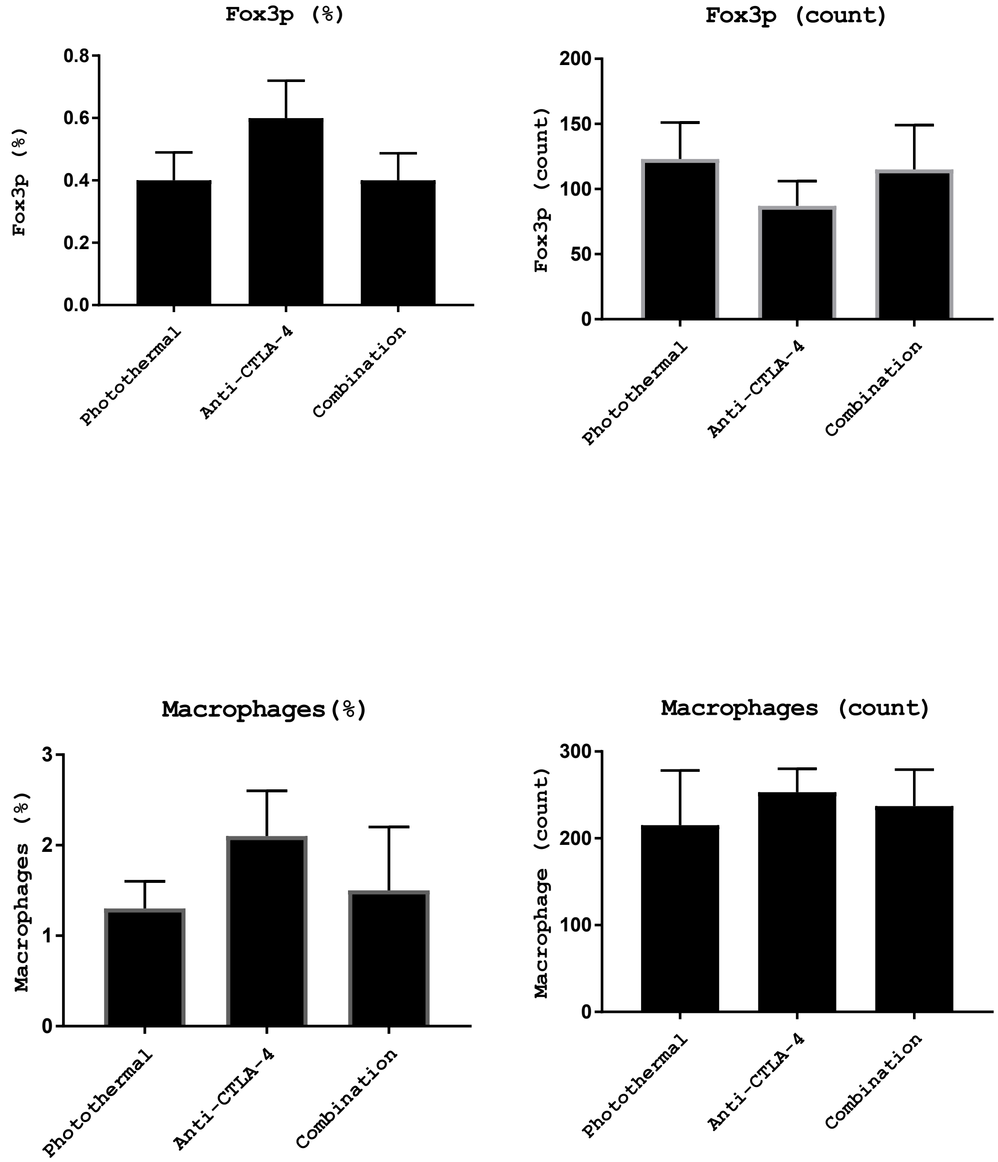

Figure 17: <u>Splenocyte cell populations in mice treated by various treatment (continued).</u> The relative counts and % composition of Fox3p and macrophage splenocytes was examined 14 days following photothermal treatment. Data is presented as the mean ± SE (n = 3).

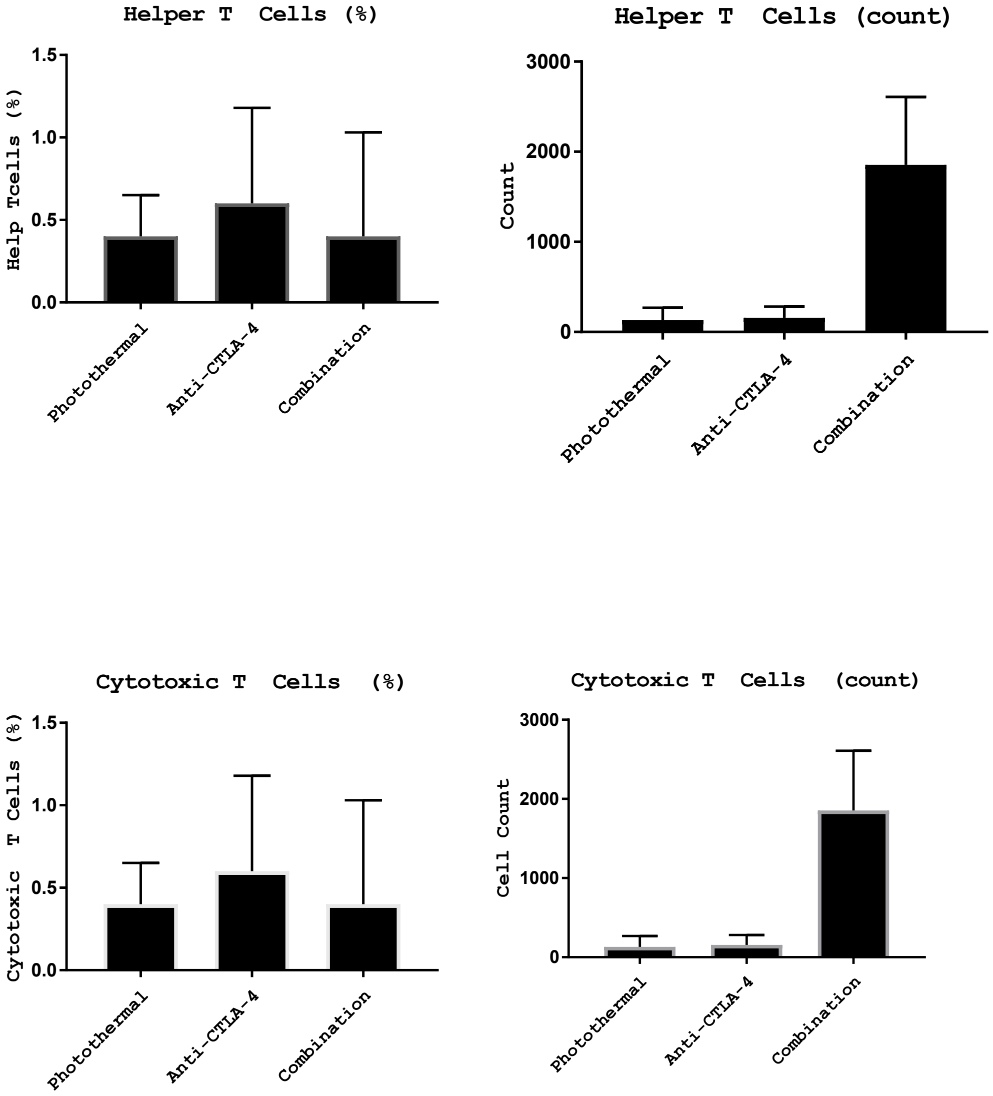

Figure 18: Splenocyte cell populations in mice treated by various treatment (continued). The relative counts and % composition of Helper T cells and Cytotoxic T cells was examined 14 days following photothermal treatment. Data is presented as the mean ± SE (n = 3).

In mice receiving both anti-CTLA-4 checkpoint inhibition and SWCNT-ANXA5 targeted photothermal therapy, we observed immunophenotypic changes in splenocyte populations. Specifically, we observed increases in both tumor killing CD4(+) T-helper cells and CD8(+) cytolytic cells (Figure 20).

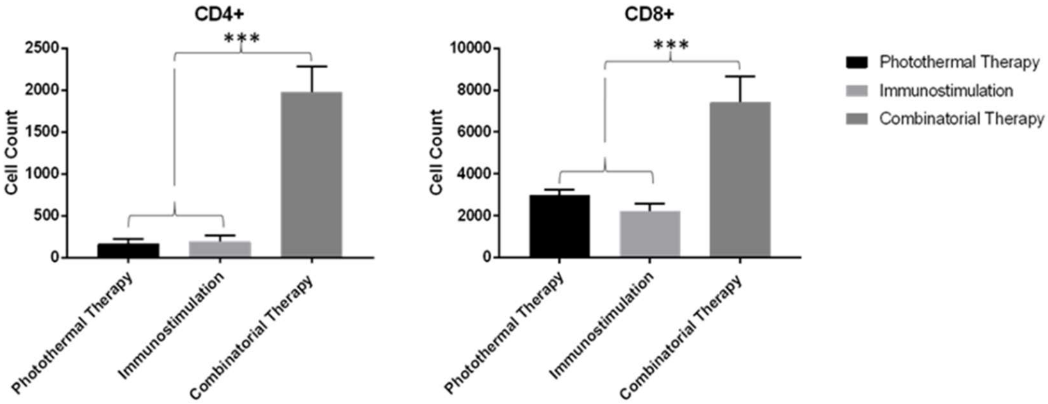

Figure 19: <u>Photothermal therapy in conjunction with α-CTLA-4 checkpoint inhibition significantly increased the number of CD4(+) and CD8(+) splenocytes.</u> For the three groups treatment was the same as previously described. Data is for cells in the spleen at 2 weeks following treatments and is presented as the mean ± SE (n = 3). Significance is indicated by *** ($P \leq 0.005$).

Increases in CD4(+) and CD8(+) cell counts correlated to increases in spleen sizes observed during necropsy. Increased spleen size indicates a heightened immune response. The spleen is comprised of multiple cell types, the most common of which are of the CD4(+), CD8(+), and B-cell lineages [89, 90]. While not explored in this body of work, we would expect B-cell counts to increase along with CD4(+) and CD8(+) T-cells counts [91]. Helper T-cells also known as CD4(+)

T-cells, assist in humoral immunity by facilitating other immune cells by cytokine stimulation and direct cell-cell interactions. Cytolytic T-cells, also known as CD8(+) cells, directly kill tumor cells. Increases in CD4(+) and CD8(+) cell counts are indicative of a systemic abscopal immune response.

Conclusion

The aminophospholipid Ptd-L-Ser is actively sequestered to the inner leaflet of the plasma membrane of health cells. In a tumor, this tightly regulated Ptd-L-Ser membrane asymmetry breaks down and Ptd-L-Ser is expressed on the outer leaflet of cancerous cells and the vascular endothelium. The presence of Ptd-L-Ser solely within the tumor serves as a tumor specific antigen which can be used in targeted therapeutics. We employ the natural ligand of Ptd-L-Ser, ANXA5, in a protein-nanoparticle conjugate to sensitize tumors to photothermal ablation. The combination of ANXA5 directed SWCNT dependent photothermal ablation with anti-CTLA-4 checkpoint inhibition significantly increased survival in the orthoptic EMT6 model of breast cancer.

We observe SWCNT-ANXA5 dependent near-infrared ablation of tumors using thermal imaging and confirm the selective accumulation of ANXA5-SWCNT in tumor vasculature by fluorescent spectroscopy. We further establish the biodistribution of SWCNT following photothermal treatment. We then demonstrate the synergism between this targeted photothermal ablation modality and immunostimulation in several models of invasive metastatic cancer. Notably in the orthotopic EMT6 model of breast cancer, we observe a synergistic decrease in tumor regrowth and a corresponding increase in survival following the combination of SWCNT-ANXA5 targeted photothermal ablation and anti-CTLA-4 checkpoint inhibition. We observe an increase in splenocytes of the cytolytic CD8(+) T-cell and helper CD4(+) T-cell subsets in mice receiving the combinatorial therapy. The increase in tumor suppressing T-cells would lead to enhanced tumor rejection and increased survival via an abscopal response, as we have observed.

Chapter 3: Antimalarial Activity of Chimeric Fusion Protein

Abstract

A cytocidal mutant enzyme, cystathionine- γ-lyase (mCGL), was targeted to phosphatidylserine (Ptd-L-Ser) expressed on malaria infected erythrocytes through fusion with the protein annexin A5 (ANXA5). The resulting fusion protein selectively accumulates to Ptd-L-Ser expressing parasite infected erythrocytes by ANXA5-dependent binding, where the enzyme catalyzes the generation of toxic products. The enzymatic activity of parasite localized mCGL was highly toxic to infected erythrocytes, but minimally toxic to healthy erythrocytes. We demonstrate the antimalarial activity of this fusion protein both in vitro and in vivo.

Introduction

Malaria is the single most deadly infectious disease, infecting 214 million individuals a year of which almost 438 thousand will die. Discounting direct mortality, malaria represents a significant burden on the health care system of many countries [32, 33]. In malaria endemic countries, malaria accounts for almost one half of all hospital visits. Compounding these issues is the spread of drug resistant malaria. Emerging strains of the Plasmodium parasite responsible for malaria are resistant to all known pharmaceutical treatments. There is a significant need for new antimalarial therapeutics.

Therapeutic Approach

Using multiple in vitro models and a murine model of the disease, we demonstrate the antimalarial activity of the fusion protein ANXA5-mCGL. A succinct summary of the therapeutic mechanism of action can be seen below (21Figure 20: Therapeutic design philosophy.).

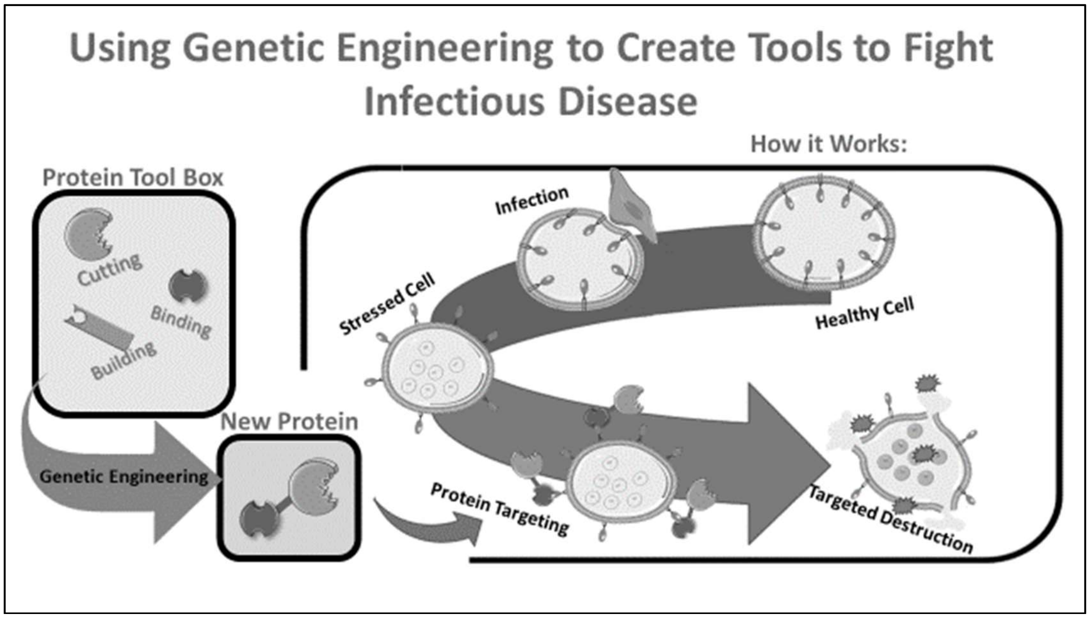

Figure 20: Therapeutic design philosophy.

Antimalarial Action

The antimalarial activity of the fusion protein begins with ANXA5 dependent binding to the infected erythrocyte. Once bound to the parasite-infected erythrocyte, the active microcidal domain of ANXA5-mCGL (mCGL) actively catabolizes multiple thiol-containing compounds such as methionine. This lyase activity has a twofold impact on parasite growth and survival. First, many of the substrates for mCGl are essential parasite nutrients [92, 93]. The Plasmodium parasite lacks many of the common eukaryotic metabolic pathways necessary to synthesize these crucial metabolites. Lacking these compounds, the parasite is unable to fuel its rabid growth. Secondly, the byproducts of mCGL lyase activity are potent cell toxins. The enzyme mCGL produces byproducts such as hydrogen sulfide, reactive oxygen species (ROS), and ammonium. The twofold antimalarial action of the enzyme mCGL is further compounded by the parasitic nature of the malaria parasite. The parasite actively imports many of the substrates of mCGL to fuel its growth [92]. The result of this active transport is an increase in substrate concentration susceptible to mCGL activity, further enhancing the therapeutic effect of the fusion protein.

In contrast to typical chemotherapeutic agents, ANXA5-mCGL does not inhibit parasite growth. The fusion protein selectively targets infected cells for destruction by enzymatic action (Figure 22). Here we present the in vitro antimalarial action of ANXA5-mCGL in the P. Yoelii and P. berghei models. Furthermore, we demonstrate the in vivo antimalarial action of the fusion protein in the P. berghi model.

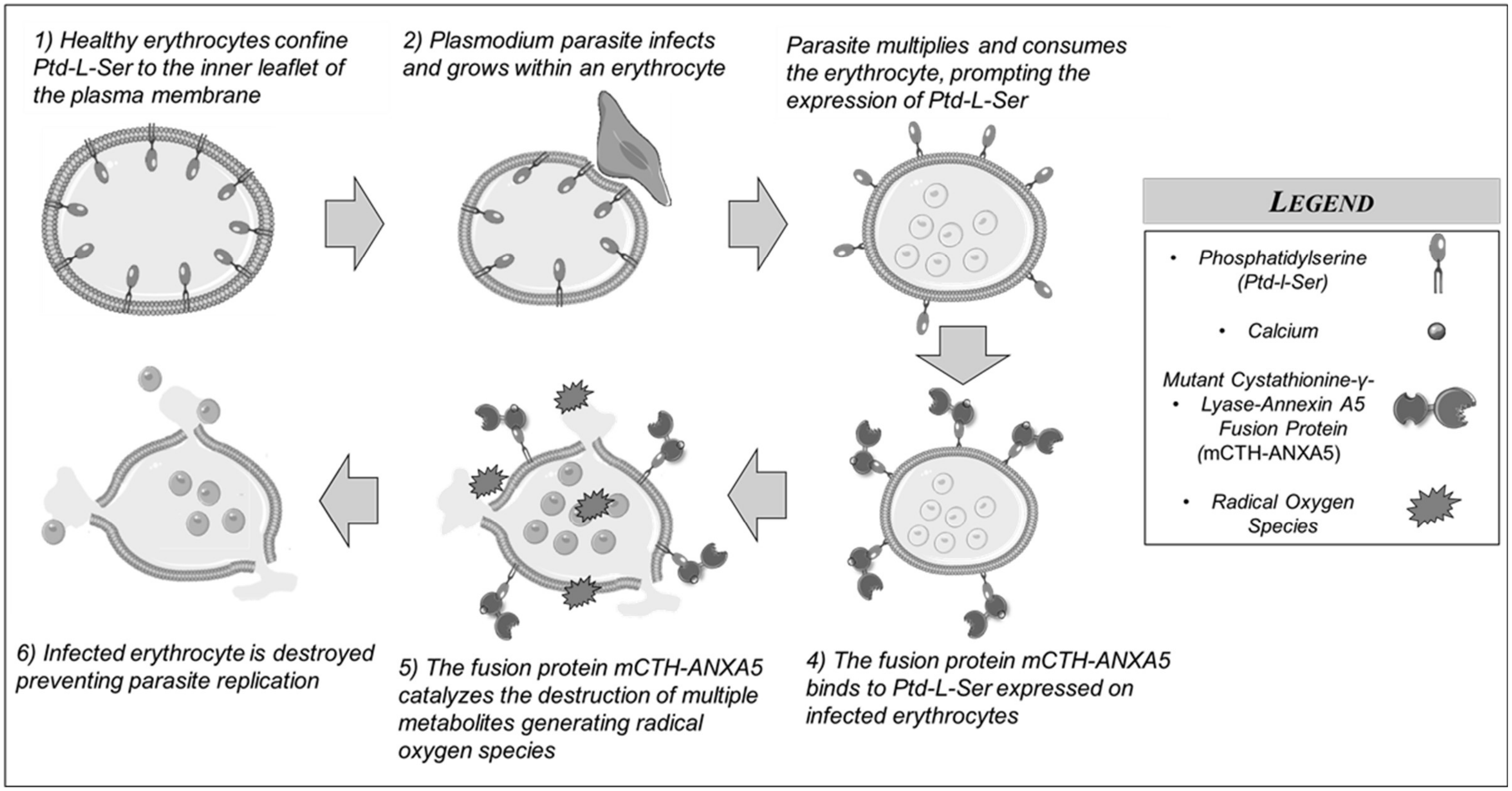

Figure 21: The antimalarial mechanism of action of the fusion protein mCGL-ANXA5.

Materials and Methods

Materials

An AXA5-mCGL vector was previously constructed as part of a pET-30 Ek/LIC plasmid using Gibson fragment assembly cloning [46]. Modified giemsa stain, bovine serum albumin (BSA), pyridoxal-3-phosphate, Triton X-100, EDTA, selenomethionine, and Tris-acetate-EDTA buffer were from Sigma-Aldrich (St Louis, MO). His-trap columns were from GE Healthcare (Chicago, IL). Sodium phosphate and sodium dodecyl sulfate (SDS) were from Mallinckrodt Chemicals (Phillipsburg, NJ). Antifade reagent Fluoro-gel, borate buffer, Hoescht stain, FITC, Deep Red Plasma Membrane stain, DAPI, propidium iodide, flow cytometry staining buffer, fixation/permeabilization buffer, permeabilization buffer, and LAL chromogenic endotoxin quantitation kit were from Thermo Fisher Scientific (Waltham, MA). The 2 and 100 kDa dialysis membranes were from Spectrum Laboratories (Rancho Dominguez, CA). Roswell Park Memorial Institute cell medium (RPMI-1640) and Hank's balanced salt solution (HBSS) were from ATCC (Manassas, VA). Fetal bovine serum (FBS) was from Atlanta Biologicals (Lawrenceville, GA).

Cell Lines and Cell Culture

Murine blood samples infected with Plasmodium yoelii (substrain yoelii; 4-20 % parasitemia) and wildtype Plasmodium berghei (substrain ANKA; 3-5% parasitemia) were kindly donated from the lab of Dr. Noah Butler (OUHSC). Plasmodium berghei samples (Substrain ANKA; mutation 507m6c11) were obtained through the Biodefense and Emerging Infections Center of the CDC (BEI). The P. berghei ANKA mutation 507m6c11 parasites are transformed by double cross-over integration using the pL0023 (BEI MRA-792) vector to constitutively express green fluorescent protein [94]. In flow cytometric applications 507m6c11 parasites are GFP(+). For in vitro work, samples were collected from infected mice and immediately diluted in ice cold RPMI-1640 supplemented with 10% FBS without antibiotic/antimycotic. Parasites were cultured for up to 24 hours at 37 °C and 100% relative humidity using the candle jar method [95]. Parasites were maintained for in vivo studies by serial passage in mice. Frozen aliquots of P. berghei were stored in medium supplemented with 5% DMSO under liquid nitrogen. Cryogenic lots were first passaged in mice twice before use during in vivo studies.

Fusion Protein Production

Recombinant mCGL-ANXA5 was produced and isolated by His-tag chromatography, and activity was confirmed by a chromatographic assay as previously described [46]. The experimental procedure is given in Appendix A. The experimental procedure is provided in Appendix A. Purity was confirmed by SDS-PAGE. Samples were confirmed endotoxin free by limulus amoebocyte lysate assay.

Parasite Models and Cytotoxicity

In cytotoxicity studies, P. yoelii infected erythrocytes were analyzed by flow cytometry. Samples were first gated to select a population of CD71(+) erythroid cells [CD71(+) erythrocytes are Ter-119(+)]. Following selection of erythrocytes, samples were gated to remove the presence of CD45(+) nucleated leukocytes. Nonviable nucleated cells were identified by staining with the cell impermeable nuclear stain propidium iodide (PI). The cell impermeable PI stain is only capable of staining nucleated cells with compromised cellular membranes PI(+). Nonviable parasites were identified after treatment with fusion protein as CD45(-)CD71(+)PI(+) erythrocytes. Viability of parasite samples was measured following overnight (12 h) or after a short term (3 h) incubation at 37°C using the candle jar method. A brief description of the candle jar method can be found in Appendix A.

Fusion protein (mCGL-ANXA5) dependent parasite death was further confirmed by both giemsa stain and histological light microscopy examination. Fresh samples of infected blood were in incubated for 3 hours with 100 nM fusion protein to allow fusion protein binding to parasite surface. Following this brief incubation, the samples were washed to remove excess protein and incubated overnight with various concentrations of the prodrug selenomethionine (setmet). Following treatment, samples were fixed and examined by both giemsa stain and differential interference contrast microscopy.

In a second model of malaria, the viability of fusion protein (mCGL-ANXA5) treated P. Berghei infected erythrocytes was measured using flow cytometry. Samples of infected erythrocytes were gated to remove the presence of CD45(+) nucleated leukocytes. The leukocyte free population of cells was then gated on recombinant P. berghei parasites. Parasites of substrain ANKA, mutation 507m6c11 are transformed to be green fluorescent by GFP(+) parasites. Nonviable nucleated cells were identified by staining with the cell impermeable nuclear stain propidium iodide (PI). The cell impermeable PI stain is only capable of staining nucleated cells with compromised cellular membranes PI(+). Nonviable CD45(-) GFP(+)PI(+) parasites were quantified and compared to viable CD45(-)GFP(+)

PI(-) parasite control samples after a short-term (3 h) incubation.

Erythrocyte Damage

The structure of fusion protein (mCGL-ANXA5) treated P. Berghei infected erythrocytes was assessed using flow cytometry. Erythrocytes were identified in blood samples as CD45(-)CD71(+) cells. Erythrocyte structure was analyzed by flow cytometric FSC/SSC gating. Damaged cells were crudely identified as events that deviated from original size gating parameters of healthy erythrocytes. Treated cell samples were analyzed following short-term or overnight incubation with fusion protein.

Survival Model

The survival of P. berghei inoculated mice was monitored for a period of one month. Male CF-1 mice of 6 weeks of age sourced from Charles River (Boston, MA) were inoculated with 1×10^6 P. berghei infected erythrocytes by i.p. injection. Infected mice were treated the following day with 15 mg/kg fusion protein in 150 μL of phosphate buffered saline or with phosphate buffered saline control. After the all control animals perished, the study was concluded (28 days) and surviving treated mice were necropsied.

Weight

The weight of mice receiving daily fusion protein (mCGL-ANXA5) or saline control treatments was monitored over one month. Male outbred Swiss CF-1 mice of 6 weeks of age were treated daily with 15 mg/kg of fusion protein by i.p. injection for 20 days. Following treatment mice were monitored for 4 weeks to observe any changes in weight of behavior.

Flow Cytometry

Samples of infected blood (100 µL) were harvested in sodium citrate coated syringes and immediately diluted with 5 mL of ice cold media. Cell numbers were then enumerated using a hemocytometer. Samples (100 µL) were diluted to a final concentration of 10 x 10^6 iRBC per mL^{-1} with flow cytometry buffer. Samples (500 µL) were stained with a combination of 0.2 µg of APC α-CD45 (Rat IgG2b, κ; clone 30-F11), 0.2 µg of PE α-CD71 (Rat IgG2a, κ; clone R17217), and 5.0 µg of propidium iodide (PI). Samples of iRBC were incubated with the antibody cocktail for 1 h at 4 °C, protected from light. Cells were then washed (x3) by pelleting (5 min; 500 *g*) discarding the supernatant and suspending in 1 mL of flow cytometry staining buffer. Following the last wash, cells were suspended in flow cytometry staining buffer with PI. Samples were then incubated at 4 °C for 15 minutes in the dark. Samples were then analyzed via a BD Accuri C6 flow cytometet (San Jose

Ca). Detailed flow cytometry gating schema can be found in Appendix A: Antimalarial Fusion Protein.

Histology

Thin blood smears were created on glass microscopy slides from samples (15 µL) of iRBC. The smear was allowed to dry for 2 h, and then fixed for 20 s with ice cold methanol. Fixed smears were then stained for 45 min with a solution of 0.02 w/v% modified giemsa stain diluted in deionized water. Samples were allowed to dry and then analyzed with a E800 Nikon fluorescent microscope. Pictures were captured with a Sony CMOS IMX183 AMscope camera.

Statistical Analysis

Data was analyzed with Graphpad Prism software. Statistical significance of parasite cytotoxicity was assessed using a one-way ANOVA and Tukey-Kramer multiple comparisons test. Statistical significance of survival curves was determined by the Mantel-Haenszel log-rank test. Multiple comparisons were corrected by the Bonferroni threshold. Unless otherwise listed all samples were n = 5 not including outliers as determined by the Tietjen-Moore test. Error is represented graphically as standard error unless error did not exceed the size of the plotted mean point symbol, in which case the bars were excluded for clarity.

Results and Discussion

Plasmodium Yoelii Model

The P. yoelii model of infection is a murine model of human malaria [96]. This model is highly prized by researchers for three reasons. First, the infection is nonfatal; animals can be studied after experimental treatment. Second, the yoelii strain of plasmodium expands rapidly in the blood (40% parasitemia), providing a large pool of parasites for in vitro studies. Finally, the significant P. yoelii - P. falciparum homology makes yoelii one of the first choices for in vitro drug testing [97]. Here we demonstrate that the fusion protein ANXA5-mCGL has significant antimalarial activity as assayed in the P. yoelii model by fluorescent light microscopy, flow cytometry and histological staining.

Using fluorescent microscopy, we assayed fluorescent fusion protein accumulation to P. Yoelii infected erythrocytes (parasitemia 40 %) (Figure 23). Immediate fluorescent microscopy of the samples revealed accumulation of FITC-ANXC5-mCGL (green) to parasitized cells (blue). Following this confirmation of fusion protein binding, we undertook an initial assay of fusion protein antimalarial activity. When cultured overnight with fusion protein, the number of identifiable Hoechst stained parasites decreased (Figure 24). We conclude from this light microscopy data that the fusion protein has ANXA5 dependent accumulation and cytotoxicity. We proceeded to establish the full dose-response model of the fusion protein in the P. yoelii model of infection.

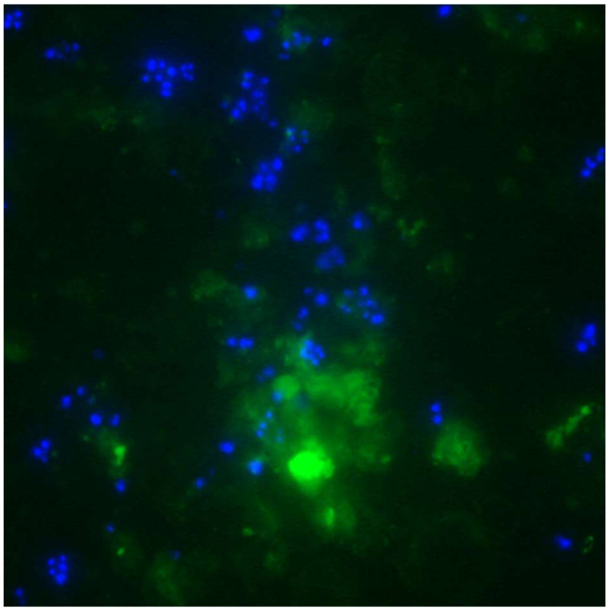

Figure 22: Fusion protein binding. Infected erythrocytes (1 x 106) were incubated briefly with 0.02 µg/mL of FITC labeled fusion protein (FITC-ANXA5-mCGL) and 0.01 µg/mL Hoechst stain. Infected erythrocytes were then washed and suspended in HBSS. Fluorescent light microscopy of P. berghei infected erythrocyte cultures revealed the accumulation of ptd-L-ser binding annexin-FITC (green) on parasitized cells (blue).

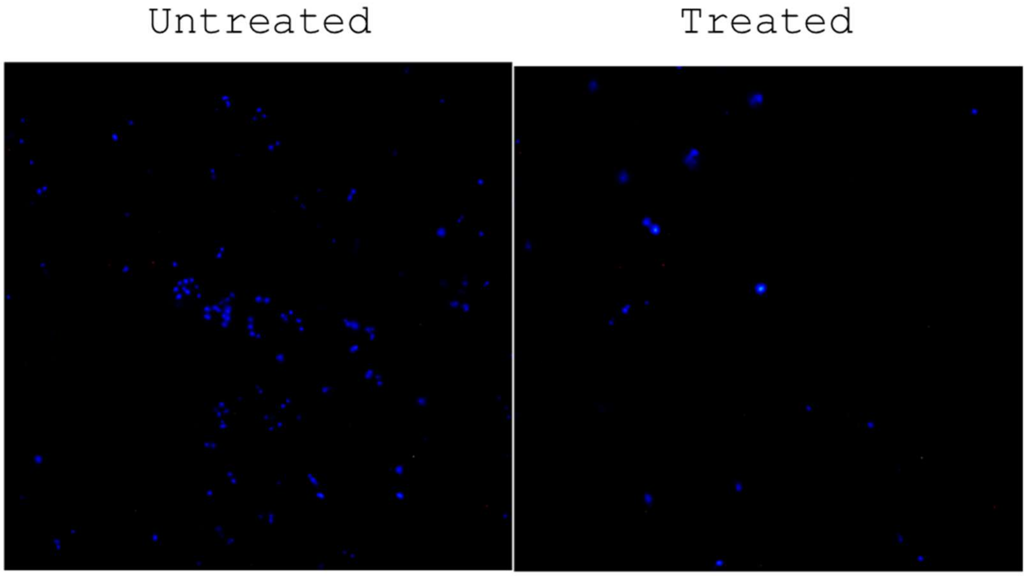

Figure 23: DNA stain of treated and untreated parasites. Erythrocytes infected with P.berghei were cultured overnight with a saline control (left) or with 40 nM fusion protein (right). The number of Hoechst stained parasites (blue) were significantly decreased after treatment with fusion protein.

The dose-response model of ANXA5-mCGL and P. yoelii was constructed by experimental flow cytometry (Figure 25). The viability of parasite samples (n = 3) was measured following overnight (12 h) incubation at 37°C using the candle jar method. Treated samples of infected erythrocytes were gated to select a population of CD71(+) erythroid cells. Following selection of erythroid cells, samples were gated to remove the presence of CD45(+) nucleated leukocytes. The remaining nonviable nucleated cells were identified by staining with the cell impermeable nuclear stain propidium iodidie (PI). The 50% cytotoxic concentration (CC50) was determined to be 40 nM.

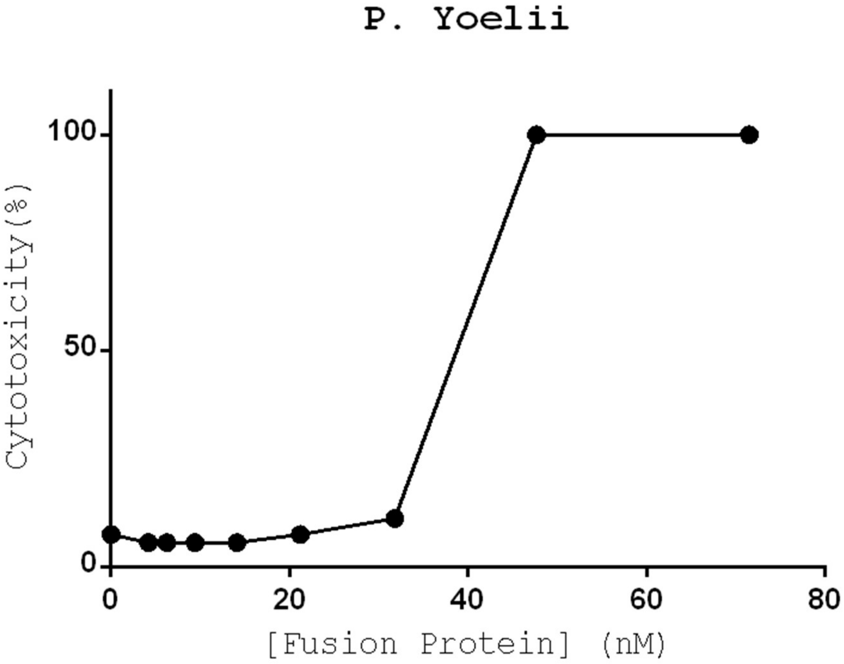

Figure 24: P. Yoelii treated with Fusion Protein. Samples of infected erythrocytes were gated to select a population of CD71(+) erythroid cells (CD71(+) erythrocytes are Ter-119(+)). Following selection of erythrocytes, samples were gated to remove the presence of CD45(+) nucleated leukocytes. Nonviable parasites within infected erythrocytes were identified by staining with the cell impermeable nuclear stain propidium iodide (PI). The cell impermeable PI stain is only capable of staining nucleated cells with compromised cellular membranes PI(+). Nonviable parasites were identified after treatment with fusion protein as CD45(-)CD71(+)PI(+)erythrocytes. Viability of parasite samples was measured following overnight (12 h) incubation at 37°C using the candle jar method. Data is presented as the mean ± SE (n = 3).

The dose-response model of ANXA5-mCGL and P. yoelii was constructed using propidium iodide and cytometric analysis. Propidium iodide possesses a positive charge and is unable to cross intact cellular membranes [98]. Damaged cells such as those in the late stages of cell death have damaged membranes.

Propidium iodide accumulates in dying cells where it binds to DNA. We observed a dose-dependent increase in the propidium iodide fluorescence of parasites when treated with ANXA5-mCGL starting at concentrations as low as 30 nM (Figure 25). The death of parasitized cells and corresponding increase in propidium iodide fluorescence rapidly increased with the concentration of ANXA5-mCGL. The concentration of enzyme cytotoxic to half of all parasites (CC50) was 40 nM. All parasites were killed by a concentration of only 50 nM.

While we observed antimalarial activity solely with the addition of the fusion protein, previous work indicated that fusion protein dependent antimalarial activity could be increased with the addition of a supplemental substrate of mCGL enzymatic activity [8]. Specifically, we hypothesized that the use of the prodrug selenomethionine (setmet) would enhance antimalarial mCGL enzymatic activity. In an in vitro study employing P. yoelii infected erythrocytes, we found that the nontoxic amino acid, setmet, increases the cytotoxic action of the fusion protein (Figure 26). While the natural products of mCGL are relatively nontoxic compounds such as ammonia and α-ketobutrate, the products of the nontoxic prodrug setmet are highly toxic seleno-radical oxygen species (ROS). The number of parasites within samples were enumerated by microscopy following enzyme-prodrug treatment (Figure 27). Samples of infected blood were incubated briefly with the fusion protein. Following this incubation , the samples were washed to remove excess protein and incubated overnight with setmet. We observed that increasing concentrations of setmet decreased the number of observable parasites per field of view (FOV).

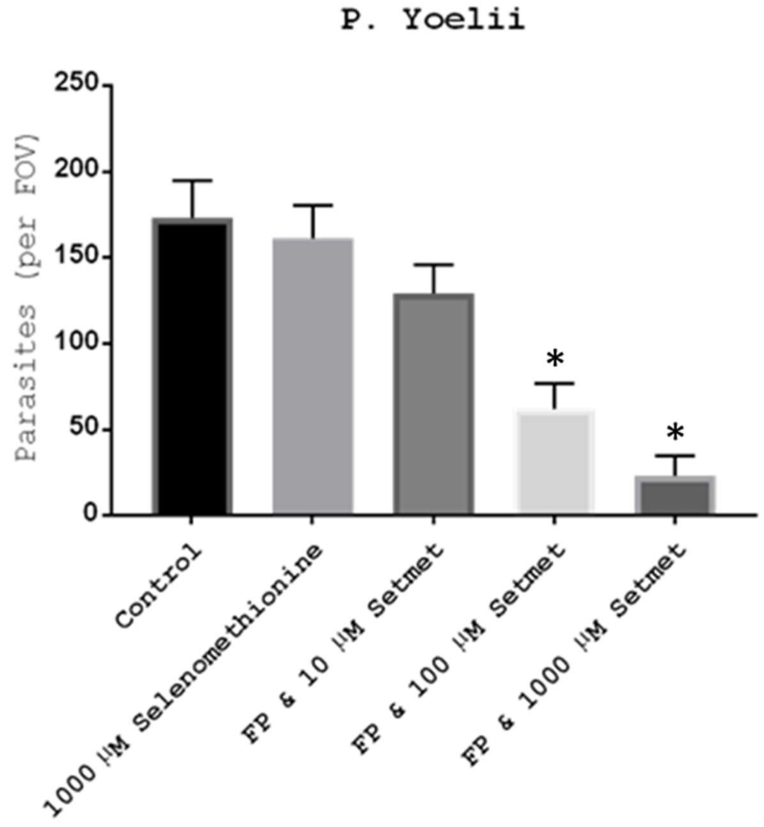

Figure 25: Selenomethionine and parasite viability. The parasite burden of fusion protein (mCGL-ANXA5) treated P. Yoelii infected erythrocyte samples was determined by giemsa stain and histological light microscopy examination. Samples of infected blood were incubated for 3 hours with 100 nM fusion protein to allow binding to parasite surface. Following this brief incubation, the samples were washed to remove excess protein and incubated overnight with various concentrations of the prodrug selenomethionine (setmet). The number of parasites per field of view (FOV) were then enumerated. Data is shown as the mean ± SE (n = 5). Statistical significance between groups is denoted by * ($p < 0.005$).

Using light microscopy of giemsa stained blood smears, we quantified the number of intact P. Yoelii parasites as a function of setmet dose (Figure 26). The addition of a supplemental substrate of mCGL enzymatic activity, (setmet), increased the antimalarial activity of the fusion protein ANXA5-mCGL in vitro. Setmet on its own had no significant effect on the number of parasites observable in cell culture. However, starting at concentrations of 10 μM we observed a decrease in the number of parasites as the dose of setmet was increased to 1 mM. The reported antimalarial activity of selenium derivatives such as selenite and methylselenocysteine is several orders of magnitude less than the activity of setmet in conjunction with ANXA5-mCGL [99, 100]. Furthermore, much previous work examining the antimalarial activity of selenium derivatives has focused on toxic oxides such as selenius acid or sodium selenite. The selenium derivative used in this study, setmet, is an essential amino acid naturally present in the body. Setmet is significantly less toxic than many of these species.

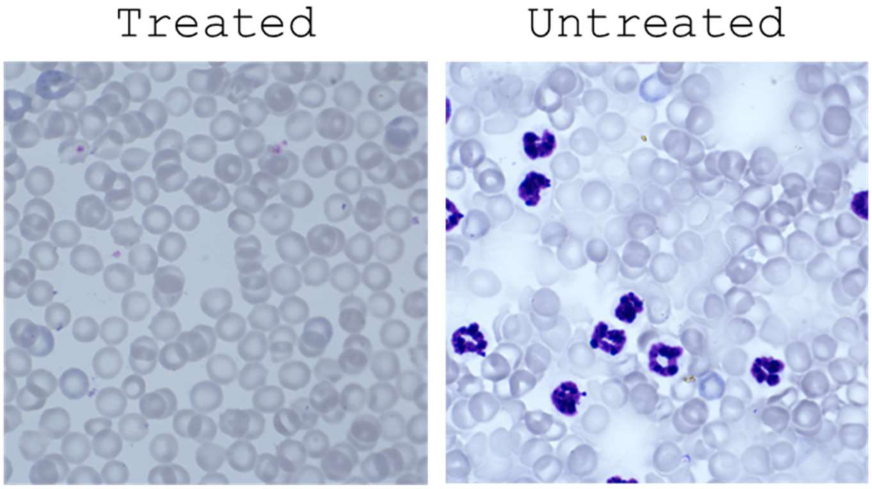

Figure 26: Antimalarial action of fusion protein. Giemsa stained blood slides of uninfected (left) blood following fusion protein treatment and infected (right) untreated erythrocytes. Erythrocytes weakly accumulate giemsa (blue-pink). Parasites within the erythrocyte strongly accumulate giemsa (purple-black). Parasites were quantified by light microscopy.

Plasmodium Berghei Model

In addition to preliminary work with the P. yoelii strain, the antimalarial activity of the fusion protein ANXA5-mCGL was also confirmed in the P. berghei model of infection. P. berghei infected erythrocyte viability was measured using flow cytometry. The fusion protein was found to have significant antimalarial activity in the P. berghei model with CC50 concentrations of 150 and 35 nM after 3 h and 12 h incubations respectively.

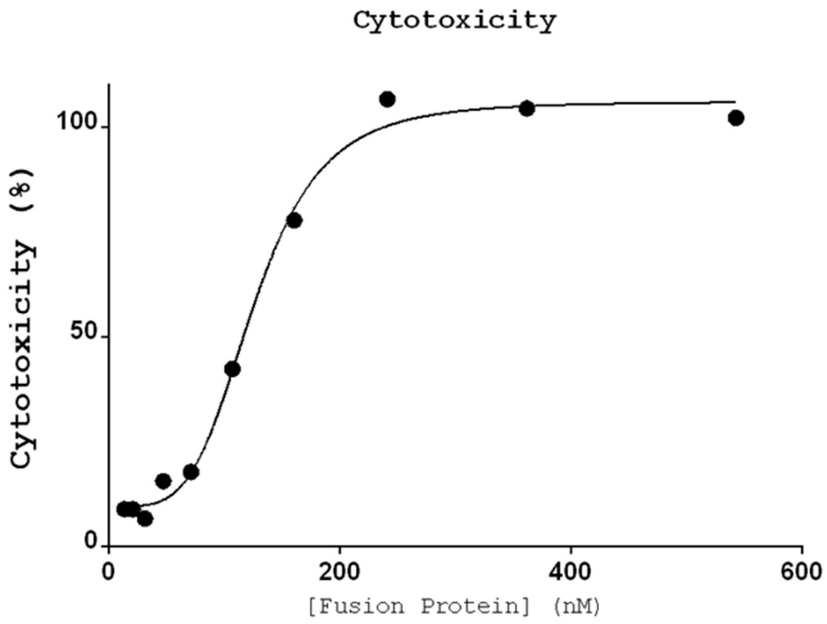

Figure 27: Antimalarial action of fusion protein. The viability of fusion protein (mCGL-ANXA5) treated P. Berghei infected erythrocytes was measured using flow cytometry. Samples of infected erythrocytes were gated to remove the presence of CD45(+) nucleated leukocytes. The leukocyte free population of cells was then gated on recombinant GFP(+) parasites. Nonviable parasites within infected erythrocytes were identified by staining with the cell impermeable nuclear stain propidium iodidie (PI). The cell impermeable PI stain is only capable of staining nucleated cells with compromised cellular membranes PI(+). Nonviable CD45(-)GFP(+)PI(+) parasites were quantified and compared to viable CD45(-)GFP(+)PI(-)parasite control samples after a short-term (3 h) incubation with the fusion protein at 37°C under 5% CO2 supplemented atmosphere. Data is shown as the mean ± SE (n = 3).

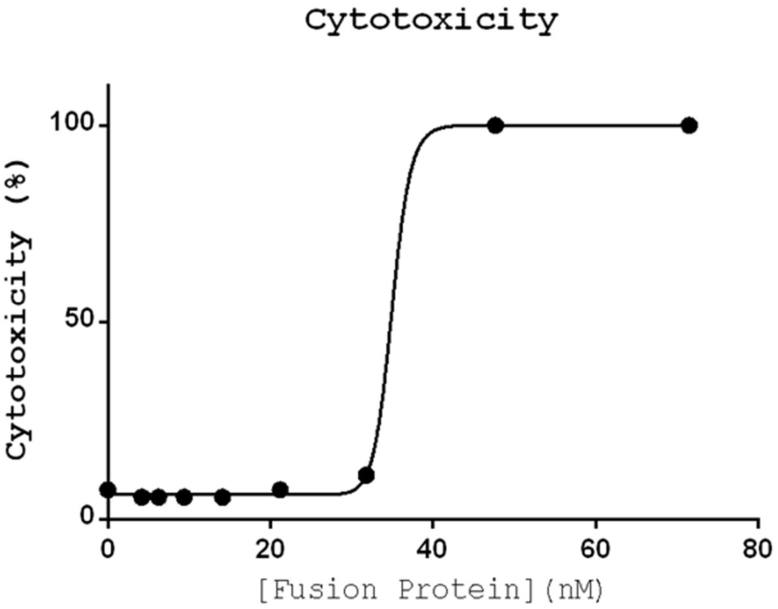

Figure 28: Antimalarial activity of fusion protein. The viability of fusion protein (mCGL-ANXA5) treated P. Berghei infected erythrocytes was measured using flow cytometry. Samples of infected erythrocytes were gated to remove the presence of CD45(+) nucleated leukocytes. The leukocyte free population of cells was then gated on recombinant GFP(+) parasites. Nonviable parasizited erythrocytes were identified by staining with the cell impermeable nuclear stain propidium iodidie (PI). The cell impermeable PI stain is only capable of staining nucleated cells with compromised cellular membranes PI(+). Nonviable CD45(-)GFP(+)PI(+) parasites were quantified and compared to viable CD45(-)GFP(+)PI(-)parasite control samples after an overnight incubation (12 h) with fusion protein using the candle jar method of parasite culture. Data is shown as the mean ± SE (n = 3).

The antimalarial activity of the fusion protein was examined in two-time course studies. In a short-term study of 3 hours, and a longer study of 12 hours, the CC50 concentrations of ANXA5-mCGL were established in the P. berghei model. In the 12-hour cytotoxicity experiment, we confirmed the antimalarial activity we observed in the P. yoelii model. We observed a similar cytotoxicity profile in the P. berghei model, with cytotoxicity starting at 30 nM. Half of all parasites were nonviable at a concentration of 35 nM, and all parasites were apoptotic at a concentration of 40 nM. The similarity between the cytotoxicity profiles in the P. yoelii model and the P. berghei is surprising. The P. berghei model is invariably fatal, whereas the P. yoelii model is nonfatal, and typically responds better to chemotherapeutics. In the 3-hour study we observed parasite toxicity starting at a dose of 50 nM, a CC50 of 150 nM, and no viable parasites were detected at concentrations higher than 250 nM. The observed CC50 of 150 nM is startling. Traditional chemotherapeutics are poisons whose antimalarial effects are measured as the parasite completes multiple lifecycles, and is measured over period of days [101]. A brief examination of the literature demonstrates typical cytotoxicity experiments lasting 48 hours [102-104]. Whereas typicaly chemotherapeutics take several days to kill parasites, the fusion protein ANXA5-mCGL destroys parasites in a time frame of only 3 hours. Furthermore, the antimalarial activity of the fusion protein exceeds that of traditional chemotherapeutics such as chloroquine (CC50: 122 μM; 48 hours) even when measured over a much shorter timeframe [105].

Erythrocyte Damage Index

During initial antimalarial dose-curve experiments with the P. berghei model, we observed dose-dependent damage to erythrocytes (Figure 30). Samples of P berghei infected blood were incubated overnight with fusion protein. Following incubation, samples were fixed, stained with giemsa stain, and examined by DIC light microscopy. Untreated controls (left) maintained their structure. Therapeutic concentrations of fusion protein (100 nM; center) did not alter membrane morphology. Excess fusion protein (10 µM) lead to membrane damage and the production of cell debris. Concerned with the possibility of nontarget destruction of erythrocytes, we evaluated fusion protein dose-dependent erythrocyte damage using histological confirmation, flow cytometry, and absorbance spectroscopy.

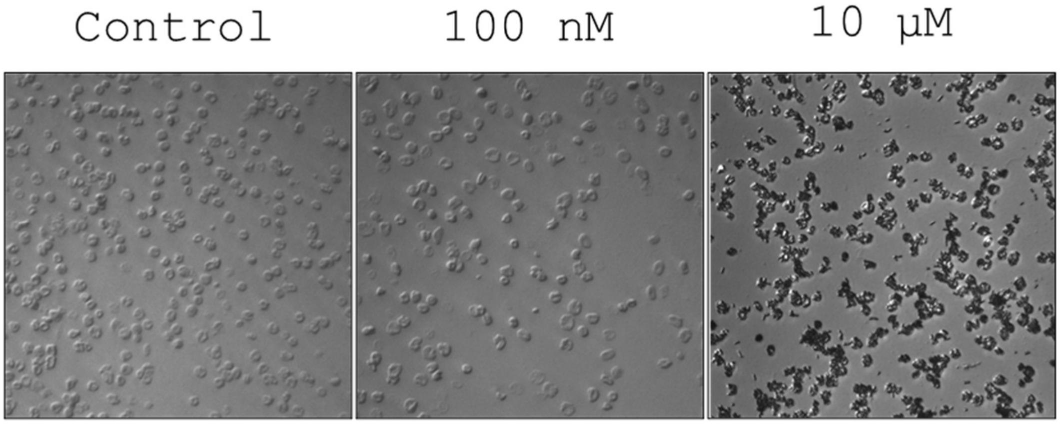

Figure 29: DIC analysis of erythrocyte damage. The fusion protein (mCGL-ANXA5) can damage infected erythrocytes. Untreated infected erythrocytes (untreated; left) maintain their structure. Therapeutic concentrations of fusion protein (100 nM; center) did not alter membrane morphology. A 100-fold increase in fusion protein (10 µM; right) lead to membrane damage and the production of cell debris.

Flow cytometry analysis revealed dose-dependent cell structure changes (Appendix A: Erythrocyte Damage Flow Scheme). Erythroid cells were identified in blood samples as CD45(-)CD71(+) cells, and cell morphology was analyzed by FSC/SSC size gating. Damaged cells were identified grossly as events whose structure deviated from control erythrocyte samples. Following an overnight incubation, we observed a clear relationship between fusion protein dose and cell forward scatter in treated samples. Increasing concentrations of fusion protein clearly decreased cell Forward SCatter (FSC). FSC is a measure of cell surface area. Decreases in FSC reflect a decrease in cell size. Increasing doses of fusion protein shrink erythrocytes in a manner similar to apoptosis. Following this observation, an erythrocyte damage index was defined as the % of structurally damaged cells (Figure 31). Following a short-term (left) or overnight (right) incubation, we observed an increase in cellular debris, and a corresponding decrease in gated erythrocytes. While dose-dependent changes in cell morphology were observed, we note that therapeutic, antimalarial concentrations of fusion protein did not affect cell morphology in vitro. Cell damage was only observed at concentrations in excess of therapeutic concentrations.

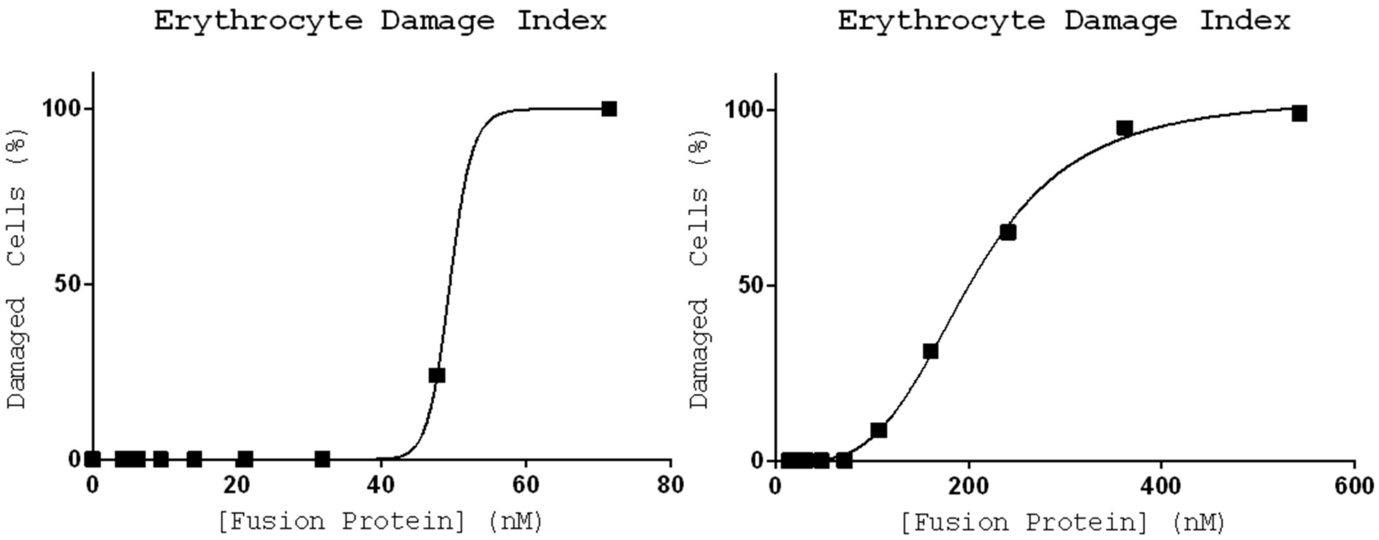

Figure 30: Fusion protein dependent erythrocyte damage. The structure of fusion protein (mCGL-ANXA5) treated P. Berghei infected erythrocytes was assessed using flow cytometry. Erythrocytes were identified in blood samples as CD45(-)CD71(+) cells. Erythrocyte structure was analyzed by flow cytometric FSC/SSC gating. Damaged cells were identified grossly as events that deviated from original gating parameters of healthy erythrocytes. Treated cell samples were analyzed following short-term (left; 3 h) or overnight (right; 12 h) incubation with fusion protein. Increases in fusion protein concentration generated an increase in cellular debris, and a corresponding decrease in gated erythrocytes. Data is presented as the mean ± SE (n = 3).

The fusion protein is capable of damaging CD71(+) erythroid cells as measured by size analysis. In a 3-hour study we observed the onset of size morphology changes in some cells at a dose of 45 nM, significant morphology changes in half of all cells at 50 nM (effect concentration EC50: 50 nM), and the complete loss of structural normality in all cells at a dose of 60 nM. In a 12-hour study, we observed size morphology changes starting at 100 nM, an EC50 of 200 nM, and the complete loss of structural normality in all cells at a dose of 200 nM. While we observed an ANXA5-mCGL dose-dependent change in cell morphology, it is important to note that therapeutic concentrations of the fusion protein are less than the concentrations where erythrocyte damage was observed.

We confirmed the difference between dose-dependent antimalarial and eryptotic action of the fusion protein by histology (Figure 32). Erythrocytes infected with P. berghei were cultured overnight with 50 nM (left) or 100 nM of fusion protein (right). Comparative analysis of giemsa stained slides revealed that 50 nM of fusion protein destroyed infected trophozoites releasing the immature parasites (purple). Erythrocytes maintain normal physiologic appearance at concentrations as high as 50 nM of fusion protein. In contrast, at concentrations of 100 nM there was abundant cell debris and few intact cells.

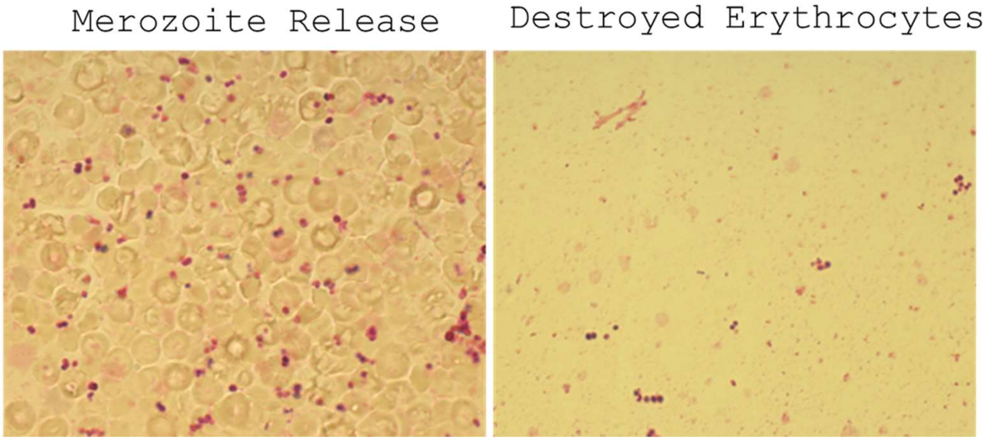

Figure 31: Comparison of fusion protein dose. Erythrocytes infected with P. berghei were cultured overnight (12 hours) with 50 nM (left) or 100 nM of fusion protein (right). Giemsa stained slides revealed that 50 nM of fusion protein destroyed many infected trophozoites releasing the immature parasites (purple). Erythrocytes maintain normal physiologic appearance at this dose. In contrast, cultures of infected blood treated with 100 nM of fusion protein featured few intact cells and abundant cell debris.

Erythrocyte Chemical Damage

Damage to erythrocytes can be measured using multiple methods; one method is the use of spectroscopy to ascertain oxidative damage to hemoglobin. As the chemical unit responsible for carrying oxygen within the erythrocyte, chemical damage to hemoglobin directly impacts the function of the erythrocyte. The use of many antimalarial chemotherapeutics, especially quinine derivatives, has been reported to induce chemical damage to hemoglobin [104, 106]. Oxidative chemical damage to hemoglobin, produces derivatives such as methemoglobin and sulfohemoglobin. While these derivatives are naturally present at low concentrations (~2%), increasing concentrations of these derivatives impair the oxygen carrying capacity of erythrocytes [107]. The derivatives of hemoglobin, sulfohemoglobin and methemoglobin, have unique spectroscopic signatures. Nonfunctional deoxyhemoglobin derivatives, methemoglobin and sulfohemoglobin have maxima absorption at 660 nm in relation to hemoglobin [108, 109]. The relative oxidation state of drug-damaged hemoglobin was determined after 3 h in infected blood by comparative analysis of absorption at 940 and 660 nm (Appendix A: Hemoglobin Oxidation).

Similar to other antimalarial chemotherapeutics, the products of fusion protein antimalarial activity can damage hemoglobin. Dose-dependent oxidation of blood was first observed visually (Figure 33). Untreated blood (left) rapidly acquired a rust brown color when incubated in the presence of excess (10 μM) fusion protein. This color change indicates oxidation of erythrocyte hemoglobin from a Fe^{2+} to Fe^{3+} oxidation state. Enzymatic products of mCGL-ANXA5 include radical oxygen species (ROS) capable of oxidizing blood [110-112]. Using comparative spectroscopic analysis at 940 and 660 nm, we assayed chemical damage to samples of erythrocyte hemoglobin as a log function of fusion protein concentration (Figure 34). The fusion protein did not chemically damage erythrocytes at therapeutic antimalarial concentrations.

Figure 32: Oxidation of infected blood by mCGL-ANXA5. Blood infected with P. berghei was treated with 10 mM fusion protein for 3 h (right) and compared to untreated controls (left). The brown color of the blood incubated with fusion protein indicates the oxidation of hemoglobin.

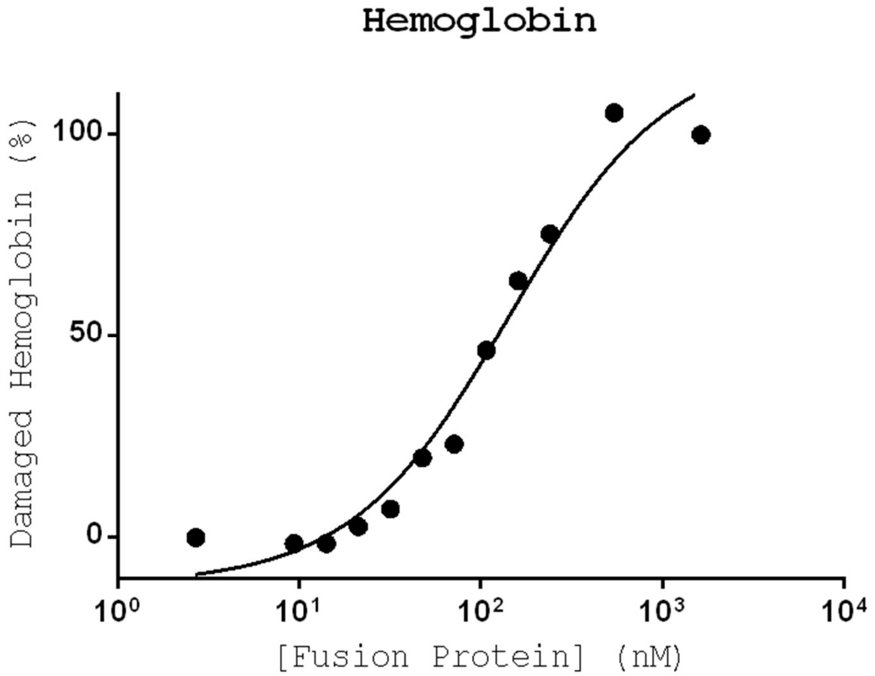

Figure 33: Chemical damage of hemoglobin. Chemical damage of hemoglobin as a function of the concentration of fusion protein was measured as the ratio of absorbances at 990 to that of 660 after 3 hours. The absorbance of blood at 660 and 940 nm corresponds to functional hemoglobin and nonfunctional hemoglobin respectively. Functional hemoglobin carries oxygen (oxyhemoglobin). Nonfunctional hemoglobin derivatives (methemoglobin and sulfohemoglobin) are unable to carry oxygen. Quantifying these two hemoglobin states, the health of erythrocytes was expressed as the fraction of nonfunctional hemoglobin as a function of fusion protein (mCGL-ANXA5) concentration. Data is presented from single points).

We observed ANXA5-mCGL dose-dependent changes in the oxidation state of blood as measured by absorbance spectroscopy. We observed oxidative damage to the hemoglobin of intact erythrocytes starting at a concentration of 30 nM, an EC50 of 0.1 μM, and the complete oxidation of hemoglobin at a concentration of 0.8 μM. Oxidation of hemoglobin occurred at concentrations much higher than those where cell morphology changes were observed, suggesting that the dose limiting factor in ANXA5-mCGL treatment is physical damage to the erythrocyte and not chemical damage to hemoglobin.

In vivo Model

Having both demonstrated the antimalarial activity of the fusion protein in two strains of plasmodium and confirmed the safety of the fusion protein by chemical, histological and cytometric analysis, we proceeded to ascertain the in vivo antimalarial activity of the fusion protein in a P. berghei model. The survival of P. berghei inoculated mice was monitored for a period of one month (Figure 35). All control mice and 50% of treated mice perished within 11 days. At the conclusion of the study (28 days), surviving treated mice were necropsied and confirmed to be parasite free. With half of all mice treated with a single dose were found parasite free at the end of the study; we conclude that they were cured.

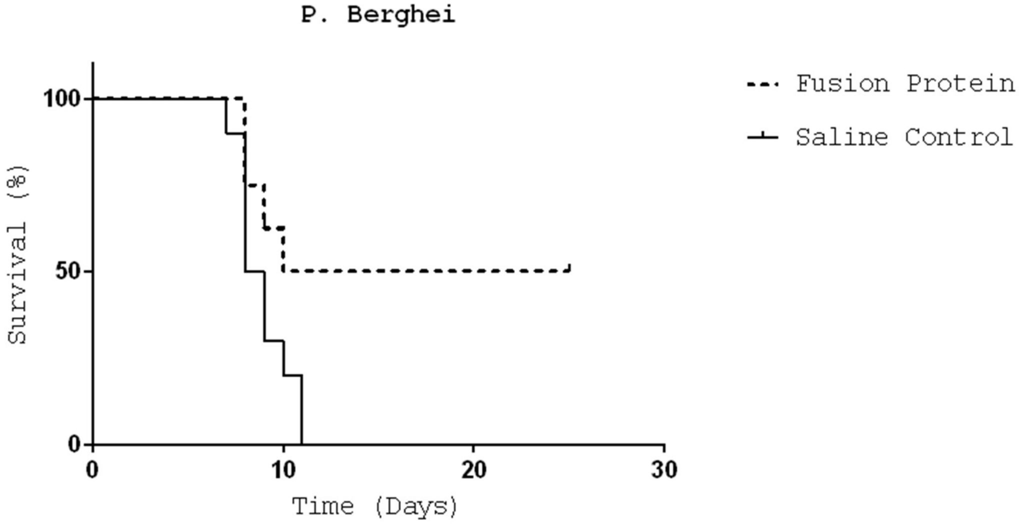

Figure 34: Survival of P. berghei infected mice. The survival of P. berghei inoculated mice was monitored for a period of one month. Male CF-1 mice of 6 weeks of age were inoculated with 10^6 P. berghei infected erythrocytes. Infected mice were treated the following day with 15 mg/kg fusion protein in 150 µL of dPBS or with a saline control. All control mice and 50% of treated mice perished within 11 days. At the conclusion of the study (28 days), surviving treated mice were necropsied and confirmed to be parasite free. Data represents the survival of n = 10 mice.

In addition to observing survival after a single dose, the safety of the fusion protein was confirmed by monitoring mice following daily injections for one month. Weight and behavior were monitored for the presence of adverse side effects. See Figure 36 for weight changes over time. No changes in behavior or weight were observed in mice treated with fusion protein. The rigorous dosing schedule (once per day) as opposed to the experimental treatment schedule (once) highlights the safety of the conjugate.

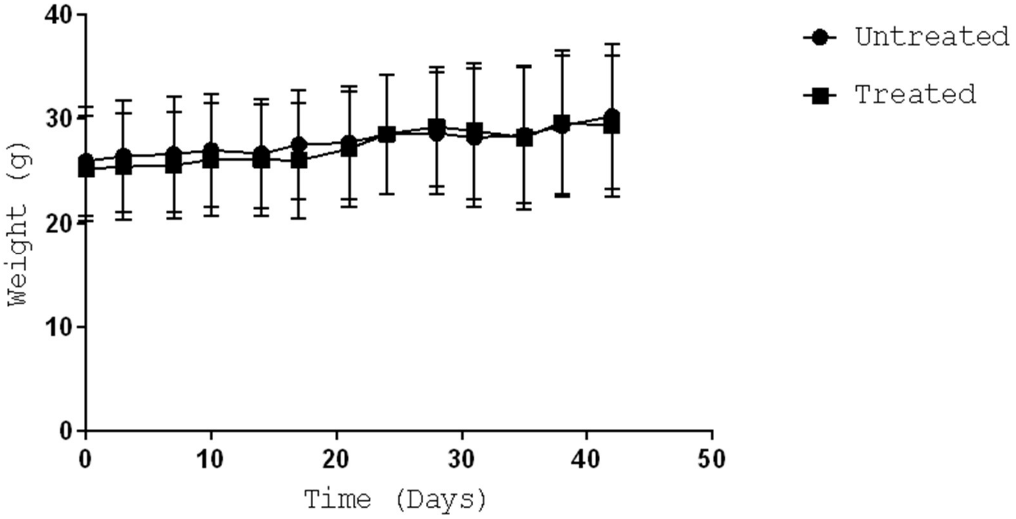

Figure 35: Mouse weight following repeated treatment with fusion protein. The weight of mice receiving daily fusion protein (mCGL-ANXA5) or saline control treatments was monitored over one month. Male outbred swiss CF-1 mice of 6 weeks of age were treated daily with 15 mg/kg of fusion protein for 20 days. Following treatment mice were monitored for 4 weeks to observe any changes in weight of behavior. No changes in behavior or weight were observed in mice treated with fusion protein. Data presented as mean ± SE (n = 4).

Conclusion

There is critical need for new antimalarial drugs. Drug resistant strains of plasmodium, immune to all known pharmaceutic agents, are sweeping across multiple continents endangering billions of people. Here we demonstrate the antimalarial activity of a novel chimeric fusion protein. Comprised of a parasite targeting domain (ANXA5) and a microcidal enzyme (mCGL), the fusion protein specifically binds and destroys parasite infected erythrocytes. The unique mechanism of antimalarial activity, targeting a host marker of cell stress (Ptd-L-Ser), was proven effective in two in vitro models of infection.

In initial experiments we explored the antimalarial activity of the fusion protein in a P. yoelii model of infection. First, we confirmed the localization of fusion protein to infected erythrocytes using fluorescent microscopy. We observed fusion protein accumulation to infected erythrocytes, increasing the effective concentration of the microcidal fusion protein. We then determined the cytotoxic antimalarial activity of the fusion protein (CC50: 40 nM) in a 12 h viability assay. Finally, we demonstrated the synergism of the fusion protein with a prodrug (setmet). Selenium derivatives have demonstrated antimalarial activity, and the synergistic activity of the fusion protein with the prodrug setmet could be a possible second line treatment [99]. Furthermore, using the fatal P. berghei stain we demonstrated again that the fusion protein has tremendous antimalarial activity

(CC50: 35 nM). Interestingly, in short-term tests (12 h) we still observed antimalarial activity, highlighting the rapid antimalarial action of the fusion protein. Further work in vivo with P. berghei demonstrated a significant cure rate with a single dose. Additionally, repeated daily treatments for 20 days failed to illicit weight loss or behavioral changes.

Chapter 45: A Novel Cytostatic Protein-Drug Conjugate Consisting of Annexin A5 and Chlorambucil

Abstract

Here we present a novel cytocidal bioconjugate (ANXA5-CMB) comprised of the protein annexin A5 (ANXA5) and the alkylating agent chlorambucil (CMB). The protein component, ANXA5, serves as a vehicle specifically targeting chlorambucil to tumor cells. The antineoplastic activity of the mustard derivative CMB is enhanced by ANXA5 dependent tumor targeting delivery. We demonstrate the synthesis and analysis of this novel ANXA5-CMB conjugate. Furthermore, we establish the anticancer activity of the conjugate in vitro using four cell lines, and in vivo with two murine tumor models.

Introduction

Chlorambucil(CMB) was linked to annexin A5 (ANXA5) using 1-Ethyl-3-(3-dimethylaminopropyl) carbodiimide (EDC) and N-hydroxysuccinimide (NHS). CMB is unique among FDA approved chemotherapeutics. It is the only chemotherapeutic with a single carboxylic group and no primary amine groups (Figure 36). By selectively activating the carboxylic group of CMB and then quenching EDC-NHS chemistry before the addition of ANXA5, it is possible to perform a one pot synthesis of ANXA5-CMB without the formation of undesired crosslinking products (Figure 37). In typical bioconjugation schema employing other chemotherapeutics, side reactions such as protein-protein and drug-drug crosslinking produce undesired biproducts, reducing yield. Additionally, the cytocidal functional groups of CMB are the bis(2-chloroethyl)amino arms [58]. Linking chlorambucil by the carboxylic group does not impact cytocidal activity; in fact the bioconjugate was up to 100-fold more cytotoxic than free CMB.

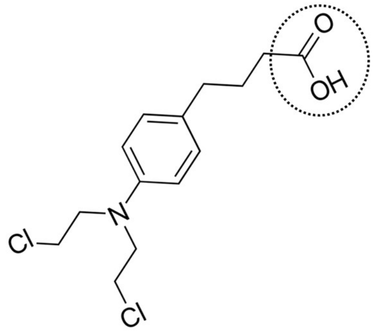

Figure 36: Chlorambucil chemical structure, and linking moiety (circle). The nitrogen mustard chlorambucil (MW: 304.2 Da) is unique among FDA approved cancer drugs. It is the only antineoplastic agent with a single carboxylic functional group and no primary or secondary amine.

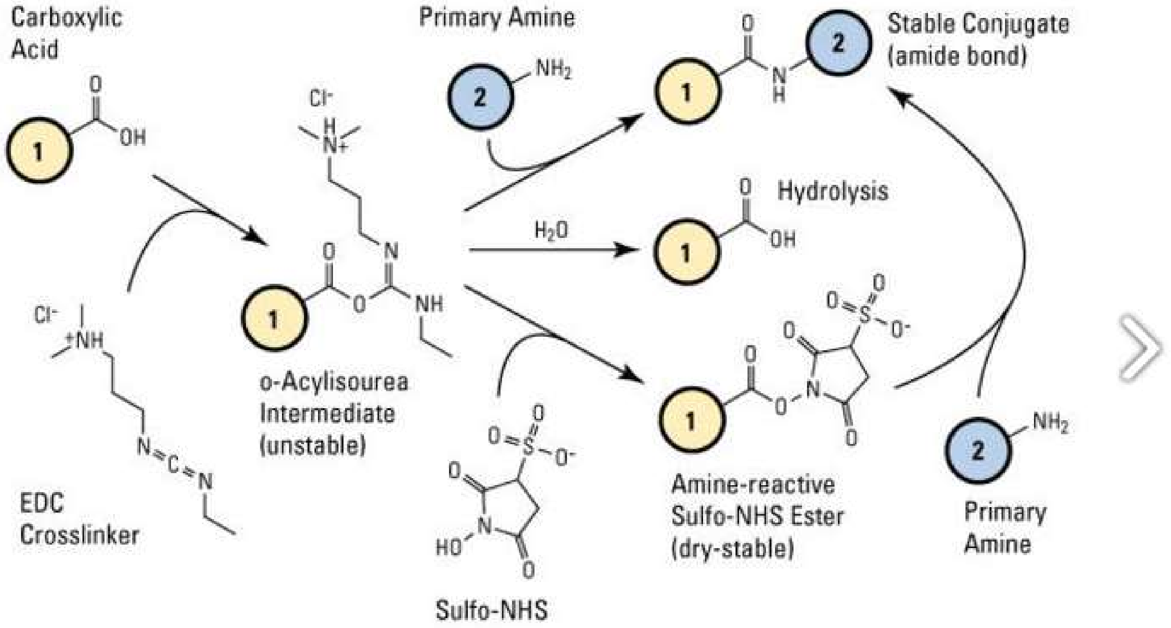

Figure 37: Chemical Synthesis of CBM-EDC and then CBM-NHS. The NHS derivative (1) was the conjugated to ANXA5 (2) creating a peptide bond. *Thermofisher.com*

Materials and Methods

Materials

An AXA5 vector was previously constructed as part of a pET-30 Ek/LIC plasmid using Gibson fragment assembly cloning [46]. Bovine serum albumin (BSA), Alamar Blue reagent, Triton X-100, EDTA, TPCK, EDC, NHS, β-mercaptoethanol, PMSF, and Tris-acetate-EDTA buffer were from Sigma-Aldrich (St Louis, MO). His-trap columns were from GE Healthcare (Chicago, IL). Sodium phosphate, and sodium dodecyl sulfate (SDS) were from Mallinckrodt Chemicals (Phillipsburg, NJ). Chlorambucil was from TCI America (Portland, OR). HPLC grade ethanol was from Acros Organics (Waltham, MA). Antifade reagent Fluoro-gel, borate buffer, HOIESCHT stain, FITC, Alexa-488, Deep Red Plasma Membrane stain, DAPI, Propidium Iodide, flow cytometry staining buffer, fixation/permeabilization buffer, permeabilization buffer, and Slide-A-Lyzer dialysis cassettes (3.5 kDa) were from Thermo Fisher Scientific (Waltham, MA). The 2 and 100 kDa dialysis membranes were from Spectrum Laboratories (Rancho Dominguez, CA). Roswell Park Memorial Institute cell medium (RPMI-1640), Weymouth's MB 753/10 medium, and Hank's balanced salt solution were from ATCC (Manassas, VA). Fetal bovine serum (FBS) was from Atlanta Biologicals (Lawrenceville, GA). Tryptone, yeast extract, and kanamycin monosulfate were obtained from Alfa Aesar (Haverville, MA). Sodium hydroxide, potassium chloride, and sodium chloride were from VWR inc (Radnor, PA). HRV-C3 protease was from Sino biologics (Wayne, PA).

EDC/NHS Coupling

Chlorambucil (CMB) was linked to the protein annexin A5 (ANXA5) by a zero-length carbodiimide linker (Figure 37) . Insoluble at neutral pH, 10 mg of chlorambucil was initially dissolved in 15 µL of an acidic solution of 12 M HCl . This solution of chlorambucil salt was then immediately diluted 200-fold in 30 mM phosphate buffer. Using 10 mg/mL 1-ethyl-3-[3-dimethylaminopropyl]carbodiimide hydrochloride (EDC), the carboxylic group of chlorambucil was modified with an unstable O-acylisourea intermediate. This intermediate was then stabilized with the addition of 7 mg/mL N-hydroxysulfosuccinimide (sulfo-NHS). The reactants were vigorously vortexed for 15 minutes to facilitate sulfo-NHS-CMB conjugation. The EDC/NHS crosslinking reaction was then quenched with 2 µL/mL of β-mercaptoethanol. If EDC/NHS is not quenched, carboxylic groups such as those on aspartate and glutamate on ANXA5 may be activated in following steps, leading to protein-protein crosslinking (Figure 38).

The synthesized sulfo-NHS-CMB derivative reacts readily with the primary amines of annexin A5 such as those on lysine (Figure 39). The activated chlorambucil was linked to annexin A5 by incubating 2.5 mL of 1 mg/mL annexin in 30 mM phosphate buffer with 1 mL of the sulfo-NHS-CMB derivative. The pH of the solution was then immediately titrated to 7.4. The sulfo-NHS-CMB derivative and annexin A5 were then gently mixed for 12 hours. Following conjugation, the solution was centrifuged for 10 minutes at 12000 g to remove precipitates. The resulting supernatant was dialyzed against 2 L of 30 mM phosphate buffer for 8 hours. The dialysate was then filtered through a 0.22 µm filter and stored at 4 °C for 48 hours protocol is given in Appendix B.

Protein yields were calculated by Bradford assay.

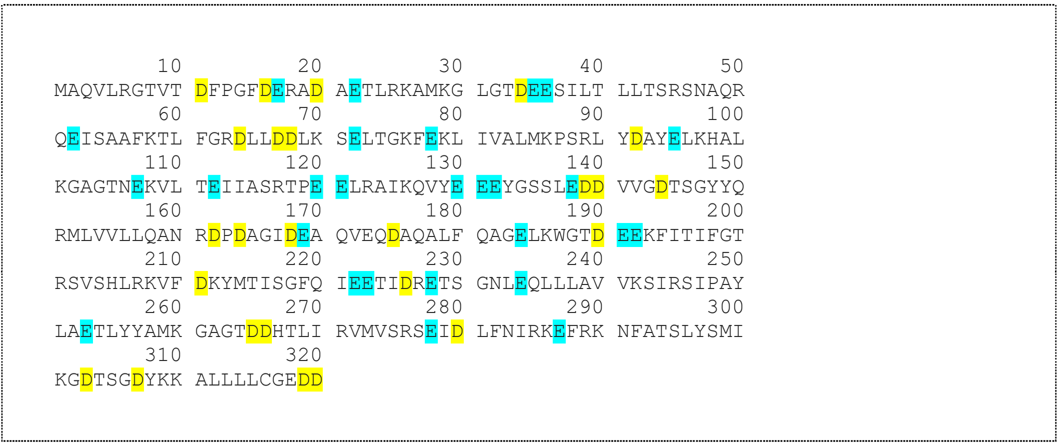

```
        10         20         30         40         50
MAQVLRGTVT DFPGFDERAD AETLRKAMKG LGTDEESILT LLTSRSNAQR
        60         70         80         90        100
QEISAAFKTL FGRDLLDDLK SELTGKFEKL IVALMKPSRL YDAYELKHAL
       110        120        130        140        150
KGAGTNEKVL TEIIASRTPE ELRAIKQVYE EEYGSSLEDD VVGDTSGYYQ
       160        170        180        190        200
RMLVVLLQAN RDPDAGIDEA QVEQDAQALF QAGELKWGTD EEKFITIFGT
       210        220        230        240        250
RSVSHLRKVF DKYMTISGFQ IEETIDRETS GNLEQLLLAV VKSIRSIPAY
       260        270        280        290        300
LAETLYYAMK GAGTDDHTLI RVMVSRSEID LFNIRKEFRK NFATSLYSMI
       310        320
KGDTSGDYKK ALLLLCGEDD
```

Figure 38: Possible locations of EDC/NHS crosslinking in ANXA5**.** Aspartate (blue) and glutamate (yellow) carboxylic moieties within the amino acid sequence of ANXA5 are possible locations of protein-protein crosslinking.

```
        10         20         30         40         50
MAQVLRGTVT DFPGFDERAD AETLRKAMKG LGTDEESILT LLTSRSNAQR
        60         70         80         90        100
QEISAAFKTL FGRDLLDDLK SELTGKFEKL IVALMKPSRL YDAYELKHAL
       110        120        130        140        150
KGAGTNEKVL TEIIASRTPE ELRAIKQVYE EEYGSSLEDD VVGDTSGYYQ
       160        170        180        190        200
RMLVVLLQAN RDPDAGIDEA QVEQDAQALF QAGELKWGTD EEKFITIFGT
       210        220        230        240        250
RSVSHLRKVF DKYMTISGFQ IEETIDRETS GNLEQLLLAV VKSIRSIPAY
       260        270        280        290        300
LAETLYYAMK GAGTDDHTLI RVMVSRSEID LFNIRKEFRK NFATSLYSMI
       310        320
KGDTSGDYKK ALLLLCGEDD
```

Figure 39: Lysine (yellow) residues with a primary amine. The lysine residues within ANXA5 are a possible location of protein-protein crosslinking in EC/NHS chemistry and the target of CMB modification.

Quantification of Chlorambucil

The concentration of chlorambucil can be determined by the synthesis and quantification of a photocatalyzed chlorambucil derivative. Standards of chlorambucil were solubilized in an acidic solution of 12 M HCl acid and diluted 200-fold in a solution of 30 mM phosphate buffer and 10% DMSO. Samples were then incubated in a UV RMR-500 photochemical reactor for 1 hour. The UV-catalyzed cyclic addition of DMSO to chlorambucil generates a perhydrothiazocine derivative (Figure 40).

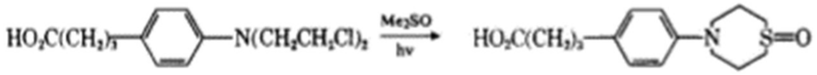

Figure 40: Synthesis of perhydrothiazocine. The perhydrothiazocine derivate is fluorescent (358/434; ex/em). Fluorescence was measured on a microtiter plate reader (360/460; ex/em) and found to be proportional to concentration.

Cell Lines and Cell Culture

Drug resistant, triple-negative 4T1 breast cancer cells from ATCC (Manassas, VA) were transfected with tdTomato (Td) previously [6]. 4T1-Td breast cancer cells were cultured in Roswell Park Memorial Institute (RPMI-1640) medium supplemented with 10 % FBS and 1% penicillin/streptomycin antibiotics (100 U mL^{-1} and 100 $\mu g/mL^{-1}$ respectively). EMT6 breast cancer cells were cultured in Waymouth's MB 752/1 medium supplemented with 2 mM L-glutamine and 15% FBS. Nonadherent L1210 lymphocytic leukemia and P388 lymphoblastic lymphoma cells were cultured in Dulbecco's modified eagle's medium (DMEM) with supplemental glucose enriched with 10 % FBS, and 1% penicillin/streptomycin antibiotics (100 U mL^{-1} and 100 $\mu g/mL^{-1}$ respectively). All adherent cells were passaged using 0.25 % (w/v) Trypsin in 0.53 mM EDTA. All cells were grown at 37 ° C and 100% humidity under 5 % CO_2.

In vitro Cytotoxicity studies

Cells (5000 cells/well) were seeded and cultured for 48 hours in 96 well microtiter plates. Cells were then incubated with chlorambucil or the protein conjugate for 24 hours. Following incubation cell viability was assayed by AlamarBlue assay as previously described [46].

Mouse Tumor models

All procedures were conducted under protocols approved by the Institutional Animal Care and Use Committee (IACUC) of the University of Oklahoma. Two strains of mice were employed to assay two different types of cancer. The first strain was female BALB/cj mice from JAX (Frenchman Bay, ME) at six weeks of age. These mice were used in conjunction with the breast cancer cell lines 4T1 and EMT6. The second strain employed was male DBA mice from Charles River (Lebanon, CT) of six weeks of age. These mice were used in conjunction with the lymphoblastic leukemia, P388 and L1210, cell lines. In breast cancer studies, mice were injected s.c. in the 4th mammary fat pad with 5×10^4 4T1 or EMT6 mammary carcinoma cells in a 100 µl suspension of saline on day 0. Tumor volumes were recorded twice weekly to ascertain progression of the disease. Mouse tumor volumes were determined by the formula [V=1/2*L*W^(2)]. In leukemia studies mice received an i.p. inoculation with 10^6 L1210 or P388 lymphoblastic leukemia cells in a 100 µL suspension of saline on day 0. Leukemia progression was monitored by survival and necropsy. Mice received doses of 10 µg of chlorambucil as part of a free salt or as part of a protein – drug conjugate. The annexin A5 – chlorambucil conjugate was administered daily for the duration of the study.

Statistical Analysis

Data was analyzed with Graphpad Prism software. Statistical significance of parasite cytotoxicity was assessed using a one-way ANOVA and Tukey-Kramer multiple comparisons test. Statistical significance of survival curves was determined by the Gehan-Breslow-Wilcoxon test and Mantel-Haenszel log-rank test. Multiple comparisons were corrected by the Bonferroni threshold. Samples were n = 5 unless otherwise listed, outliers as dertermined by the Tietjen-Moore tests were no included in the sample numbers. Error is represented graphically as standard error unless error did not exceed the size of the plotted mean point symbol in which case the bars were excluded for clarity.

Results and Discussion

Synthesis of ANXA5-CMB

Synthesis of an ANXA5-CMB conjugate was confirmed using SDS-gel electrophoresis (Figure 41). Three samples were run between two protein ladders. ANXA5 (left; MW:36 kda) and two separate batches of ANXA5-CMB conjugate (center and right; MW:40 kDa) demonstrate the increase in molecular weight as chlorambucil (MW:0.302 kDa) is covalently attached to the annexin A5. Molecular weights of the band above and the band below the samples are 53 and 35 kDA respectively. We observed an increase in MW of approximately 3 kDA following the synthesis of ANXA5-CMB.

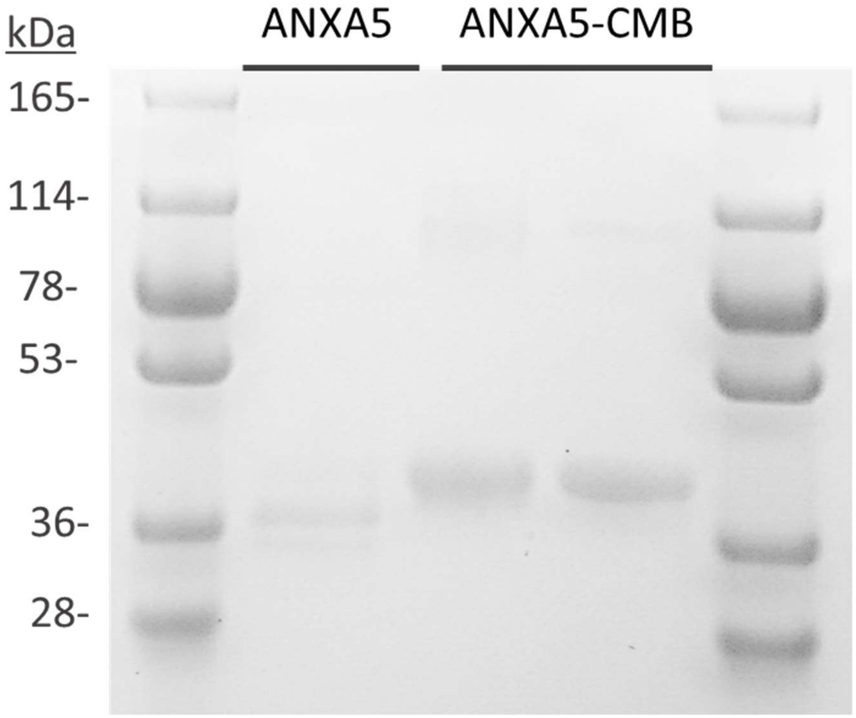

Figure 41: Molecular weight of ANXA5 (left) and ANXA5-CMB (right). Synthesis of a chlorambucil – annexin A5 conjugate was confirmed using SDS-gel electrophoresis. Three samples were run between two ladders. Annexin A5 (left; MW:36 kDa) and two batches of chlorambucil - annexin A5 conjugate (center and right; MW:40 kDa) demonstrate the increase in molecular weight as chlorambucil (MW:0.302 kDa) is covalently attached to the annexin A5. Molecular weights of the band above and the band below the samples are 53 and 35 kDA respectively

The EDC/NHS linking chemistry does not contribute the molecular weight of the ANXA5-CMB construct. Any increase in molecular weight is the result of CMB addition to ANXA5. Therefore, the molecular weight of the resulting ANXA5-CMB conjugate can only increase by a factor of CMB's molecular weight. The molecular weight of CMB is 304 Da. Using gel-electrophoresis, we observe an increase in ANXA5 molecular weight from 36 kDa to about 40 kDa. This increase of about 4 kDa corresponds to the addition of 13 CMB to each annexin. Furthermore, we observe no smearing of the protein bands in the ANXA5-CMB groups. Band smearing is indicative of the formation of side products such as ANXA5-ANXA5 polymers during the synthesis of ANXA5-CMB. Band smearing would also indicate CMB heterofunctionalization of ANXA5 producing ANXA5-CMB derivatives of various molecular weights. In two different batches of ANXA5-CMB we observe a sizable change in molecular weight, and the production of a relatively pure product.

The extent of CMB addition to ANXA5 was also confirmed by fluorescent assay. The ANXA5-CMB conjugate samples were incubated under UV-light with 5 % DMSO to generate a fluorescent derivative of CMB. The formation of the fluorescent derivative, perhydrothiazocine, by photocatalyzed cyclic addition of DMSO allowed the quantification of CMB on ANXA5 (Figure 42). Using this method we determined a molar ratio of typically 8-12 CMB per ANXA5. This corresponded to roughly a mass value of 10% CMB (m/m %) in the ANXA5-CMB conjugate.

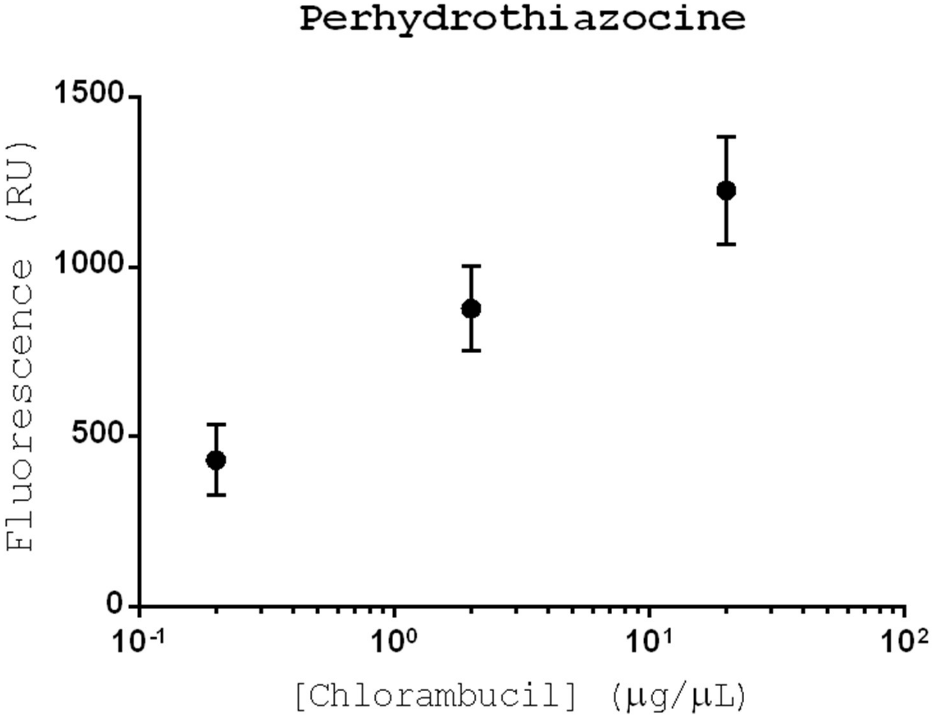

Figure 42: Log[CMB]-perhydrothiazocine fluorescence quantification. An unknown concentration of chlorambucil can be determined with fluorescent spectroscopy. When chlorambucil is in the presence of DMSO, UV light catalyzes the production of fluorescent perhydrothiazocine (358/434; ex/em). The excitation and emission of perhydrothiazocine was measured (360/460; ex/em) and found to be proportional to concentration. Samples depicted as mean ± SE (n = 3).

ANXA5-CMB Binding

The accumulation of ANXA5-CMB in tumor cells was first demonstrated in B-cell derived lymphocytic L1210 cells using an ANXA5-fluorescein isothiocyanate (FITC) derivative. ANXA5 was functionalized with FITC, a fluorescent label of similar weight and hydrophobicity to CMB. Fluorescent imaging of L1210 cells incubated with ANXA5-FITC demonstrated the accumulation of ANXA5-FITC (green) to Deep Red Plasma Membrane stained L1210 (red) cells (Figure 43).

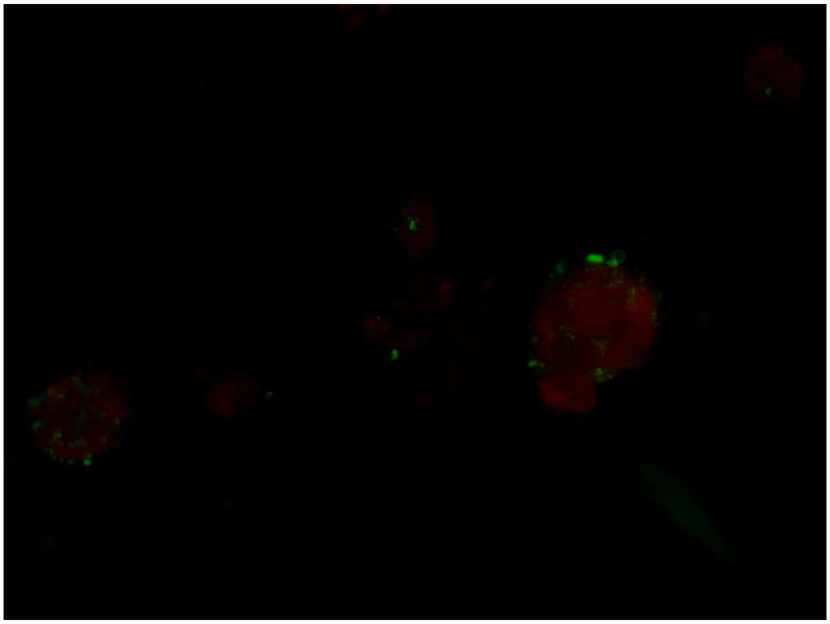

Figure 43: FITC-ANXA5 (green) indicates the presence of ANXA5 on the membrane of L1210 cells statined with Deep Red Plasma Membrane Stain (red).

The accumulation of ANXA5-CMB was also indirectly confirmed by fluorescent analysis of perhydrothiazocine formation. The UV catalyzed heterocyclic ring formation of perhydrothiazocine from chlorambucil and DMSO creates a green fluorescent derivative. The accumulation of chlorambucil-protein conjugate to L1210 cells was demonstrated in this manner (Figure 44).

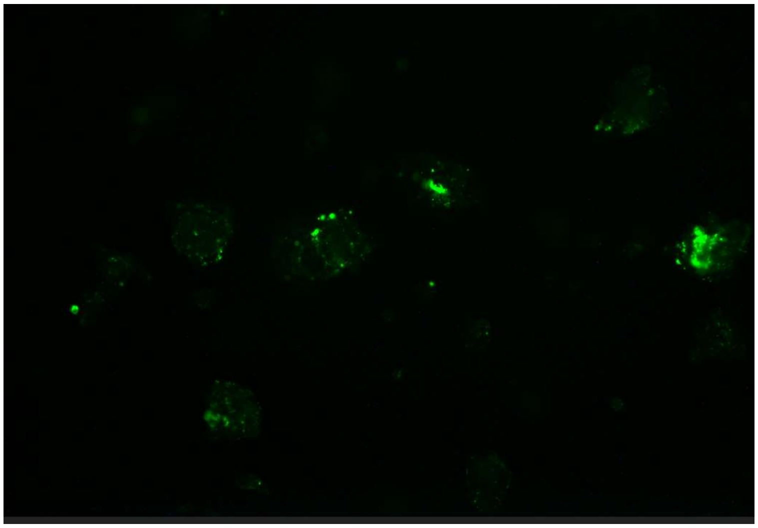

Figure 44: Photocatalyzed luminescent ANXA5-CMB (green) binding L1210 leukemia. The UV catalyzed heterocyclic ring formation of perhydrothiazocine from chlorambucil and DMSO creates a fluorescent derivative. The accumulation of chlorambucil-protein conjugate to L1210 cells was demonstrated in this manner. Cells were incubated with chlorambucil – annexin A5 conjugate briefly (3 h), and then fixed in 4% paraformaldehyde. Samples were then incubated under UV light (20 W for 1 h) to develop fluorescence. Cells were then imaged.

Acute Lymphocytic Leukemia

Having confirmed the localization of ANXA5-CMB to L1210 leukemia cells, we undertook an assay of bioconjugate cytotoxicity. The viability of L1210 leukemia cancer cells treated with either chlorambucil or a chlorambucil-protein conjugate was assayed after 24 hours (Figure 45). Cells were incubated with chlorambucil (CMB) or chlorambucil-annexin A5 conjugate (ANXA5-CMB). The conjugate (squares) was significantly more potent than the free chlorambucil (circles) ($P \leq 0.005$). The 50 % cytotoxic concentration was 10 μM for CMB and 1 μM for ANXA5-CMB, a 10-fold difference.

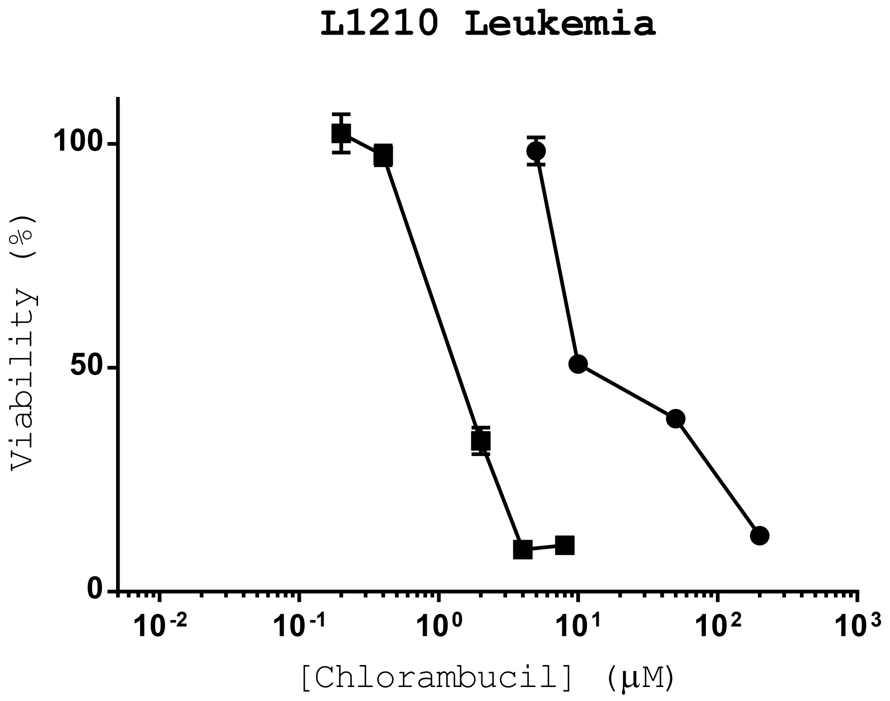

Figure 45: Comparative cytotoxicity of L1210 leukemia. The viability of L1210 leukemia cancer cells treated with either chlorambucil (circles) or a chlorambucil-protein conjugate (squares) was assayed by alamarBlue after 24 hours. Cells were incubated with chlorambucil (CMB) or chlorambucil-annexin A5 conjugate (CMB-ANXA5). The conjugate (circles) was significantly more potent than the free chlorambucil (squares). The full viability curve of chlorambucil was truncated by physical limitations (solubility ~300 mM). Data depicted as mean ± SE (n = 8). Error bars omitted for clarity if SE was smaller than the point symbol.

Following initial results in the L1210 model of leukemia, the cytocidal activity of the ANXA5-CMB conjugate was determined in a second cell mode using the macrophage derived lymphocytic lymphoma cell line P388 (Figure 46). The viability of P388 lymphoblastic lymphoma cancer cells treated with either chlorambucil or a chlorambucil-protein conjugate was assayed after 24 hours. Again in a second model of leukemia, the conjugate (circles) was significantly more potent than the free chlorambucil (squares)($P \leq 0.005$). The CC50 was 60 μM for CMB compared to 2 μM for ANXA5-CMB, a 30-fold difference.

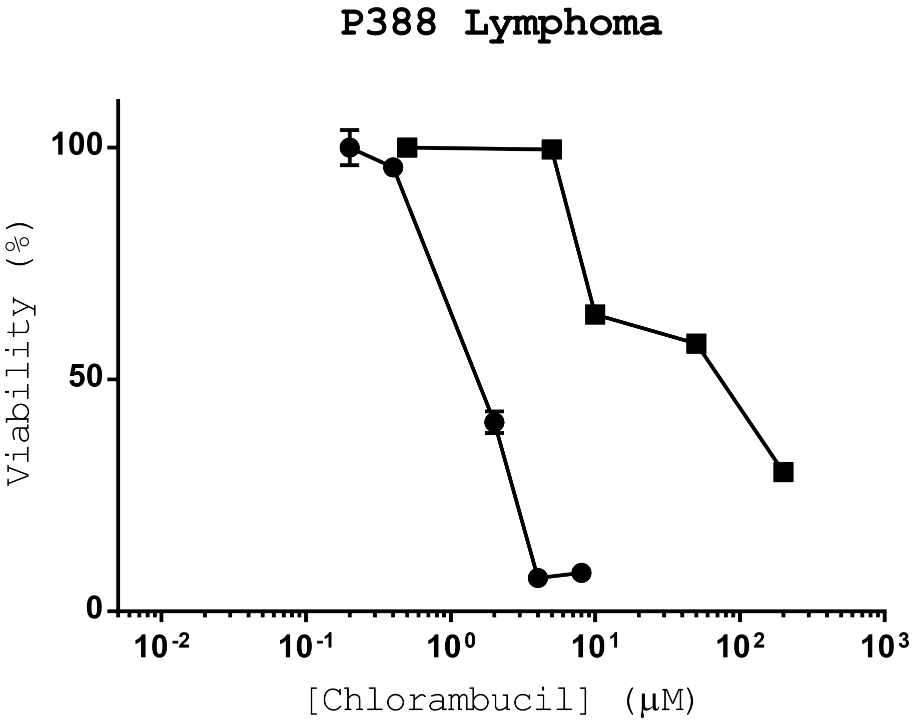

Figure 46: Comparative cytotoxicity of CMB (circles) and ANXA5-CMB (squares). The viability of P388 lymphoblastic lymphoma cancer cells treated with either chlorambucil or a chlorambucil-protein conjugate was assayed by alamarBlue after 24 hours. Cells were incubated with chlorambucil (CH) or chlorambucil-annexin A5 conjugate (ANXA5-CMB). The conjugate (circles) was significantly more potent than the free chlorambucil (squares). The full viability curve of chlorambucil was truncated by physical limitations (solubility ~300 mM). Data is presented as the mean ± SE (n = 12). Error bars omitted for clarity if SE was smaller than the point symbol.

The cytocidal activity of ANXA5-CMB was established in two models of acute lymphocytic leukemia. In the L1210 and P388 models CMB was a poor inducer of cell death. The full cytotoxicity profile of CMB was unable to be constructed due to solubility limitations. The chemotherapeutic CMB is insoluble in water. Even with the aid of a dimethyl sulfoxide cosolvent, the highest concentration of CMB aachieved as only 300 μM. We note that the ANXA5-CMB conjugate was fully soluble in water and not precipitation was observed at concentrations of CMB as high as 10 μM.

Following promising in vitro results, we undertook an in vivo assay of ANXA5-CMB antineoplastic activity using the L1210 cell line in a mouse model (Figure 47).

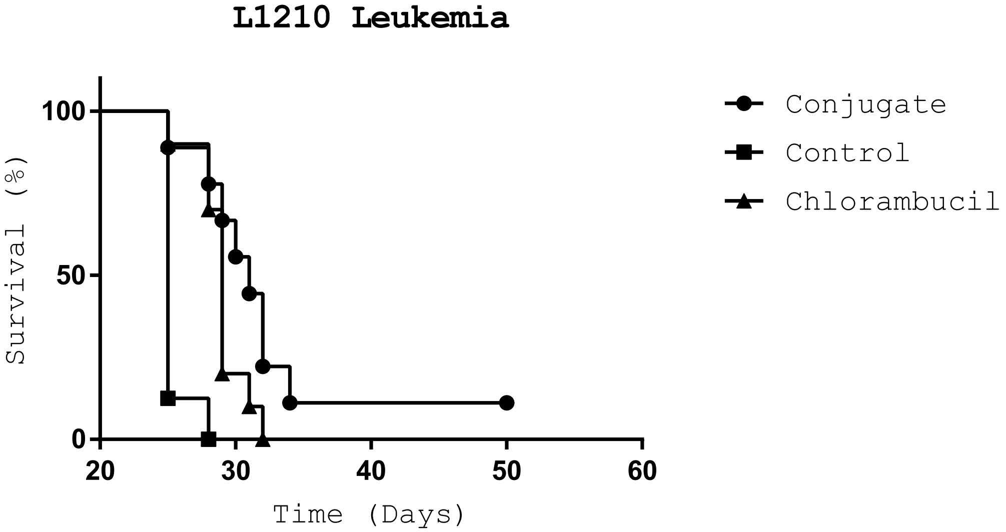

Figure 47: <u>ANXA5-CMB dependent survival increase in a L1210 model.</u> The survival of 6 week old male DBA mice inculcated with 10^5 L1210 leukemia cells was monitored for 7 weeks. Mice received either daily doses of 20 µg of chlorambucil as a free agent or as part of a protein – drug conjugate, which started 2 days after innoculation. The annexin A5 – chlorambucil conjugate performed significantly better than free chlorambucil, significantly improving survival. Data presented as mean ± SE (n = 9).

Chlorambucil (median survival: 29 d) significantly increased the survival of mice bearing L1210 lymphocytic leukemia (median survival 29 d) as measured by the Mantle-Cox Test (P = 0.0004) and the Gehan-Breslow-Wilcoxon Test (P = 0.0005). Additionally, the protein conjugate ANXA5-CMB (median survival: 31 d) significantly increased the survival of mice bearing L1210 tumors (median survival 29 d) as measured by the Mantel-Cox Test (P = 0.0004) and the Gehan-Breslow-Wilcoxon Test (P = 0.0007). While the ANXA5-CMB conjugate did not significantly increase survival when compared to CMB as measured by the Mantel-Cox Test (P = 0.08) or the Gehan-Breslow-Wilcoxon Test (P = 0.12), one mouse appeared to have full tumor regression and to date has survived greater than 100 days tumor free. Furthermore, an analysis of the confidence intervals reveals that an increase in median survival of 1 day in the ANXA5-CMB group would have likely yielded significant differences between the two groups. Significance could easily be achieved by increasing the number of animals or increasing the dose of CMB-ANXA5. Further work is needed to optimize the in L1210 in vivo model.

Adverse Effects

The ANXA5-CMB conjugate has significant antineoplastic activity both in vitro and in vivo. A typical side effect of potent mustard derived agents is lowered white blood cell counts (WBCC). Lowered WBCC or leukopenia, is a deadly side effect. After observing ANXA5-CMb cytocidal activity in both macrophage and B-cell derived tumor cell lines, we investigated the effect of the conjugate on healthy mouse WBCC (Figure 48). We assayed the effect of ANXA5-CMB on WBCC male DBA/2 mice of 10 weeks of age treated daily with 20 µg of ANXA5-CMB. No changes in WBCC (purple cells) was observed in conjugate treated animals (left) compared with saline mock treatments (right) after seven daily treatments.

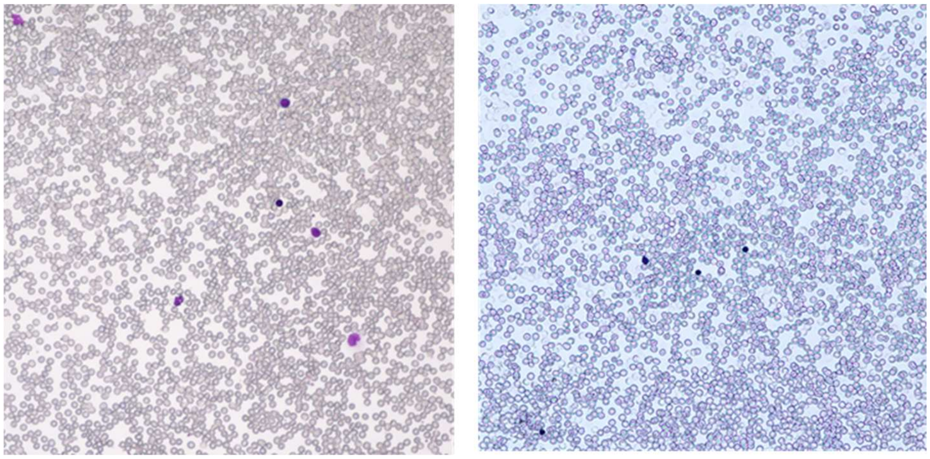

Figure 48: Comparison of control (left) and treated (right) WBCC in thin-film blood smears. The chlorambucil- annexin ANXA5 conjugate does not induce leukopenia (low WBCC) in mice. Mice treated daily with 20 µg of chlorambucil conjugate (left) did not have statistically different WBCC after seven daily treatments (n = 3; 5 F.O.V.) .

Metastatic Breast Cancer

Having observed ANXA5-CMBN cytocidal activity in nonsolid murine tumor models of lymphocytic lymphoma, we furthermore assayed the antitumor activity of the conjugate in several solid tumor models. First, the viability of EMT6 breast cancer cells treated with either chlorambucil or a chlorambucil-protein conjugate was assayed after 24 hours (Figure 49). Cells were incubated with chlorambucil (CMB) or chlorambucil-annexin A5 conjugate (ANXA5-CMB). The conjugate (squares was significantly more potent than the free chlorambucil (circles).

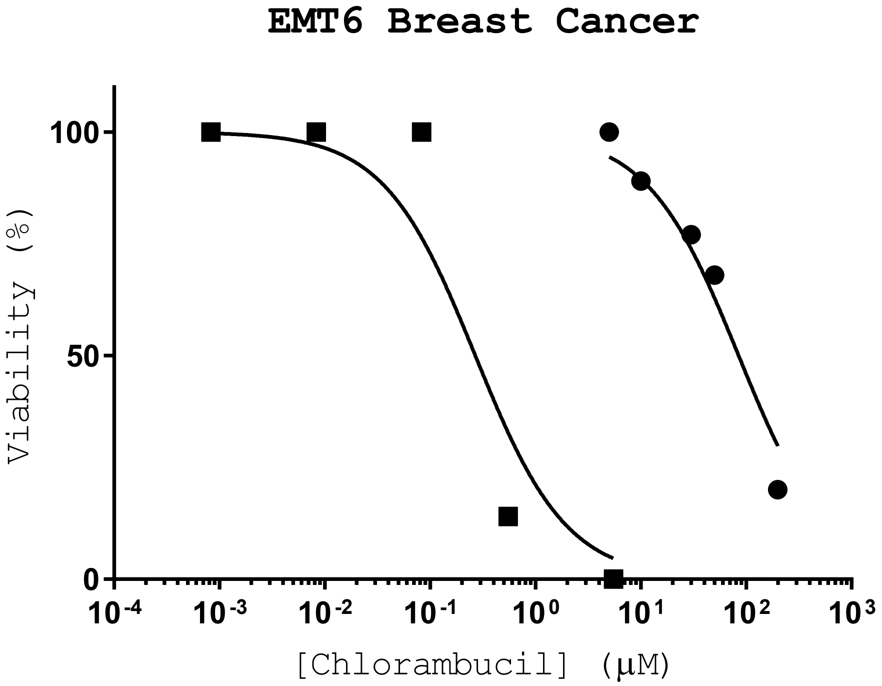

Figure 49: Comparative cytotoxicity of CMB and ANXA5-CMB for EMT breast cancer cells. The viability of EMT6 breast cancer cells treated with either chlorambucil or a chlorambucil-protein conjugate was assayed by alamarBlue assay after 24 hours. Cells were incubated with chlorambucil (CH) or chlorambucil-annexin A5 conjugate (ANXA5-CMB). The conjugate (circles) was significantly more potent than the free chlorambucil (squares) ($p \leq 0.005$). The full viability curve of chlorambucil was truncated by physical limitations (solubility ~300 mM). Data is presented as mean ± SE ($n = 12$). Error bars omitted for clarity if SE was smaller than the point symbol.

The in vitro cytocidal activity of ANXA5-CMB was further characterized in the triple-negative drug resistant 4T1 breast cancer cell line (Figure 50). The viability of 4T1 breast cancer cells treated with either chlorambucil or a chlorambucil-protein conjugate was assayed after 24 hours. Cells were incubated with chlorambucil (CMB) or chlorambucil-annexin A5 conjugate (ANXA5-CMB). The conjugate (circles) was significantly more potent than the free chlorambucil (squares).

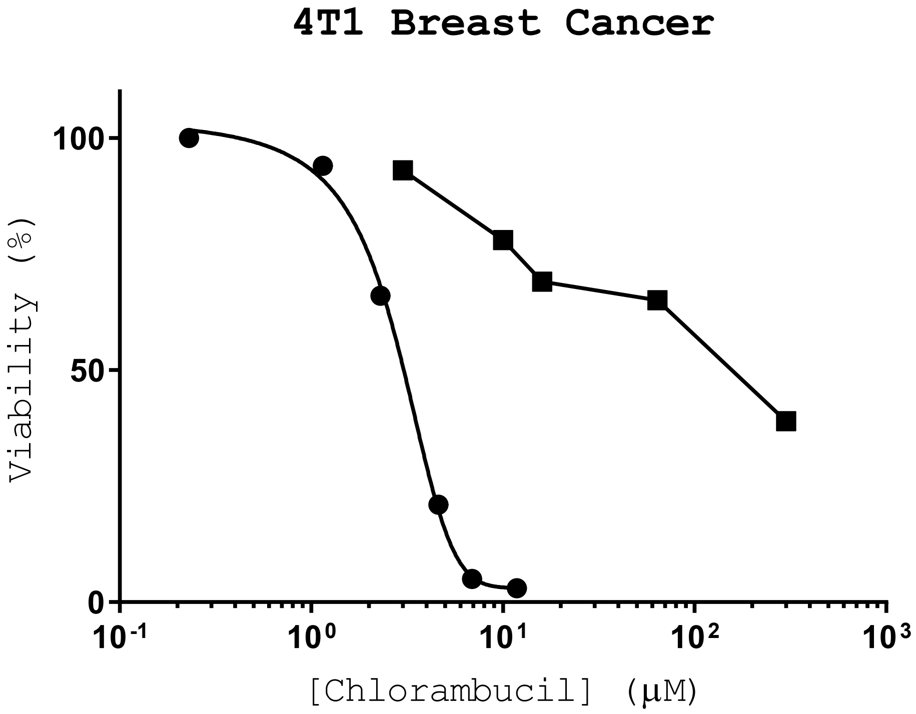

Figure 50: Comparative cytotoxicity of CMB and ANXA5-CMB. The viability of 4T1 breast cancer cells treated with either chlorambucil or a chlorambucil-protein conjugate was assayed by alamarBlue assay after 24 hours. Cells were incubated with chlorambucil (CH) or chlorambucil-annexin A5 conjugate (ANXA5-CMB). The conjugate (circles) was significantly more potent than the free chlorambucil (squares) ($p \leq 0.005$). The full viability curve of chlorambucil was truncated by physical limitations (solubility ~300 mM). Data is presented as mean ± SE (n = 12). Error bars omitted for clarity if SE was smaller than the point symbol.

We observed ANXA5-CMB dependent cytocidal activity in the 4T1 and EMT6 models of breast cancer. In contrast to ANXA5-CMB, we observed very little cytotoxicity in the 4t1 or EMT6 tumor models with CMB alone. In the EMT6 model, CMB dependent cytotoxicity was first observed at concentrations as high as 10 μM. In the drug-resistant tumor line 4T1, CMB dependent cytotoxicity was first observed at doses of 20 μM. The drug CMB alone was only capable of reducing the viability of drug-resistant 4T1 cultures by half at its maximum solubility limit (200 μM). In contrast to CMB alone, the conjugate ANXA5-CMB was much more potent. In the EMT6 cell line cytotoxic effects were first observed at doses as small as 0.1 μM. In the 4T1 cell line cytotoxicity was observed at doses as low as 1 μM.

Evaluation of the therapeutic efficacy of the ANXA4-CMB conjugate was performed in BALB/cj mice bearing orthotopic tumors (Figure 51). The conjugate almost completely halted tumor growth for 18 days. This study was repeated with the addition of a group treated by free CMB (Figure 52). The tumor volumes were significantly smaller by day 9 for the mice treated by the conjugate, compared to treatment by free CMB. The dose of CMB in the ANXA5 conjugate (0.5 mg/kg) is much lower then has been reported in previous studies of treating tumors with free CMB (5-20 mg/kg) [113, 114]. Based on the in vitro data (Figure 50) it appears likely that higher doses of the conjugate would increase the tumor suppressing activity. Even a tripling of the conjugate would give a lower CMB dose then was previously employed.

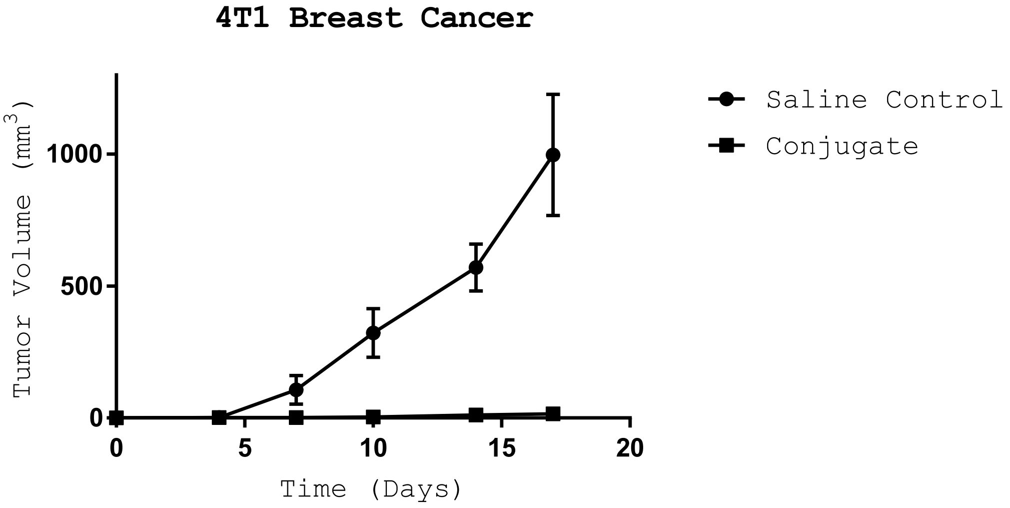

Figure 51: ANXA5-CMB suppression of 4T1 breast cancer tumor growth. The growth of 4T1 metastatic breast cancer was monitored in mice (n = 5) over a period of several weeks. Balb/cj mice of 8 weeks of age were inoculated with an orthotopic injection of 10^5 4T1 cells in the mammary fat pad on day 0. The following day mice received 10 μg of chlorambucil as part of a protein – drug conjugate. The annexin A5 – chlorambucil conjugate was administered daily for the duration of the study. Mouse tumor volumes were recorded twice weekly and tumor volume was determined by the formula [V=1/2*L*W^(2)]. Data is presented as mean ± SE (n = 12).

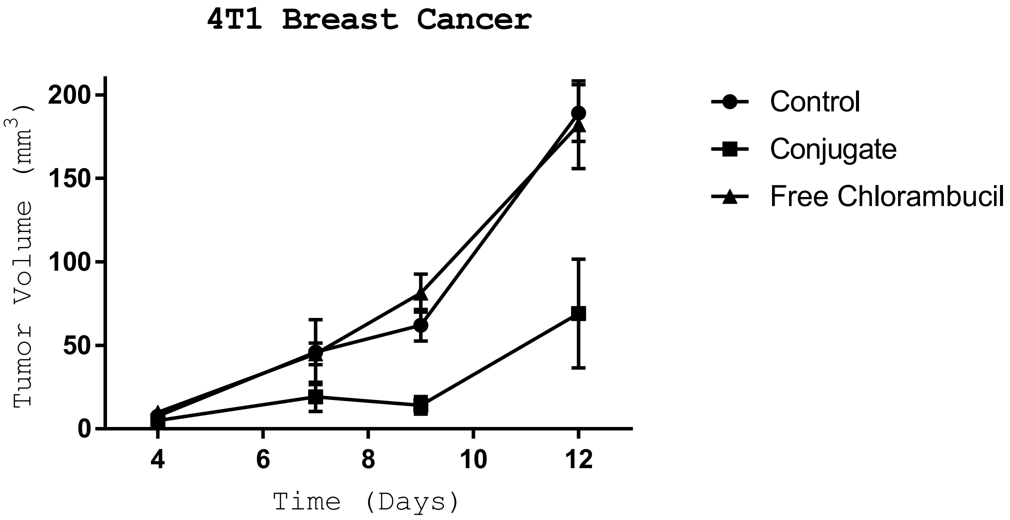

Figure 52: ANXA5-CMB suppression of 4T1 breast cancer tumor growth with the addition of a CMB treatment group. The growth of 4T1 metastatic breast cancer was monitored in mice (n=5) over a period of several weeks. Balb/cj mice of 8 weeks of age were inoculated with an orthotopic injection of 10^5 4T1 cells in the mammary fat pad on day 0. The following day mice received 10 μg of chlorambucil as part of a protein – drug conjugate. The annexin A5 – chlorambucil conjugate was administered daily for the duration of the study. Mouse tumor volumes were recorded twice weekly and tumor volume was determined by the formula [V=1/2*L*W^(2)]. Data is presented as mean ± SE (n = 12).

Conclusion

The novel cytocidal bioconjugate (ANXA5-CMB) comprised of the protein annexin A5 (ANXA5) and the alkylating agent chlorambucil (CMB) possesses significant cytotoxic activity. We characterize the resulting conjugate by both SDS-Page and quantitative fluorescent spectroscopic analysis of CMB. We then successfully demonstrate the activity of the characterized conjugate in four separate models of cancer, two of which we further test in orthotopic murine models. We conclude that the ANXA5-CMB conjugate has significant anticancer activity both in vitro and in vivo.

Chapter 5: Preliminary Studies

Chapter 5A: Heating of Single-Walled Carbon Nanotubes by Very High Frequency Radiowaves

Abstract

Very high frequency (VHF) radio waves (30-150 MHz) heat 6,5 chiral single-walled carbon nanotubes (SWCNT) suspended in 1% Sodium dodecyl sulfate (SDS).

Introduction

Very high frequency (VHF) radiation heats semiconducting SWCNTs by dipole induced phonon generation. Electromagnetic radiation induces the formation of charge dipoles within SWCNTs. These dipoles generate a loading force which mechanically deform the SWCNTS. The deformation of the SWCNT in response to this force can be crudely modeled using either the Euler-Bernoulli or Timoshenko macroscopic beam deformation theorems [115-117]. The transient localized deformation of the carbon lattice within the SWCNT then moves along the carbon nanotube. The moving wave of stressed carbon atoms is referred to as a phonon. The compressional wave travels via acoustic propagation of the phonons along the SWCNT [118]. The phonons then are transferred to the surroundings where they deposit their energy creating heat. The specific heating of SWCNTs in response to VHF radiation has been employed previously in such application as tumor thermal ablation [119].

The VHF radiation dependent heating of SWCNTs by dipole induced phonon generation is primarily a factor of nanotube chirality, nanotube length, and the VHF excitation frequency. While the excitation of SWCNTs by VHF and the resulting heating can be modeled by theorems such as the Euler-Bernoulli beam theory, it is important to note that these models only serve as estimations of SWCNT reactivity (Equation 1).

$$f_{resonant} = \frac{\beta_i^2}{8\pi L^2}\sqrt{\frac{D_o^2 D_i^2 E}{\rho}}$$

Equation 1: Euler-Bernoulli's vibrational beam theory. The resonance frequency ($f_{resonant}$) can be approximated by this model. Where β_1 is a constant, L is the length, D_o and D_i are the inner and outer diameters respectively, E is the Young's modulus, and ρ is the density.

Several factors contribute to the failure of the Euler-Bernoulli equation to accurately model SWCNTs response to VHF radiation. First, the Euler-Bernoulli equation was developed for macroscopic not nanoscopic mechanics. Second, SWCNTs are a heterogeneous mix of many species of nanotube. The SG65i nanotubes employed in this study only contained 39% of the predominant (6,5) chiral SWCNTs (Appendix D: Chiral Analysis). The remaining characterizable mass fraction of the sample was predominantly (7,3), (9,4), (8,4), and (7,5) chiral nanotubes which accounted for another 35% of the total sample. The remaining 26% of the sample consisted of species such as aamorphous carbon, noncharacterizable nanostructures, carbon black, and cobalt-molybdenum catalyst. Each species within the SG65i sample will respond differently to VHF as predicted by the Euler-Bernoulli model. Third, the length of each chiral species of SWCNT is not uniform. Initially, the length of nanotubes within the SG65i samples varied from 0.5-1.0 μM. Sonication of the SWCNTs during the synthesis of the liquid SDS suspension damages the nanotubes, decreasing the mean length of the SWCNTs. Finally, the nanotubes themselves are not pristine beams as assumed by the model. The SWCNTs have numerous point defects where the carbon matrix has been oxidized, breaking the uniformity of the beam decreasing the effective length of the modeled beam. These factors all contribute to deviations in the Euler-Bernoulli model. Therefore, it is necessary empirically observe the SG65i heating response to VHF radiation.

Materials and Methods

Materials

Sodium phosphate, and sodium dodecyl sulfate (SDS) were from Mallinckrodt Chemicals (Phillipsburg, NJ). SG65i single-walled carbon nanotubes were from CHASM Advanced Materials (Canton, MA). Characterization of the SWCNTs can be found in Appendix D.

System Analysis

Electric field plates capable of supporting a 10 mm^2 macro UV-cuvette were scavenged from a Comdel CX-600S ultra stable 13.56 MHz generator chosen for use based off of previous in house work [119]. Plates were placed in a parallel plate orientation using ultra dense polyethylene foam and 10 mm nylon bolts. The setup was then tested using an N5225A Agilent PNA network analyzer (Santa Clara, CA;

Smith chart output) to determine the system's intrinsic resistance and impedance between 30 and 120 MHz (Figure 53).

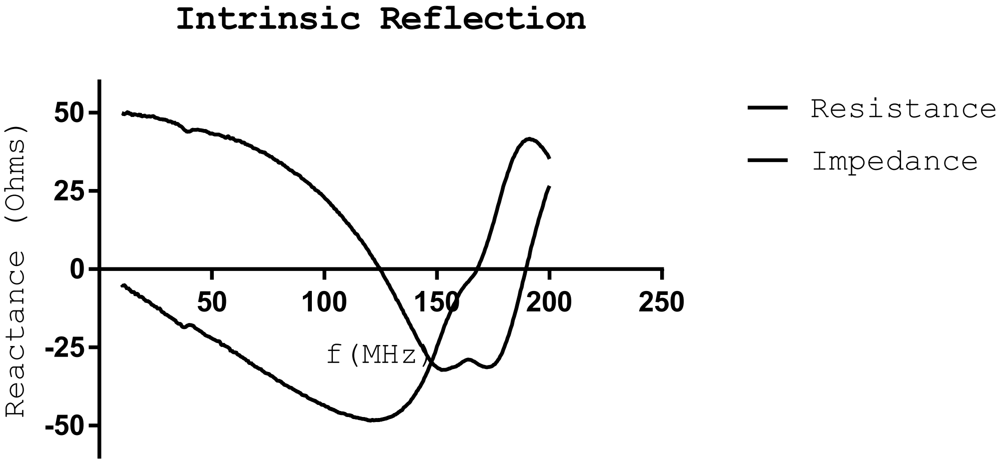

Figure 53: Intrinsic reflection of the load. The intrinsic reflection of the heating plates (load) as measured by the S11 coefficient on a network analyzer assuming a 50 Ω connection.

A narrow band Lumped element matching network (L-network) was chosen to match the plates (Figure 54) [120]. A series capacitor and shunt inductor configuration were chosen for the L-network. Theoretical capacitor and inductor values were then calculated from PNA network analyzer data to impedance match the system (Re(z)=1; z=1) assuming a 50 Ω load (Figure 54) (Figure 55) (Figure 56). Roller inductors (100-1500 nH) and butterfly capacitors (2.0-22.4 pF) were sourced from Rokwell/Collins and obtained through Surplus Sales of Nebraska (Omaha, Nebraska).

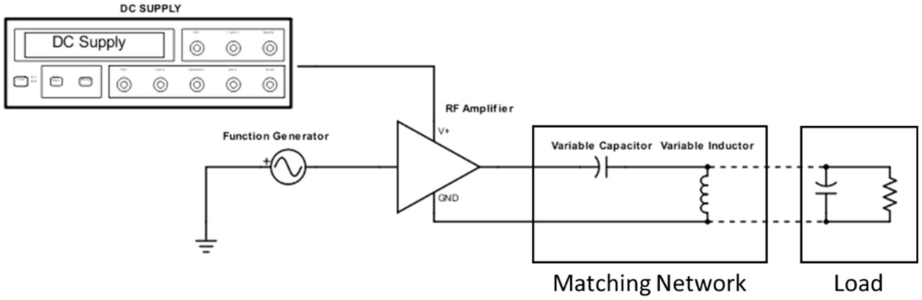

Figure 54: Radiofrequency setup. Electrical diagram of the power supply, signal generator and amplifier used in conjunction with the L-network and heating plates.

$$B = \frac{X_L \pm \sqrt{\frac{R_L}{Z_O}}\sqrt{{R_L}^2 + {X_L}^2 - Z_O * R_L}}{R_L + Z_L}$$

Equation 2: The L-network variable 'B' used as placeholder in several equations is a function of initial system reactance ($\boldsymbol{Z_O}$), frequency (f), load resistance ($\boldsymbol{R_L}$), and load reactance ($\boldsymbol{X_L}$).

$$C = \frac{1}{2 * \pi * f * \left[\left(\frac{1}{B}\right) + \left(\frac{X_L Z_O}{R_L}\right) + \left(\frac{Z_O}{R_L}\right)\right] * Z_O}$$

Equation 3: The deal L-network capacitor value as a function of initial system reactance ($\boldsymbol{Z_O}$), frequency (f), load resistance ($\boldsymbol{R_L}$), load reactance ($\boldsymbol{X_L}$) and the variable B.

$$L = -\frac{Z_O}{2 * \pi * f * B}$$

Equation 4: The ideal L-network inductor value as a function of system reactance ($\boldsymbol{Z_O}$), frequency (f), and the variable B.

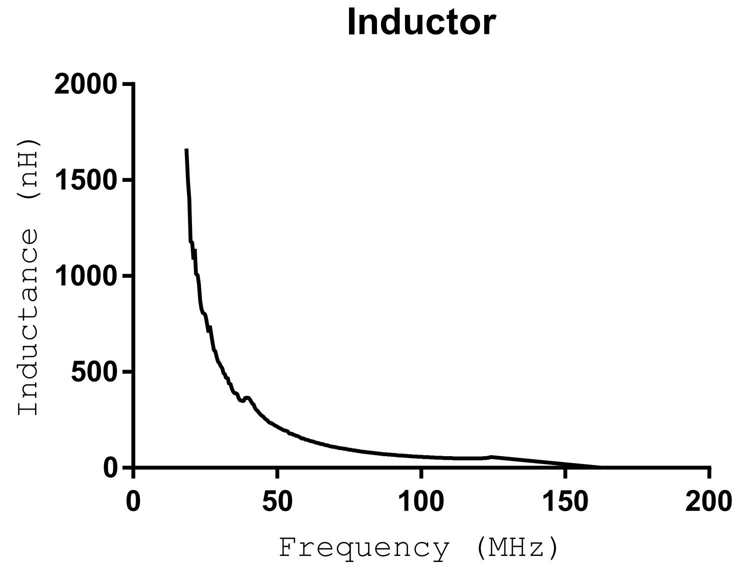

Figure 55: Ideal theoretical inductor values. The ideal inductor values for a L-network that matches the heating plates to the generator were determined from the intrinsic reflextion.

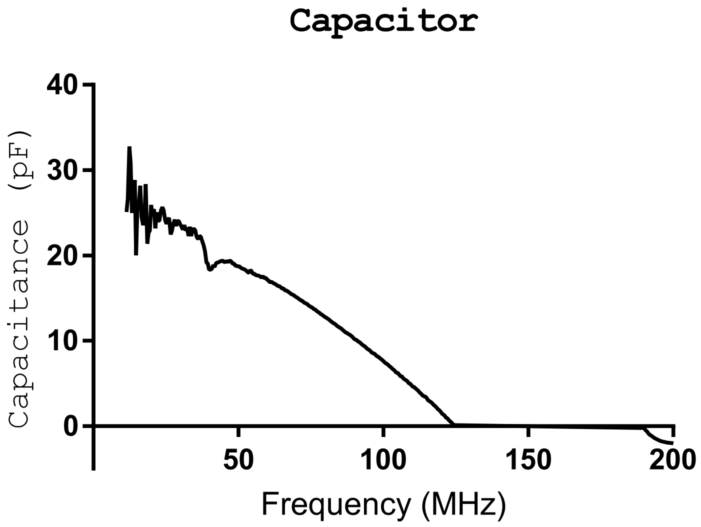

Figure 56: Ideal theoretical capacitor values. The ideal capacitor values for a L-network that matches the heating plates to the generator were determined from the intrinsic reflextion.

Network Matching

The assembled network and plate system was then tested using the PNA network analyzer (transmittance mode) to confirm load match and verify theoretical ideal frequency calculations (Figure 57). The network and plates were then connected to an Agilent 4 -channel oscilloscope via a direction coupler in order to directly monitor voltage mismatch. The coupled system was again tested using the PNA network analyzer to insure the directional coupler and oscilloscope did not shift the ideal transmittance frequency. The plates and network were then attached to the RF system consisting of a BK precision XLN6024 60 V programable power supply (Yorba Linda, Ca), a HD30664 Class A 20 W linear amplifier (Denver, CO), and a HP 8648A signal generator (Las Angeles, CA).

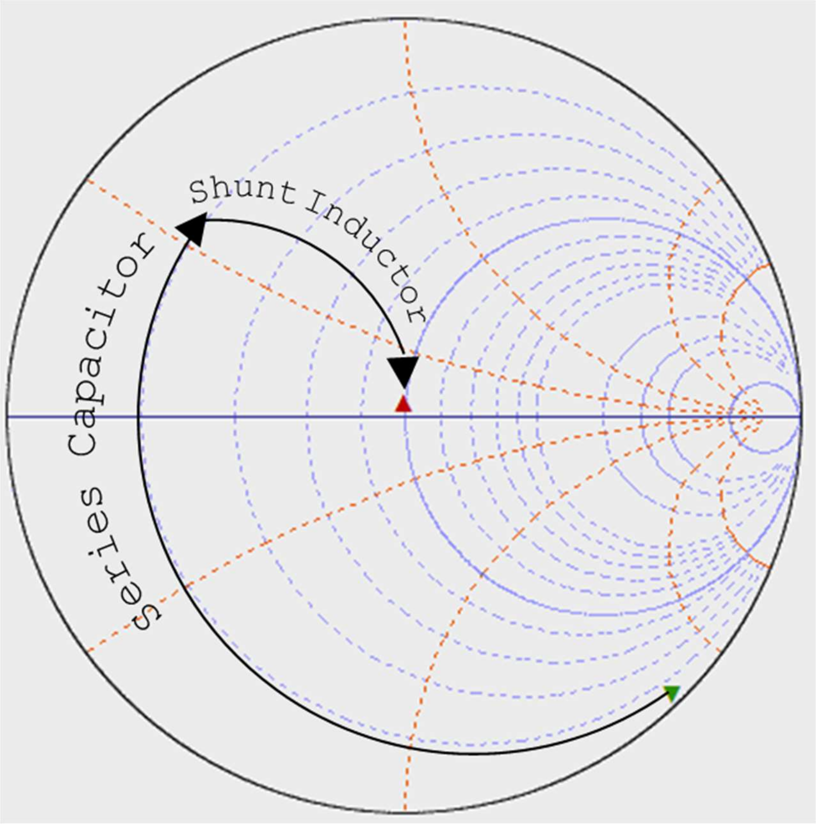

Figure 57: Network matching plates (green arrow) with an attached L-network (red arrow). The field plates initially were unmatched (green arrow). A L-network consisting of a series capacitor and a shunt inductor was constructed and attached to the plates to impedance match the system.

Results and Discussion

A cuvette holding 3 mL of 195 mg/mL SWCNT from was placed between the field plates. The DC power supply was set to 28 V and 4.5 A; current leakage of 3.9 A was observed during operation. The signal generator was keyed to the ideal frequency measured during network matching using the PNA network analyzer, and a -60 dB signal was triggered. The oscilloscope was observed to monitor voltage mismatch while a frequency sweep +/- 20 MHz was performed to empirically optimize voltage mismatch. At this stage voltage mismatches (in: out) of 4:1 were considered ideal. With the proper frequency identified and voltage mismatch minimized, function generator input was increased to -5 to -4 dB over 30 seconds. Samples were then irradiated for 8-10 minutes and temperature was recorded using a thermocouple (Figure 58).

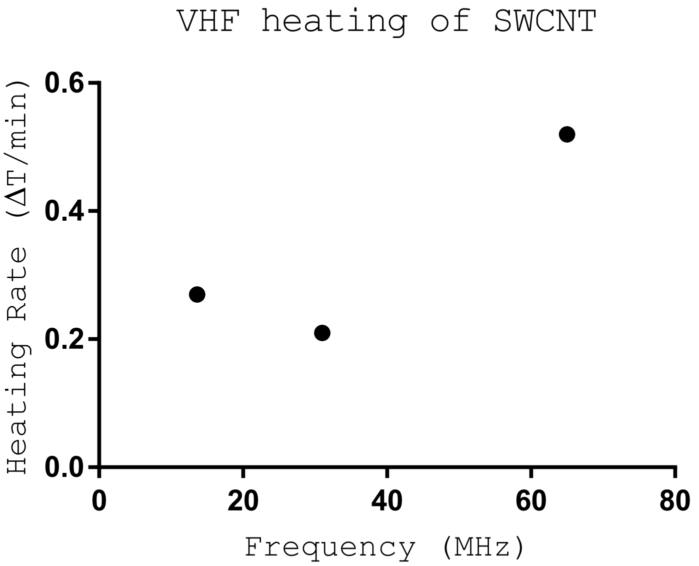

Figure 58: Heating of SWCNTs by VHF radiation. A sample of SWCNTs (195 mg/L) was irradiated at a power of 15 watts for 8-10 minutes and temperature was recorded. Samples excited at 31 and 65 MHz were irradiated using the HD30664 linear amplifier, and the sample at 13.6 MHz was irradiated using a Comdel CX-600S amplifier.

A twofold increase in heating was observed as the frequency increased from 31 MHz to 65 MHz. This change corresponded to a heating rate increase of 0.25 °C/min at a power of 15 W over the measured spectra. Normalizing the heating rate increase to power, we observe a heating rate of 0.016 °C/W.

Conclusions

VHF radiation at a power of 15 W between a frequency of 13 and 65 MHz heated aqueous suspended samples of SG65i SWCNTs in SDS buffer at a maximum rate of 0.52 °C/min. The observed heating rate was less than that observed previously. This difference may be due to experimental protocol differences or deviations from the assumed Euler-Bernoulli model of heating. Further observations at additional frequencies are necessary to more accurately determine the response of SWCNTs to VHF radiation.

Chapter 5B: Synergistic Enhancement of the Cytocidal Activity of Docetaxel by Single-Walled Carbon Nanotubes

Abstract

Here we present a chemotherapeutic delivery agent comprised of 6,5 single-walled carbon nanotubes (SWCNTs) functionalized with the anticancer drug docetaxel (DTX). The chemotherapeutic was synthesized by labeling SWCNTs with the highly hydrophobic taxane, docetaxel, by antisolvent precipitation. Docetaxel loading was then assayed by methylene chloride extraction followed by absorbance spectroscopy. Having determined the loading efficiency of docetaxel, we proceeded to analyze the cytotoxicity of the resulting conjugate in several models of cancer. The SWCNT-DTX conjugate possessed increased anticancer activity compared either SWCNT or DTX alone. In this chapter we demonstrate the synthesis, analysis, and efficacy of SWCNT-DTX conjugate.

Introduction

Carbon nanotubes were first discovered by Sumio Iijima in 1991 and gained extensive attention due to their robust nature, large surface areas, ability to be functionalized, and drug-loading properties [121]. A number of in vitro and in vivo studies have employed carbon nanotubes as chemotherapeutic delivery agents. The unique stability, large surface area and ease of chemical functionalization make carbon nanotubes ideal drug delivery agents capable of efficiently loading a target therapeutic. The association of traditional chemotherapeutics with a carbon nanotube delivery vehicle confers several therapeutic benefits including improved drug solubility, enhanced stability, increased drug cytotoxicity, and increased tumor uptake. While a diverse group of tumor killing agents including novel therapeutics such as folate receptor inhibitors, interfering RNA, and cell toxins have been used in association with nanotube delivery, the vast majority of nanotube associated chemotherapeutic agents belong to the taxane, platinum or anthracycline family.

Carbon nanotubes been used as delivery agents for chemotherapeutics of the anthracycline family. Originally isolated from cultures of Streptomyces peucetius in the early 1960s by multiple independent groups, daunorubicin, the founding member of the glycoside anthracycline family was effective against a wide variety of cancer types, most notably childhood leukemia [122, 123]. While nanotube associated daunorubicin has been employed by several groups, the majority of anthracycline-nanotube research has focused on the more potent anthracycline derivative doxorubicin [124-129]. Another common group of agents whose therapeutic potential can be enhanced by nanotubes is the platinum agent family. Discovered in 1965, this family of DNA intercalating agents, including the founding member cisplatin are potent cytostatic agents effective in a wide variety of tumor types especially when employed with SWCNTs [130-133].

Since their first documented in vitro use in 1971, the taxane family of cytostatic agents has become the standard of care for many types of cancer [134]. The taxane family of cytostatic agents including the founding member of the family, paclitaxel, and derivatives such as docetaxel are some of the most effective anticancer chemotherapeutics in the clinical environment. [135]. However, despite their tremendous clinical significance, the clinical use of taxanes is hampered by three critical drawbacks. First, members of the taxane family are almost completely insoluble in water, necessitating the use of solubilizing agents such as polysorbate or castor oil derivatives to facilitate intravenous administration. Second, while these solubilizing excipients enable the aqueous administration of taxanes, they have significant effects on the bioavailability of administered taxanes [136]. Finally, only a fraction of a given taxane dose actually reaches neoplastic tissue. Harnessing the unique chemical and physical properties of carbon nanotubes as delivery agents, researchers have been able to overcome these therapeutic challenges [137-139].

Materials and Methods

Materials

Bovine serum albumin (BSA), Alamar Blue reagent, Triton X-100, EDTA, TPCK, β-mercaptoethanol, PMSF, and Tris-acetate-EDTA buffer were from Sigma-Aldrich (St Louis, MO). Sodium phosphate and sodium dodecyl sulfate (SDS) were from Mallinckrodt Chemicals (Phillipsburg, NJ). Docetaxel was from TCI America. HPLC grade ethanol was from Acros Organics (Waltham, MA). Antifade reagent Fluoro-gel, and Slide-A-Lyzer dialysis cassettes (3.5 kDa) were from Thermo Fisher Scientific (Waltham, MA). The 2 and 100 kDa dialysis membranes were from Spectrum Laboratories (Rancho Dominguez, CA). Roswell Park Memorial Institute cell medium (RPMI-1640) and Hank's balanced salt solution were from ATCC (Manassas, VA). Fetal bovine serum (FBS) was from Atlanta Biologicals (Lawrenceville, GA). Trypton, yeast extract, and kanamycin monosulfate were obtained from Alfa Aesar (Haverhill, MA). Sodium hydroxide, potassium chloride, and sodium chloride were from VWR inc (Radnor, PA). HRV-C3 protease was from Sino biologics (Portland, OR). Single-walled carbon nanotubes (SWCNT) were obtained from CHASM (Boston, MA).

Cell lines and Cell Culture

Cell lines and cell culture were done as previously described in chapter 2 and Chapter 4.

Cell Viability Analysis

Cells were incubated with chemotherapeutic as described and then cell viability was assayed by alamarBlue assay. Cells were incubated with fresh media containing 10% (v/v) alamarblue for 3 hours and then fluorescence was assayed at 570:580; ex; em). Viability of treated samples was compared to an untreated control. A more detailed procedure was previously described [46].

Conjugate Synthesis

The SWCNT-DTX conjugate was synthesized by antisolvent precipitation of DTX. A mixture of 5 mg of SWCNT and 20 mg DTX in 500 μL of anhydrous EtOH was mixed in an JP-890 ultrasonic bath for 15 m while dropwise phosphate-buffered saline solution was added to a total volume of 3 mL. The mixture was then pulsed 10 times by a Fischer 50-sonic dismembrator at 400 W for 10 s each time. The SWCNT-DTX conjugate was isolated by centrifugation at 10,000 g for 15 minutes. The pellet was then briefly washed with anhydrous EtOH followed by nanopore water to remove excess DTX.

Chemical Analysis

Analysis of the SWCNT-DTX conjugate was done by absorbance spectroscopy. SWCNT concentration was determined as previously described (Chapter 3). DTX was isolated from the SWCNT-DTX conjugate by methylene chloride - water solvent biphasic extraction. The DTX within the methylene chloride was then quantified by absorbance spectroscopy of the maximum absorbance between 200-300 nm. The detailed spectroscopic examination of DTX in methylene chloride and various other solvents can be found in (Appendix E).

In Vitro Cytotoxicity Studies

The SWCNT-DTX conjugate was gently suspended in EtOH by gently vortexing. Viability assays were performed using the AlamarBlue assay as described in “Chapter 2”.

Results and Discussion

Initial Observations

The synergistic interaction between DTX and SWCNTs was first observed in vitro in the B16F10 model of melanoma (Figure 59). Cells were accidentally cultured in docetaxel (10 μM) supplemented media with or without SWCNTs (5 mg/L). In groups receiving SWCNTs and DTX, a marked increase in cell cytotoxicity was observed. We hypothesized that SWCNTs were synergistically enhancing DTX cytotoxicity.

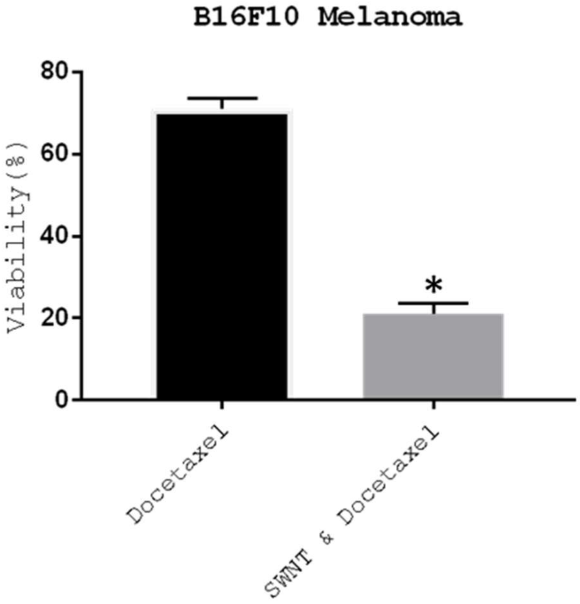

Figure 59: Nanoparticle-Drug synergistic cytotoxicity. The presence of EtOH dispersed SWCNT (5 mg/L) synergistically enhances DTX (10 µM) cytotoxicity. B16F10 melanoma was cultured with DTX and SWCNT for 24 h. The combination of DTX and SWCNT was significantly more toxic that DTX alone, as indicated by ‘ * ‘ ($P \leq 0.05$). Data is shown as the mean ± SE (n = 3).

In a more detailed study, neither docetaxel or SWCNT significantly reduced the viability of B16F10 cell cultures over 24 hours (Figure 60). However, the combination of SWCNT and DTX in solution significantly decreased cell cytotoxicity ($P \leq 0.05$). We conclude that SWCNT synergistically enhance DTX-mediated B16F10 cytotoxicity.

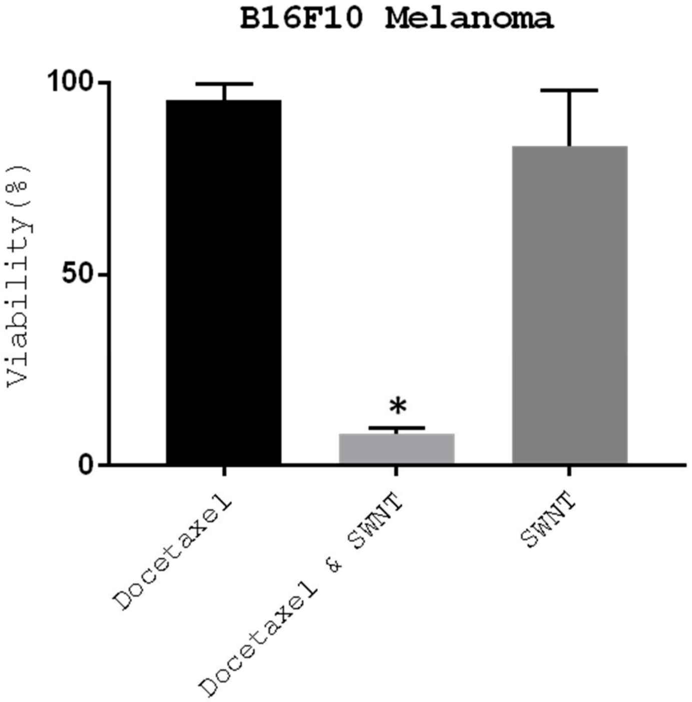

Figure 60: Nanoparticle-Drug synergistic cytotoxicity. The presence of aqueous dispersed SWCNT (5 mg/L) synergistically enhances DTX (10 µM) cytotoxicity. B16F10 melanoma was cultured with DTX and SWCNT for 24 h. The combination of DTX and SWCNT was significantly more toxic that DTX or SWCNTs alone as indicated by ‘ *’ ($P \leq 0.05$). Data is shown as the mean ± SE ($n = 3$).

Conclusion

Single-walled carbon nanotubes synergistically enhance the toxicity of DTX in the B16F10 model of melanoma. We first observed in the B16F10 cell line that the independent presence of both DTX and SWCNTs in solution produces a marked increase in the cytotoxicity of both components. In an attempt to harness this observed phenomenon, a SWCNT-DTX conjugate was synthesized by antisolvent precipitation. We characterized the DTX loading by absorbance spectroscopy following methylene chloride extraction. Preliminary in vitro data in the MB49 cell line suggests that the SWCNT-DTX conjugate is more toxic than free DTX. While we observed marked anticancer activity in the MB49 cell line, further work is necessary to characterize the synthesis and in vitro anticancer activity of the DTX-SWCNT conjugate.

Chapter 5C: Interaction of Annexin A5 and Drug Resistance in the Presence of the Selecting Drug

Abstract

Phosphatidylserine (Ptd-L-Ser) dependent annexin A5 (ANXA5) binding to wildtype L1210 and drug resistant L1210r leukemia cells is modulated by the presence of subtoxic doses (10 μM) of chlorambucil (CMB). Drug resistance was induced in the L1210 cell line by culture with CMB (10 μM) for 2 months; creating a drug resistance subline, L1210r. The expression of Ptd-L-Ser was assayed in both L1210 and L1210r cells by cytometric quantification of fluorescent FITC-ANXA5 binding. While we observe increases in Ptd-L-Ser expression in the L1210r versus L1210 cell lines, this relationship was inverted in the presence of chlorambucil (10 μM) .

Introduction

Many tumor cell lines are characterized by increased Ptd-L-Ser expression [140-142]. The expression of Ptd-L-Ser is intrinsically tied to the pathological progression of cancer. All lethal tumors share several etiological hallmarks including: uncontrolled proliferation, failure of apoptosis, angiogenic activity, evasion of the immune system, and metastasis. [12, 13, 17-20, 31]. The expression of Ptd-L-Ser is intrinsically tied to oncogenesis and metastasis. Furthermore, the expression of Ptd-L-Ser is a byproduct of drug resistance.

One of the principle mechanisms of acquired drug resistance in tumors is drug efflux by cell membrane transporters. The transporters, primarily of the ATP-binding cassette (ABC) transporter family, remove chemotherapeutics from the cell [143-148]. Increased expression and activity of ABC-transporters confers drug resistance to cancerous cells. The natural role of these transporters is the transport of hydrophobic molecules across the lipid bilayer of the cellular membrane. Specifically, many ABC-transporters act as flippase, floppase and scramblases maintaining Ptd-L-Ser asymmetry in healthy cells [149-152]. We hypothesize an increase in Ptd-L-Ser would be observed during the acquisition of ABC-transport dependent drug resistance.

Results

Constitutive Expression of Ptd-L-Ser

The constitutive expression ot Ptd-L-Ser on cancer cells can be observed by flow cytometric analysis using the natural ligand of Ptd-L-Ser, ANXA5. Cancerous L1210 cells express more Ptd-L-Ser than healthy rat mesenchymal stem cells (rMSCs) as observed by ANXA5 binding (Figure 61).

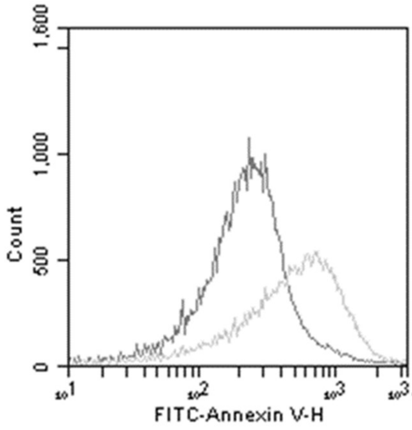

Figure 61: Ptd-L-Ser expression in rMSCs (left) and wildtype L1210 leukemia cells (right).

Drug Resistance

Wildtype L1210 leukemia cells were transformed by continuous exposure to subtoxic doses of chlorambucil (10 μM) for 2 months. This selection produced a new drug resistant L1210r cell line. We observe that the constitutive expression of low concentrations of Ptd-L-Ser on wildtype L1210 leukemia cells is heightened by chlorambucil resistance in L110r cells (Figure 62).

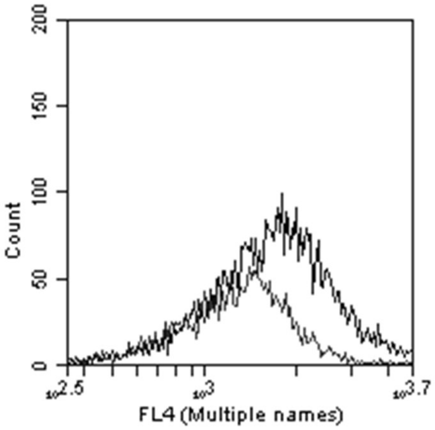

Figure 62: Drug resistant L1210r cells (right) express more Ptd-L-Ser than wildtype L1210 cells (left).

Drug-Drug Resistance Interaction

We assessed the interactions between CMB and CMB resistance on the expression of Ptd-L-Ser in L1210 leukemia. Ptd-L-Ser dependent ANXA5 binding was assessed in both wildtype and resistant L1210 leukemia cells in the presence of drug supplemented or drug free media (Figure 63). We observed that wildtype L1210 cells significantly upregulate Ptd-L-Ser expression in subtoxic doses of CMB (top left). Interestingly, we observed the same relationship in drug resistant cells as well (top-right). Furthermore, we observed that drug resistant cells continuatively express more Ptd-L-Ser than wildtype cells in drug free media (bottom left). Surprisingly, this relationship was revered in presence of chlorambucil (bottom right). It is likely that this relationship results from the competition between hydrophobic chlorambucil and Ptd-L-Ser for ABC-transporter floppase/scramblase activity in L1210r cells [144, 153, 154].

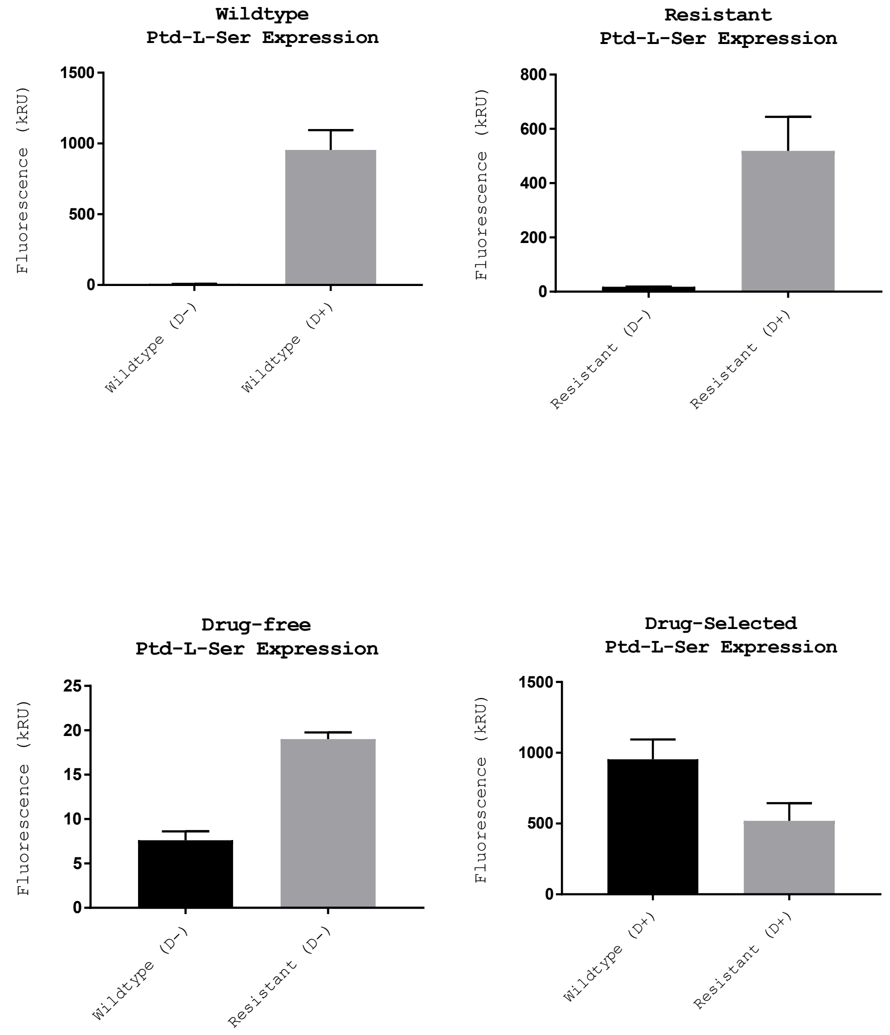

Figure 63: <u>Effects of CMB and CMB resistance on Ptd-L-Ser expression in L1210 leukemia.</u> The relative expression of Ptd-L-Ser as measured by fluorescent ANXA5 accumulation was assayed in wildtype and drug resistant L1210 cells in the presence of media with or without supplemental drug (D+, D-) All represented groups were significantly different ($P \leq 0.05$). Data is shown as the mean ± SE (n = 3).

Conclusion

Phosphatidylserine (Ptd-L-Ser) dependent Annexin A5 (ANXA5) binding to wildtype L1210 and drug resistant L1210r leukemia cells is modulated by the presence of subtoxic doses (10 μM) of chlorambucil (CMB). Drug resistance was induced in the L1210 cell line by culture with CMB (10 μM) for 2 months, creating a drug resistance subline, L1210r. The expression of Ptd-L-Ser was assayed in both L1210 and L1210r cells by cytometric quantification of fluorescent FITC-ANXA5 binding. The constitutive expression of Ptd-L-Ser on wildtype L1210 was heightened in chlorambucil resistant L1210r. Interestingly, this relationship was inverted in the presence of chlorambucil. Further work is necessary to establish ABC-transporter activity and expression in relation to drug resistance.

Chapter 5D: Bactericidal Activity of a Novel Protein-Antibiotic Bioconjugate

Abstract

Here we present antibacterial activity of a novel annexin A5 (ANXA5) derivative. The ANXA5 derivative is a novel bioconjugate comprised of the protein annexin A5 (ANXA5) and the penicillin derivative ampicillin (AMP). The extracellular antibacterial activity of the annexin A5 – ampicillin (ANXA5-AMP) conjugate was assayed in E. coli and NTHI bacteria. Surprisingly, the antibiotic conjugate, ANXA5-AMP also possessed significant antitumor activity as assayed in the EMT6 murine model of metastatic breast cancer.

Introduction

Bacterial infections can be classified as either intracellular or extracellular, depending on the location of the pathogen. Notable intracellular bacterial pathogens include Legionnaires disease, tuberculosis, and the plague. Treatment of these diseases is challenging due to the location of the bacteria within the cell. The mammalian cell membrane serves as an additional protective barrier for the pathogenic bacteria, blocking antibiotics. One possible mechanism to enhance the delivery of an antibiotic to infected cells is by conjugation of the antibiotic to a targeting moiety. Interestingly, many cells infected with intracellular bacteria express phosphatidylserine [31]. The expression of Ptd-L-Ser on infected cells may be a target for targeted antibiotic delivery.

Materials and Methods

Annexin A5 Production

Recombinant mCGL-ANXA5 was produced and isolated by His-tag chromatography, and activity was confirmed by a chromatographic assay as previously described (Chapter 1). The experimental procedure is provided in Appendix A. Purity was confirmed by SDS-PAGE. Samples were confirmed endotoxin free by limulus amoebocyte lysate assay.

Conjugate Synthesis

Synthesis of the conjugate was performed in a process similar to that previously described (Chapter 4). However, several key differences in reaction chemistry were necessitated by the presence of both a primary amine and a carboxylic group within AMP. First, AMP (30 mg/mL) was activated by EDC (3 mg/mL). This was to account for the loss of AMP by AMP-AMP crosslinking. All other steps remained as previously described (Chapter 4).

Analysis of Conjugate

The concentration of ampicillin (α-aminobenzylpenicillin) within the ANXA5-AMP conjugate can be determined by fluorescent spectroscopy [155]. Standards of penicillin in phosphate buffer supplemented with 1% formaldehyde were acidified with HCl acid (pH 2) and then incubated at 98 °C for 1 hour to catalyze the production of α-aminobenzylpenicillenic acid. This derivative of ampicillin is fluorescent (ideal; 346/422 ex/em). Samples were then neutralized with NaOH (pH 7.4). Fluorescent analysis (360/460 ex/em) was capable of detecting small concentrations of ampicillin (7 μg/mL) (Figure 64).

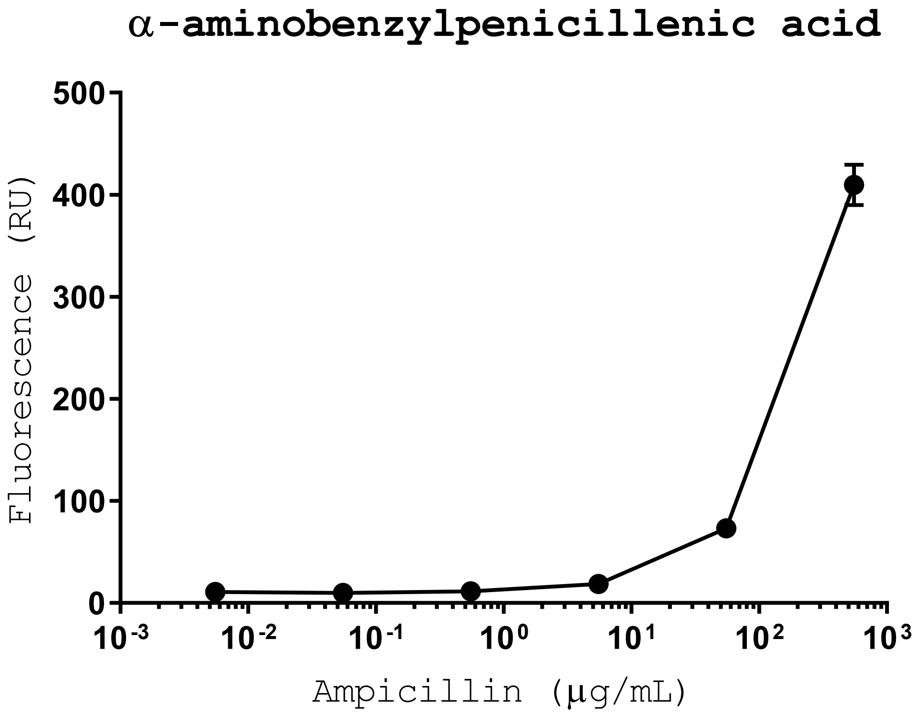

Figure 64: Fluorescent standard of ampicillin derivative α-aminobenzylpenicillenic acid. The concentration of ampicillin (α-aminobenzylpenicillin) can be determined by fluorescent spectroscopy. Standards of penicillin were acidified with HCl acid (pH 2) and then incubated at 98 °C for 1 hour to catalyze the production of α-aminobenzylpenicillenic acid. This derivative of ampicillin is fluorescent (ideal; 346/422 ex/em). Samples were then neutralized (pH 7.4). Fluorescent analysis of standards (measured; 360/460 ex/em) was capable of detecting small concentrations of ampicillin (7 μg/mL). Data is shown as mean ± SE (n = 3).

Cell Lines and Cell Culture

EMT6 breast cancer cells from ATCC (Manassas, VA) were cultured in Waymouth's MB 752/1 medium with 2 mM L-glutamine supplemented with 15% fetal bovine serum (FBS). All cells were grown at 37 ° C and 100% humidity under

5 % CO2. All cells were passaged using 0.25 % (w/v) Trypsin in 0.53 mM EDTA. E. coli strain BL21(DE3) from Thermo Fisher Scientific (Waltham, MA) were cultured in LB broth at 37 ° C. Non-typable Haemophilus influenzae (NHTi) from BEI: NRAID (Manassas, VA) was cultured on chocolate agar or in brain-heart infusion broth at 37 ° C. NTHi cultures were supplemented with factors V and X [156].

Results and Discussion

Extracellular Bactericidal Assay

The antibacterial activity of ANXA5-AMP was first assayed in E. coli. E. coli (strain:BL21(DE3)) was cultured in antibiotic free LB medium as previously described [6]. Cultures were supplemented with AMP or ANXA5-AMP and growth was monitored for 24 h (Figure 65). The ANXA5-AMP conjugate significantly reduced E. Coli growth compared to free AMP. In addition to work with AMP derivatives of ANXA5, we observed that other therapeutic ANXA5 derivatives such as ANXA5-mCGL possessed antibacterial activity against both intracellular and extracellular bacteria (Appendix: Antibacterial Assay). This is interesting because the E. coli membrane contains little Ptd-L-Ser [157, 158] . Further work is necessary to identify the Ptd-L-Ser independent mechanisms resulting in significantly heightened ANXA5-dependent antibacterial activity in this model.

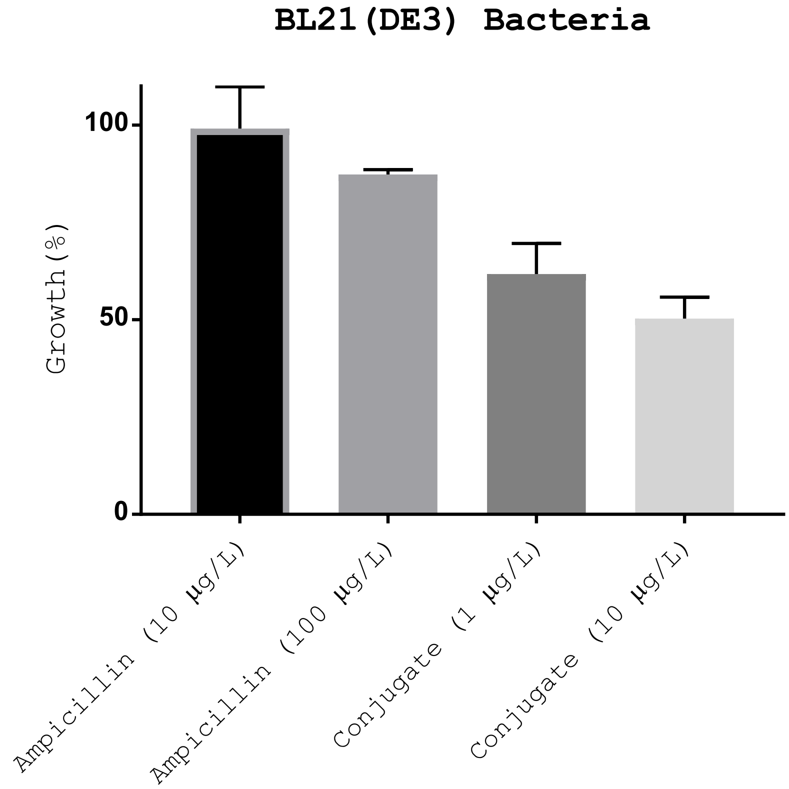

Figure 65: Antibacterial activity of ampicillin and ampicillin-annexin A5 conjugate. The ANXA5-AMP conjugate significantly reduced E. coli growth compared to free AMP ($P \leq 0.05$). Data is represented as mean ± SE ($n = 5$).

In a more in depth assay, the antibacterial activity of the ANXA5-AMP conjugate was assessed in the NTHi model of infection. The viability NTHi was determined by serial dilution and plate culture (Figure 66). Samples treated with either AMP or ANXA5-AMP conjugate were incubated for 36 h. Following incubation colonies were enumerated and compared to untreated controls. The antibacterial activity of the conjugate was more then 10-fold more potent than that of free ampicillin.

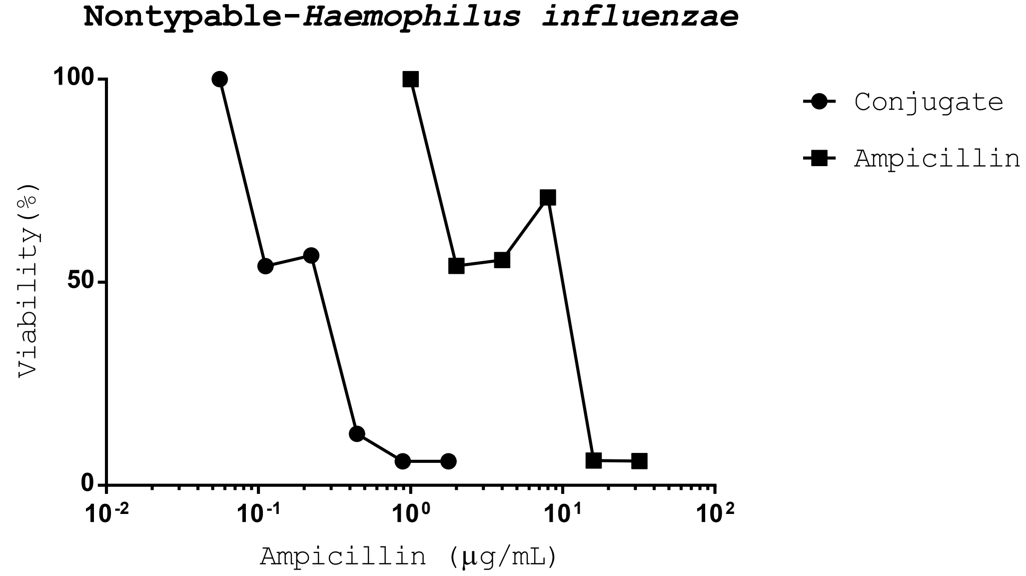

Figure 66: Comparative bactericidal activity of ampicillin and conjugate. The viability nontypable-Haemophilus influenza was determined by serial dilution and plate culture. Samples treated with either ampicillin (AMP, squares) or protein-antibiotic conjugate (AMP-ANXA5, circles) were incubate for 36 hours with antibiotic or conjugate. Following incubation colonies were enumerated and compared to untreated controls. The antibacterial activity of the conjugate was 10 to 10-fold more potent than that of free ampicillin. Data presented as mean ± SE (n = 8). Error bars omitted for clarity if SE was smaller than the point symbol.

Anticancer Activity

In addition to significant antibacterial activity the ANXA5-AMP conjugate possessed significant anticancer activity. EMT6 viability was monitored following a brief incubation (24 hours) with the ANXA5-AMP conjugate (Figure 67). Surprisingly, the conjugate has significant cytocidal activity in the EMT6 model (CC50: 100 µg/mL). Unlike most antibiotic derived chemotherapeutics, ampicillin is remarkably nontoxic. A lethal dose of ampicillin is 0.5% of an individuals bodyweight or about 310 g for an average 62 kg person [159]. No reduction in EMT6 viability was observed in doses of AMP as high as 0.52 mg/mL.

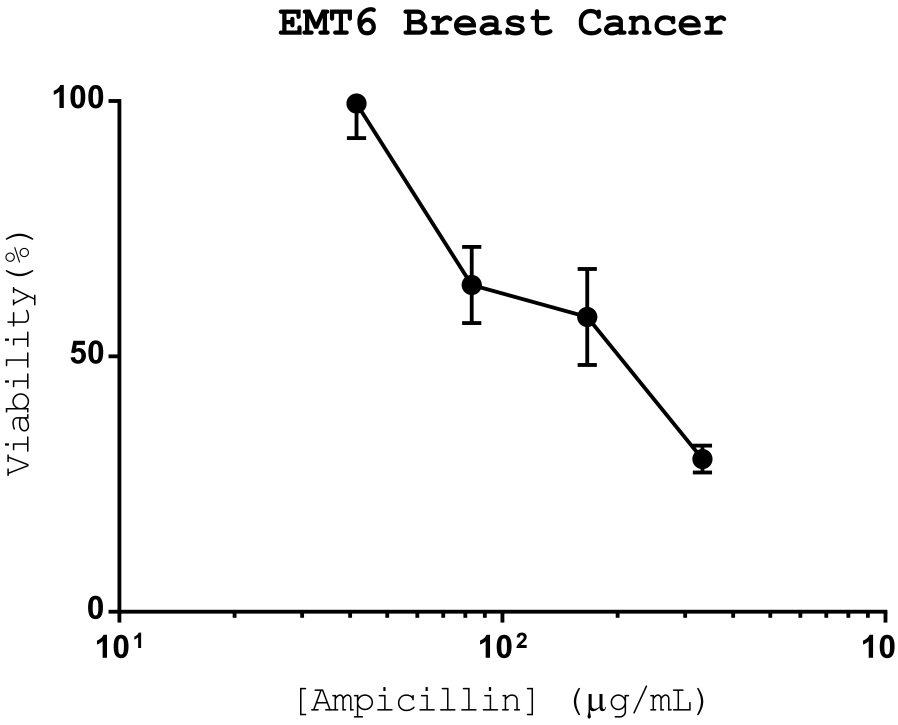

Figure 67: Toxicity of the conjugate in an EMT6 breast cancer model. The annexin V - ampicillin protein conjugate (AMP-ANXA5) possesses anticancer properties. The viability of EMT6 breast cancer cells was monitored following a brief incubation (24 hours) with the conjugate. The conjugate was capable of not only retarding cell growth but killing tumor cells as well. Data is presented as mean ± SE (n = 8).

Conclusion

The bioconjugate annexin A5 has significant activity against both intracellular and extracellular bacteria. In extracellular E. coli, the bioconjugate suppressed cell growth more efficiently than free AMP, even at doses 100-fold lower. In the intracellular model of pathogenic bacterial infection with NHTi, the ANXA5-AMP conjugate was more then 10-fold more potent than free AMP . Surprisingly, the antibiotic conjugate, ANXA5-AMP also possessed significant antitumor activity in the EMT6 murine model of metastatic breast cancer. Further work is needed to develop this novel bioconjugate in additional tumor models, and different models of pathogenic infection.

Chapter 4E: Antineoplastic Carboplatin-ANXA5 Derivative

Abstract

Here we present a novel cytostatic bioconjugate (ANXA5-CBDCA) comprised of the protein annexin A5 (ANXA5) and the drug carboplatin (CBDCA). CBDCA was covalently linked to ANXA5 with a 1-ethyl-3-(3-dimethylaminopropyl) carbodiimide (EDC) intermediate linker stabilized by N-hydroxysuccinimide (NHS). Here we present the characterization and antitumor activity of the novel ANXA5-CBDCA conjugate. The conjugate was characterized by absorbance spectroscopy, and we confirmed the conjugation of carboplatin to the protein. The cytocidal activity of the ANXA5-CBDCA bioconjugate was probed in vitro using the metastatic 4T1 breast and p53$^{-/-}$ ID8 ovarian cancer cell lines where we observed increased cytotoxicity compared to carboplatin alone. In vivo antineoplastic activity was determined in the 4T1 mouse model of late stage metastatic triple-negative drug-resistant breast cancer, where we observed large decreases in tumor volume.

Introduction

Carboplatin was linked to ANXA5 using 1-Ethyl-3-(3-dimethylaminopropyl) carbodiimide (EDC) and N-hydroxysuccinimide (NHS). Carboplatin is of prime clinical significance due to its remarkably broad anticancer activity in multiple forms of cancer. Previous work (Chapter 4), demonstrated the activity of a ANXA5 – chlorambucil conjugate. However, chlorambucil is very well tolerated, and relatively nontoxic. Carboplatin on the other hand, has significantly higher anticancer activity, at the cost of increased toxicity. This increased activity was the driving force behind the decision to select carboplatin as a potential ANXA5 - drug conjugate. While numerous groups have examined the activity of protein-carboplatin conjugate, no one to date has examined derivatives of carboplatin and annexin.

Materials and Methods

Materials

Materials were sourced as previously described in chapters 1, 2 and 3.

Cell Culture

Drug resistant, triple-negative 4T1 breast cancer cells were transfected with tdTomato (Td) as previously described [6]. 4T1-Td breast cancer cells were cultured in Roswell Park Memorial Institute (RPMI-1640) medium supplemented with 10 % FBS and 1% penicillin/streptomycin antibiotics (100 U mL^{-1} and 100 $\mu g/mL^{-1}$ respectively). P53 double negative ID8 ovarian cancer cells were cultured in DMEM media supplemented with 10% fetal bovine serum(FBS), insulin-transferrin-selenius acid, and 1% penicillin/streptomycin antibiotics (100 U mL^{-1}

and 100 μg/mL^{-1} respectively). Cells were passaged using 0.25 % (w/v) trypsin in 0.53 mM EDTA. Cells were grown at 37 ° C and 100% humidity under 5 % CO_2 supplemented atmosphere.

Synthesis of Conjugate

Synthesis of the conjugate was performed in a process similar to that previously described (Chapter4). However, several key differences in reaction chemistry were necessitated by the absence of a carboxylic group on CBDCA. Instead of activating the carboxylic group of a drug, the carboxylic group on ANXA5 (2 mg/mL) was activated with EDC (0.12 mg/mL) and NHS (0.12 mg/mL). The activation of ANXA5 carboxylic groups was done in in the presence of CBDCA (CBDCA 20 mg/mL).

Analysis of Conjugate

The concentration of CBDCA within the ANXA5-CBDCA can be determined by quantitative absorption spectroscopy [160]. Standards of CBDCA ($[\text{Carboplatin}]_{\text{starting}}$: 4.5 mg/mL) were solubilized in 30 mM sodium phosphate buffer and max absorbance was quantified.

Results and Discussion

Loading Efficiency

Typical molar loading ratios of CBDCA to ANXA5 of 3:1 (CBDCA: ANXA5) were observed. Due to the precipitation of multiple crosslinked byproducts, EDC/NHS synthesis was inefficient, generating significant precipitates with typical ANXA5 yields as low as 4.7%.

In Vitro Cytotoxicity

Conjugate cytotoxicity was determined by AlamarBlue assay as previously described (Chapter 2: Cytostatic Protein-Drug Conjugate).

Results and Discussion

Spectroscopy

The extent of CBDCA functionalization within the ANXA5-CBDCA conjugate was determined by comparative absorption spectroscopy. Controlling for the absorbance of protein, we observed the unique UV-absorbance spectrum of carboplatin within samples of ANXA5-CBDCA. The concentration of ANXA5 was determined by Bradford assay as previously described (Chapter 2: Cytostatic Protein-Drug Conjugate). The extent of CBDCA ANXA5 functionalization was highly sensitive to reaction conditions but typical molar ratios of 3:1 (CBDCA: ANXA5) were observed.

.

Anticancer Activity

The cytocidal activity of ANXA5-CBDCA was first assessed in vitro in the 4T1 metastatic breast cancer model. The viability of 4T1 breast cancer treated with either CBDCA or ANXA5-CBDCA conjugate was assayed after 24 hours (Figure 68). The ANXA5-CBDCA conjugate was significantly more toxic than free carboplatin, killing virtually all cells at doses exceeding 100-fold less than free CBDCA.

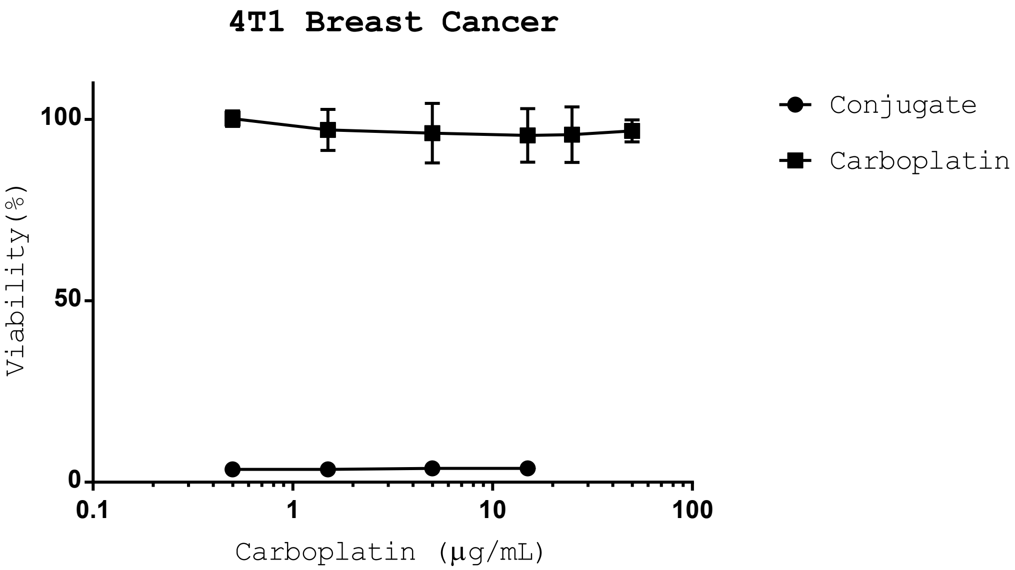

Figure 68: Comparative cytotoxicity of carboplatin and conjugate. The viability of 4T1 breast cancer cells treated with either carboplatin (squares) or carboplatin-protein conjugate (circles) was assayed after 24 hours. The annexin A5 – carboplatin conjugate was more toxic than free carboplatin, killing virtually all cells at doses exceeding 100-fold less than free carboplatin. Data is shown as the mean ± SE (n = 8)

In a second in vitro model, the cytocidal activity of ANXA5-CBDCA was assayed in the ID8 p53$^{-/-}$ mouse model of ovarian metastatic cancer (Figure 69). In this second model, the carboplatin protein conjugate was significantly more toxic to cancer cells than free carboplatin.

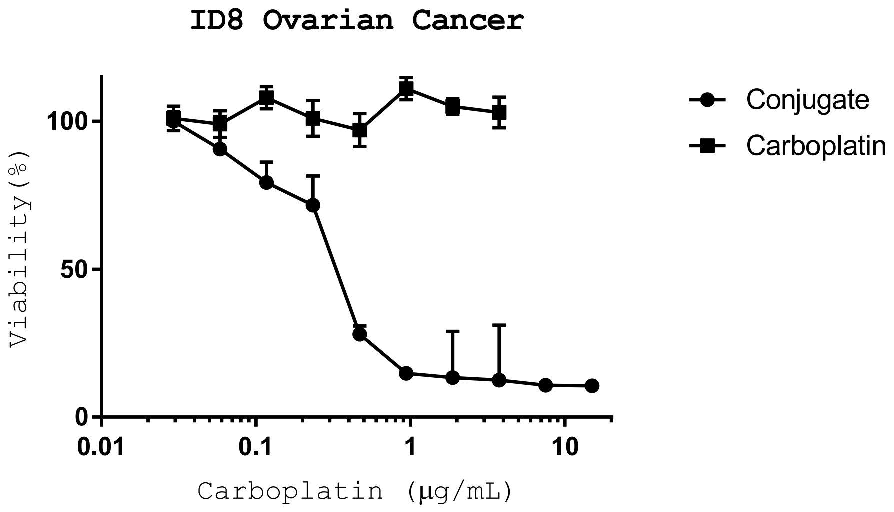

Figure 69: <u>Comparative cytotoxicity of Carboplatin (squares) and conjugate (circles).</u> The viability of ID8 p53$^{-/-}$ ovarian cancer cells treated with either carboplatin (squares) or carboplatin-protein conjugate (circles) was assayed after 24 hours. The annexin A5 – carboplatin conjugate was more toxic than free carboplatin, killing virtually all cells at doses exceeding 100-fold less than free carboplatin. Data is shown as the mean ± SE (n = 8)

Following successful in vitro testing, the in vivo activity of the ANXA5-CBDCA conjugate was ascertained in a murine model of late stage metastatic breast cancer (Figure 70). Female balb/cj mice (n = 5) of 8 weeks of age were inoculated with an orthotopic injection of 10^5 4T1 cells in the IV mammary fat pad and tumors were allowed to develop for 23 days. Starting on day 23 mice were treated daily with 5 μg of CBDCA or ANXA5-CBDCA conjugate. Mouse tumor volumes were recorded twice a week and mouse tumor volume was determined by the formula :

$$[V_{Total} = (V_{tumor} - V_{Necrotic}) = \left(\frac{1}{2} * L * W^2\right)_{tumor} - \left(\frac{1}{2} * L * W^2\right)_{necrosis}].$$

Notable increases in $V_{Necrotic}$ were rapidly observed within 1 week of treatment. A large decrease in total tumor volume was observed 2 weeks after the start of therapy. The study was concluded on day 37 when notable ulceration of the tumors was observed. The ANXA5-CBDCA conjugate significantly reduced tumor volumes in the 4T1 model of drug resistant cancer.

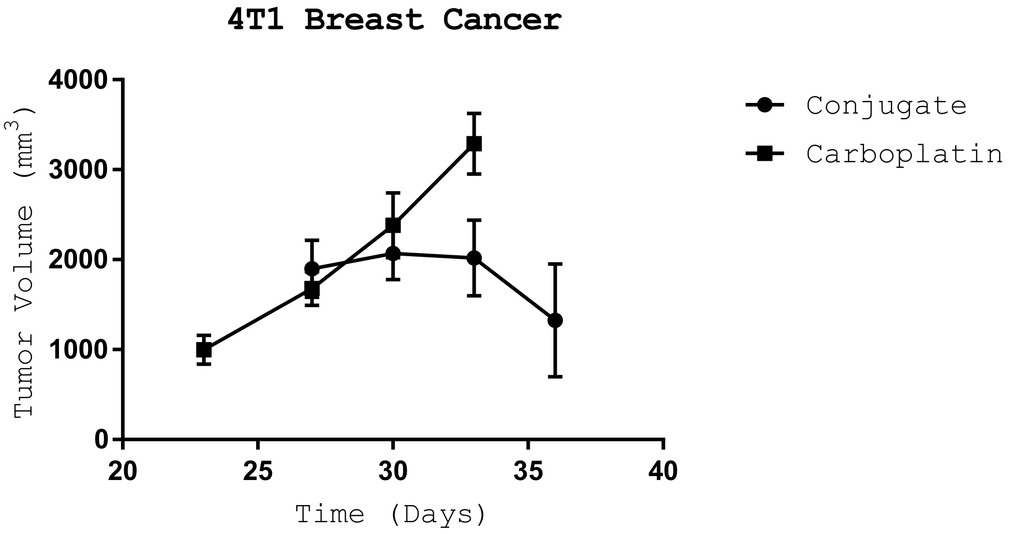

Figure 70: Conjugate dependent tumor growth suppression. The growth of late stage 4T1 metastatic breast cancer was monitored in mice (n=5) for a period of 2 weeks. Female balb/cj mice of 8 weeks of age were inoculated with an orthotopic injection of 105 4T1 cells in the IV mammary fat pad. After a period of 23 days mice were treated daily with 5 μg of carboplatin or carboplatin - protein conjugate.

Mouse tumor volumes were recorded twice a week and mouse tumor volume was determined by the formula [V_tumor-V_Necrosis=(1/3*L*W^2)_tumor-(1/3*L*W^2)_necrosis].

Conclusion

The novel cytocidal bioconjugate ANXA5-CMDCA comprised of the protein ANXA5 linked to the chemotherapeutic CBDCA by EDC/NHS chemistry is a potent anticancer chemotherapeutic. We establish the degree of CDBCA loading on ANXA5 by absorbance spectroscopy, and confirm the anticancer activity of the resulting conjugate in a ID8 ovarian cancer model. We further demonstrate the activity of the conjugate in vivo using the 4T1 model of late stage metastatic breast cancer.

References

[1] G.G. Borisenko, T. Matsura, S.X. Liu, V.A. Tyurin, J. Jianfei, F.B. Serinkan, V.E. Kagan, Macrophage recognition of externalized phosphatidylserine and phagocytosis of apoptotic Jurkat cells--existence of a threshold, Arch Biochem Biophys, 413 (2003) 41-52.

[2] M. Ida, A. Satoh, I. Matsumoto, K. Kojima-Aikawa, Human annexin V binds to sulfatide: contribution to regulation of blood coagulation, J Biochem, 135 (2004) 583-588.

[3] K. Schutters, C. Reutelingsperger, Phosphatidylserine targeting for diagnosis and treatment of human diseases, Apoptosis, 15 (2010) 1072-1082.

[4] R. Huber, M. Schneider, I. Mayr, J. Romisch, E.P. Paques, The calcium binding sites in human annexin V by crystal structure analysis at 2.0 A resolution. Implications for membrane binding and calcium channel activity, FEBS Lett, 275 (1990) 15-21.

[5] F. Oling, W. Bergsma-Schutter, A. Brisson, Trimers, dimers of trimers, and trimers of trimers are common building blocks of annexin a5 two-dimensional crystals, J Struct Biol, 133 (2001) 55-63.

[6] B. Van Rite, J. Krais, M. Cherry, V. Sikavitsas, C. Kurkjian, R. G Harrison, Antitumor Activity of an Enzyme Prodrug Therapy Targeted to the Breast Tumor Vasculature, 2013.

[7] J.J. Krais, O. De Crescenzo, R.G. Harrison, Purine nucleoside phosphorylase targeted by annexin v to breast cancer vasculature for enzyme prodrug therapy, Plos One, 8 (2013) e76403.

[8] J.J. Krais, N. Virani, P.H. McKernan, Q. Nguyen, K.-M. Fung, V.I. Sikavitsas, C.D. Kurkjian, R.G. Harrison, Antitumor Synergism and Enhanced Survival with a Tumor Vasculature-Targeted Enzyme Prodrug System, Rapamycin, and Cyclophosphamide, Molecular Cancer Therapeutics, (2017).

[9] H.M. Hankins, R.D. Baldridge, P. Xu, T.R. Graham, Role of flippases, scramblases and transfer proteins in phosphatidylserine subcellular distribution, Traffic, 16 (2015) 35-47.

[10] A.J. Schroit, J.W. Madsen, Y. Tanaka, In vivo recognition and clearance of red blood cells containing phosphatidylserine in their plasma membranes, J Biol Chem, 260 (1985) 5131-5138.

[11] G. Brouckaert, M. Kalai, D.V. Krysko, X. Saelens, D. Vercammen, M. Ndlovu, G. Haegeman, K. D'Herde, P. Vandenabeele, Phagocytosis of Necrotic Cells by Macrophages Is Phosphatidylserine Dependent and Does Not Induce Inflammatory Cytokine Production, Mol Biol Cell, 15 (2004) 1089-1100.

[12] E. Paplomata, R. O'Regan, The PI3K/AKT/mTOR pathway in breast cancer: targets, trials and biomarkers, Ther Adv Med Oncol, 6 (2014) 154-166.

[13] B.X. Huang, M. Akbar, K. Kevala, H.Y. Kim, Phosphatidylserine is a critical modulator for Akt activation, J Cell Biol, 192 (2011) 979-992.

[14] E.A. Carrera Silva, P.Y. Chan, L. Joannas, A.E. Errasti, N. Gagliani, L. Bosurgi, M. Jabbour, A. Perry, F. Smith-Chakmakova, D. Mucida, H. Cheroutre,

T. Burstyn-Cohen, J.A. Leighton, G. Lemke, S. Ghosh, C.V. Rothlin, T cell-derived protein S engages TAM receptor signaling in dendritic cells to control the magnitude of the immune response, Immunity, 39 (2013) 160-170.

[15] N. Jetten, S. Verbruggen, M.J. Gijbels, M.J. Post, M.P. De Winther, M.M. Donners, Anti-inflammatory M2, but not pro-inflammatory M1 macrophages promote angiogenesis in vivo, Angiogenesis, 17 (2014) 109-118.

[16] Y. Yin, X. Huang, K.D. Lynn, P.E. Thorpe, Phosphatidylserine-targeting antibody induces M1 macrophage polarization and promotes myeloid-derived suppressor cell differentiation, Cancer Immunol Res, 1 (2013) 256-268.

[17] G. Brouckaert, M. Kalai, D.V. Krysko, X. Saelens, D. Vercammen, M.N. Ndlovu, G. Haegeman, K. D'Herde, P. Vandenabeele, Phagocytosis of necrotic cells by macrophages is phosphatidylserine dependent and does not induce inflammatory cytokine production, Mol Biol Cell, 15 (2004) 1089-1100.

[18] M.B. Feinstein, S.M. Fernandez, R.I. Sha'afi, Fluidity of natural membranes and phosphatidylserine and ganglioside dispersions. Effect of local anesthetics, cholesterol and protein, Biochim Biophys Acta, 413 (1975) 354-370.

[19] R. Zeisig, T. Koklic, B. Wiesner, I. Fichtner, M. Sentjurc, Increase in fluidity in the membrane of MT3 breast cancer cells correlates with enhanced cell adhesion in vitro and increased lung metastasis in NOD/SCID mice, Arch Biochem Biophys, 459 (2007) 98-106.

[20] G.V. Sherbet, Membrane fluidity and cancer metastasis, Exp Cell Biol, 57 (1989) 198-205.

[21] E. Bottger, G. Multhoff, J.F. Kun, M. Esen, Plasmodium falciparum-infected erythrocytes induce granzyme B by NK cells through expression of host-Hsp70, Plos One, 7 (2012) e33774.

[22] V.B. Brand, C.D. Sandu, C. Duranton, V. Tanneur, K.S. Lang, S.M. Huber, F. Lang, Dependence of Plasmodium falciparum in vitro growth on the cation permeability of the human host erythrocyte, Cell Physiol Biochem, 13 (2003) 347-356.

[23] P. Joshi, C.M. Gupta, Abnormal membrane phospholipid organization in Plasmodium falciparum-infected human erythrocytes, Br J Haematol, 68 (1988) 255-259.

[24] F.E. Boas, L. Forman, E. Beutler, Phosphatidylserine exposure and red cell viability in red cell aging and in hemolytic anemia, Proc Natl Acad Sci U S A, 95 (1998) 3077-3081.

[25] S. Dinkla, M. Peppelman, J. Van Der Raadt, F. Atsma, V.M. Novotny, M.G. Van Kraaij, I. Joosten, G.J. Bosman, Phosphatidylserine exposure on stored red blood cells as a parameter for donor-dependent variation in product quality, Blood Transfus, 12 (2014) 204-209.

[26] C. Fernandez-Arias, J. Rivera-Correa, J. Gallego-Delgado, R. Rudlaff, C. Fernandez, C. Roussel, A. Gotz, S. Gonzalez, A. Mohanty, S. Mohanty, S. Wassmer, P. Buffet, P.A. Ndour, A. Rodriguez, Anti-Self Phosphatidylserine Antibodies Recognize Uninfected Erythrocytes Promoting Malarial Anemia, Cell Host Microbe, 19 (2016) 194-203.

[27] Z. Bozdech, J. VanWye, K. Haldar, E. Schurr, The human malaria parasite Plasmodium falciparum exports the ATP-binding cassette protein PFGCN20 to membrane structures in the host red blood cell, Mol Biochem Parasitol, 97 (1998) 81-95.

[28] R.A. Kavishe, J.M. van den Heuvel, M. van de Vegte-Bolmer, A.J. Luty, F.G. Russel, J.B. Koenderink, Localization of the ATP-binding cassette (ABC) transport proteins PfMRP1, PfMRP2, and PfMDR5 at the Plasmodium falciparum plasma membrane, Malaria J, 8 (2009) 205.

[29] S. Eda, I.W. Sherman, Cytoadherence of malaria-infected red blood cells involves exposure of phosphatidylserine, Cell Physiol Biochem, 12 (2002) 373-384.

[30] H. Phiri, J. Montgomery, M. Molyneux, A. Craig, Competitive endothelial adhesion between Plasmodium falciparum isolates under physiological flow conditions, Malar J, 8 (2009) 214.

[31] R.B. Birge, S. Boeltz, S. Kumar, J. Carlson, J. Wanderley, D. Calianese, M. Barcinski, R.A. Brekken, X. Huang, J.T. Hutchins, B. Freimark, C. Empig, J. Mercer, A.J. Schroit, G. Schett, M. Herrmann, Phosphatidylserine is a global immunosuppressive signal in efferocytosis, infectious disease, and cancer, Cell Death Differ, 23 (2016) 962-978.

[32] J. Sachs, P. Malaney, The economic and social burden of malaria, Nature, 415 (2002) 680-685.

[33] J.L. Gallup, J.D. Sachs, The economic burden of malaria, Am J Trop Med Hyg, 64 (2001) 85-96.

[34] P. Bloland, Drug resistance in malaria., Geneva, 2001.

[35] L.H. Miller, R.J. Howard, R. Carter, M.F. Good, V. Nussenzweig, R.S. Nussenzweig, Research toward malaria vaccines, Science, 234 (1986) 1349-1356.

[36] M.H. Brooks, J.P. Malloy, P.J. Bartelloni, W.D. Tigertt, T.W. Sheehy, K.G. Barry, Pathophysiology of acute falciparum malaria. I. Correlation of clinical and biochemical abnormalities, Am J Med, 43 (1967) 735-744.

[37] D.A. Warrell, Pathophysiology of severe falciparum malaria in man, Parasitology, 94 Suppl (1987) S53-76.

[38] J.M. Crutcher, S.L. Hoffman, Malaria, in: th, S. Baron (Eds.) Medical Microbiology, Galveston (TX), 1996.

[39] P.H. Schlesinger, D.J. Krogstad, B.L. Herwaldt, Antimalarial agents: mechanisms of action, Antimicrob Agents Chemother, 32 (1988) 793-798.

[40] S. Wilhelm, A.J. Tavares, Q. Dai, S. Ohta, J. Audet, H.F. Dvorak, W.C.W. Chan, Analysis of nanoparticle delivery to tumours, Nature Reviews Materials, 1 (2016) 16014.

[41] I.K. Kwon, S.C. Lee, B. Han, K. Park, Analysis on the current status of targeted drug delivery to tumors, J Control Release, 164 (2012) 108-114.

[42] S.A. Gandhi, J. Kampp, Skin Cancer Epidemiology, Detection, and Management, Med Clin North Am, 99 (2015) 1323-1335.

[43] T.L. Diepgen, V. Mahler, The epidemiology of skin cancer, Br J Dermatol, 146 Suppl 61 (2002) 1-6.

[44] N.H. Matthews, W.Q. Li, A.A. Qureshi, M.A. Weinstock, E. Cho, Epidemiology of Melanoma, in: W.H. Ward, J.M. Farma (Eds.) Cutaneous Melanoma: Etiology and Therapy, Brisbane (AU), 2017.

[45] W.C. Rose, R.L. Wixom, THE AMINO ACID REQUIREMENTS OF MAN: XIII. THE SPARING EFFECT OF CYSTINE ON THE METHIONINE REQUIREMENT, Journal of Biological Chemistry, 216 (1955) 763-774.

[46] J.J. Krais, N. Virani, P.H. McKernan, Q. Nguyen, K.M. Fung, V.I. Sikavitsas, C. Kurkjian, R.G. Harrison, Antitumor Synergism and Enhanced Survival with a Tumor Vasculature-Targeted Enzyme Prodrug System, Rapamycin, and Cyclophosphamide, Mol Cancer Ther, 16 (2017) 1855-1865.

[47] N.W.S. Kam, M. O'Connell, J.A. Wisdom, H. Dai, Carbon nanotubes as multifunctional biological transporters and near-infrared agents for selective cancer cell destruction, Proceedings of the National Academy of Sciences of the United States of America, 102 (2005) 11600-11605.

[48] Y. Xiao, X. Gao, O. Taratula, S. Treado, A. Urbas, R.D. Holbrook, R.E. Cavicchi, C.T. Avedisian, S. Mitra, R. Savla, P.D. Wagner, S. Srivastava, H. He, Anti-HER2 IgY antibody-functionalized single-walled carbon nanotubes for detection and selective destruction of breast cancer cells, BMC Cancer, 9 (2009) 351-351.

[49] X. Liu, H. Tao, K. Yang, S. Zhang, S.T. Lee, Z. Liu, Optimization of surface chemistry on single-walled carbon nanotubes for in vivo photothermal ablation of tumors, Biomaterials, 32 (2011) 144-151.

[50] C. Brace, Thermal Tumor Ablation in Clinical Use, IEEE pulse, 2 (2011) 28-38.

[51] H.O.W. Tseng, S.-E. Lin, Y.-L. Chang, M.-H. Chen, S.-H. Hung, Determining the critical effective temperature and heat dispersal pattern in monopolar radiofrequency ablation using temperature-time integration, Experimental and Therapeutic Medicine, 11 (2016) 763-768.

[52] T. Murakami, H. Nakatsuji, M. Inada, Y. Matoba, T. Umeyama, M. Tsujimoto, S. Isoda, M. Hashida, H. Imahori, Photodynamic and Photothermal Effects of Semiconducting and Metallic-Enriched Single-Walled Carbon Nanotubes, J Am Chem Soc, 134 (2012) 17862-17865.

[53] A. Gilman, The initial clinical trial of nitrogen mustard, Am J Surg, 105 (1963) 574-578.

[54] L.S. Goodman, M.M. Wintrobe, et al., Nitrogen mustard therapy; use of methyl-bis (beta-chloroethyl) amine hydrochloride and tris (beta-chloroethyl) amine hydrochloride for Hodgkin's disease, lymphosarcoma, leukemia and certain allied and miscellaneous disorders, J Am Med Assoc, 132 (1946) 126-132.

[55] L. Vidal, R. Gurion, R. Ram, P. Raanani, O. Bairey, T. Robak, A. Gafter-Gvili, O. Shpilberg, Chlorambucil for the treatment of patients with chronic lymphocytic leukemia (CLL) - a systematic review and meta-analysis of randomized trials, Leuk Lymphoma, 57 (2016) 2047-2057.

[56] V. Goede, B. Eichhorst, K. Fischer, C.M. Wendtner, M. Hallek, Past, present and future role of chlorambucil in the treatment of chronic lymphocytic leukemia, Leuk Lymphoma, 56 (2015) 1585-1592.

[57] A. Begleiter, K. Lee, L.G. Israels, M.R. Mowat, J.B. Johnston, Chlorambucil induced apoptosis in chronic lymphocytic leukemia (CLL) and its relationship to clinical efficacy, Leukemia, 8 Suppl 1 (1994) S103-106.

[58] A. Begleiter, M. Mowat, L.G. Israels, J.B. Johnston, Chlorambucil in chronic lymphocytic leukemia: mechanism of action, Leuk Lymphoma, 23 (1996) 187-201.

[59] J.B. Johnston, L.G. Israels, G.J. Goldenberg, C.D. Anhalt, L. Verburg, M.R. Mowat, A. Begleiter, Glutathione S-transferase activity, sulfhydryl group and glutathione levels, and DNA cross-linking activity with chlorambucil in chronic lymphocytic leukemia, J Natl Cancer Inst, 82 (1990) 776-779.

[60] J.B. Johnston, A.F. Kabore, J. Strutinsky, X. Hu, J.T. Paul, D.M. Kropp, B. Kuschak, A. Begleiter, S.B. Gibson, Role of the TRAIL/APO2-L death receptors in chlorambucil- and fludarabine-induced apoptosis in chronic lymphocytic leukemia, Oncogene, 22 (2003) 8356-8369.

[61] G.C. Kundu, J.R. Schullek, I.B. Wilson, The alkylating properties of chlorambucil, Pharmacol Biochem Behav, 49 (1994) 621-624.

[62] G. Ghislat, E. Knecht, New Ca(2+)-dependent regulators of autophagosome maturation, Commun Integr Biol, 5 (2012) 308-311.

[63] D. Kaushik, M. Mohan, D.M. Borade, O.C. Swami, Ampicillin: rise fall and resurgence, J Clin Diagn Res, 8 (2014) ME01-03.

[64] E.T. Knudsen, G.N. Rolinson, S. Stevens, Absorption and excretion of "Penbritin", Br Med J, 2 (1961) 198-200.

[65] G.N. Rolinson, S. Stevens, Microbiological studies on a new broad-spectrum penicilin, "Penbritin", Br Med J, 2 (1961) 191-196.

[66] K.R. Harrap, Preclinical studies identifying carboplatin as a viable cisplatin alternative, Cancer Treat Rev, 12 Suppl A (1985) 21-33.

[67] N. Sumio, [Metastasis of tumor cell in lymphatic circulation of the lung], Kokyu To Junkan, 39 (1991) 425-430.

[68] Z. Chen, A. Zhang, X. Wang, J. Zhu, Y. Fan, H. Yu, Z. Yang, The Advances of Carbon Nanotubes in Cancer Diagnostics and Therapeutics, Journal of Nanomaterials, 2017 (2017).

[69] A. Sanginario, B. Miccoli, D. Demarchi, Carbon nanotubes as an effective opportunity for cancer diagnosis and treatment, Biosensors, 7 (2017) 9.

[70] L.F. Neves, J.J. Krais, B.D. Van Rite, R. Ramesh, D.E. Resasco, R.G. Harrison, Targeting single-walled carbon nanotubes for the treatment of breast cancer using photothermal therapy, Nanotechnology, 24 (2013) 375104.

[71] T. Kalland, Effects of the immunomodulator LS 2616 on growth and metastasis of the murine B16-F10 melanoma, Cancer Res, 46 (1986) 3018-3022.

[72] N.A. Virani, E. Thavathiru, P. McKernan, K. Moore, D.M. Benbrook, R.G. Harrison, Anti-CD73 and anti-OX40 immunotherapy coupled with a novel biocompatible enzyme prodrug system for the treatment of recurrent, metastatic ovarian cancer, Cancer Lett, 425 (2018) 174-182.

[73] E.M. Knavel, C.L. Brace, Tumor ablation: common modalities and general practices, Tech Vasc Interv Radiol, 16 (2013) 192-200.

[74] M. Nikfarjam, V. Muralidharan, C. Christophi, Mechanisms of focal heat destruction of liver tumors, J Surg Res, 127 (2005) 208-223.

[75] E. Schena, P. Saccomandi, Y. Fong, Laser Ablation for Cancer: Past, Present and Future, Journal of Functional Biomaterials, 8 (2017) 19.

[76] N.A. Virani, C. Davis, P. McKernan, P. Hauser, R.E. Hurst, J. Slaton, R.P. Silvy, D.E. Resasco, R.G. Harrison, Phosphatidylserine targeted single-walled carbon nanotubes for photothermal ablation of bladder cancer, Nanotechnology, 29 (2018) 035101.

[77] R.H. Mole, Whole Body Irradiation—Radiobiology or Medicine?, The British Journal of Radiology, 26 (1953) 234-241.

[78] S. Demaria, B. Ng, M.L. Devitt, J.S. Babb, N. Kawashima, L. Liebes, S.C. Formenti, Ionizing radiation inhibition of distant untreated tumors (abscopal effect) is immune mediated, Int J Radiat Oncol Biol Phys, 58 (2004) 862-870.

[79] S.C. Formenti, S. Demaria, Systemic effects of local radiotherapy, Lancet Oncol, 10 (2009) 718-726.

[80] M.P. Nobler, The abscopal effect in malignant lymphoma and its relationship to lymphocyte circulation, Radiology, 93 (1969) 410-412.

[81] A.G. Duffy, D. Pratt, D.E. Kleiner, D. Mabry, S. Fioravanti, M. Walker, W.D. Figg, S.M. Steinberg, V. Anderson, V. Krishnasamy, B.J. Wood, T.F. Greten, Tremelimumab: A monoclonal antibody against CTLA-4—In combination with radiofrequency ablation (RFA) in patients with biliary tract carcinoma (BTC), Journal of Clinical Oncology, 35 (2017) 316-316.

[82] S.A. Dromi, M.P. Walsh, S. Herby, B. Traughber, J. Xie, K.V. Sharma, K.P. Sekhar, A. Luk, D.J. Liewehr, M.R. Dreher, T.J. Fry, B.J. Wood, Radiofrequency ablation induces antigen-presenting cell infiltration and amplification of weak tumor-induced immunity, Radiology, 251 (2009) 58-66.

[83] A.G. Duffy, S.V. Ulahannan, O. Makorova-Rusher, O. Rahma, H. Wedemeyer, D. Pratt, J.L. Davis, M.S. Hughes, T. Heller, M. ElGindi, A. Uppala, F. Korangy, D.E. Kleiner, W.D. Figg, D. Venzon, S.M. Steinberg, A.M. Venkatesan, V. Krishnasamy, N. Abi-Jaoudeh, E. Levy, B.J. Wood, T.F. Greten, Tremelimumab in combination with ablation in patients with advanced hepatocellular carcinoma, J Hepatol, 66 (2017) 545-551.

[84] M.H.M.G.M. den Brok, R.P.M. Sutmuller, S. Nierkens, E.J. Bennink, C. Frielink, L.W.J. Toonen, O.C. Boerman, C.G. Figdor, T.J.M. Ruers, G.J. Adema, Efficient loading of dendritic cells following cryo and radiofrequency ablation in combination with immune modulation induces anti-tumour immunity, British Journal of Cancer, 95 (2006) 896-905.

[85] J. Zhu, M. Yu, L. Chen, P. Kong, L. Li, G. Ma, H. Ge, Y. Cui, Z. Li, H. Pan, H. Xie, W. Zhou, S. Wang, Enhanced antitumor efficacy through microwave ablation in combination with immune checkpoints blockade in breast cancer: A pre-clinical study in a murine model, Diagnostic and Interventional Imaging, 99 (2018) 135-142.

[86] S. Demaria, N. Kawashima, A.M. Yang, M.L. Devitt, J.S. Babb, J.P. Allison, S.C. Formenti, Immune-Mediated Inhibition of Metastases after Treatment with Local Radiation and CTLA-4 Blockade in a Mouse Model of Breast Cancer, Clinical Cancer Research, 11 (2005) 728.

[87] M.Z. Dewan, A.E. Galloway, N. Kawashima, J.K. Dewyngaert, J.S. Babb, S.C. Formenti, S. Demaria, Fractionated but not single dose radiotherapy induces an immune-mediated abscopal effect when combined with anti-CTLA-4 antibody, Clinical cancer research : an official journal of the American Association for Cancer Research, 15 (2009) 5379-5388.

[88] A. Bang, T.J. Wilhite, L.R.G. Pike, D.N. Cagney, A.A. Aizer, A. Taylor, A. Spektor, M. Krishnan, P.A. Ott, T.A. Balboni, F.S. Hodi, J.D. Schoenfeld, Multicenter Evaluation of the Tolerability of Combined Treatment With PD-1 and CTLA-4 Immune Checkpoint Inhibitors and Palliative Radiation Therapy, International Journal of Radiation Oncology • Biology • Physics, 98 (2017) 344-351.

[89] S. Ugel, E. Peranzoni, G. Desantis, M. Chioda, S. Walter, T. Weinschenk, J.C. Ochando, A. Cabrelle, S. Mandruzzato, V. Bronte, Immune tolerance to tumor antigens occurs in a specialized environment of the spleen, Cell Rep, 2 (2012) 628-639.

[90] K. Geddes, F. Cruz, III, F. Heffron, Analysis of Cells Targeted by Salmonella Type III Secretion In Vivo, PLOS Pathogens, 3 (2007) e196.

[91] B. Shi, J. Geng, Y.H. Wang, H. Wei, B. Walters, W. Li, X. Luo, A. Stevens, M. Pittman, B. Li, S.R. Thompson, H. Hu, Foxp1 Negatively Regulates T Follicular Helper Cell Differentiation and Germinal Center Responses by Controlling Cell Migration and CTLA-4, J Immunol, 200 (2018) 586-594.

[92] S.A. Cobbold, R.E. Martin, K. Kirk, Methionine transport in the malaria parasite Plasmodium falciparum, Int J Parasitol, 41 (2011) 125-135.

[93] J. Liu, E.S. Istvan, I.Y. Gluzman, J. Gross, D.E. Goldberg, Plasmodium falciparum ensures its amino acid supply with multiple acquisition pathways and redundant proteolytic enzyme systems, Proc Natl Acad Sci U S A, 103 (2006) 8840-8845.

[94] C.J. Janse, B. Franke-Fayard, G.R. Mair, J. Ramesar, C. Thiel, S. Engelmann, K. Matuschewski, G.J. van Gemert, R.W. Sauerwein, A.P. Waters, High efficiency transfection of Plasmodium berghei facilitates novel selection procedures, Mol Biochem Parasitol, 145 (2006) 60-70.

[95] J.B. Jensen, W. Trager, Plasmodium falciparum in culture: use of outdated erthrocytes and description of the candle jar method, J Parasitol, 63 (1977) 883-886.

[96] B.W. Huang, E. Pearman, C.C. Kim, Mouse Models of Uncomplicated and Fatal Malaria, Bio Protoc, 5 (2015).

[97] J.M. Carlton, S.V. Angiuoli, B.B. Suh, T.W. Kooij, M. Pertea, J.C. Silva, M.D. Ermolaeva, J.E. Allen, J.D. Selengut, H.L. Koo, J.D. Peterson, M. Pop, D.S. Kosack, M.F. Shumway, S.L. Bidwell, S.J. Shallom, S.E. van Aken, S.B. Riedmuller, T.V. Feldblyum, J.K. Cho, J. Quackenbush, M. Sedegah, A. Shoaibi, L.M. Cummings, L. Florens, J.R. Yates, J.D. Raine, R.E. Sinden, M.A. Harris, D.A. Cunningham, P.R. Preiser, L.W. Bergman, A.B. Vaidya, L.H. van Lin, C.J. Janse, A.P. Waters, H.O. Smith, O.R. White, S.L. Salzberg, J.C. Venter, C.M. Fraser, S.L. Hoffman, M.J. Gardner, D.J. Carucci, Genome sequence and comparative analysis of the model rodent malaria parasite Plasmodium yoelii yoelii, Nature, 419 (2002) 512-519.

[98] L.C. Crowley, A.P. Scott, B.J. Marfell, J.A. Boughaba, G. Chojnowski, N.J. Waterhouse, Measuring Cell Death by Propidium Iodide Uptake and Flow Cytometry, Cold Spring Harb Protoc, 2016 (2016).

[99] E.W. Suradji, T. Hatabu, K. Kobayashi, C. Yamazaki, R. Abdulah, M. Nakazawa, J. Nakajima-Shimada, H. Koyama, Selenium-induced apoptosis-like cell death in Plasmodium falciparum, Parasitology, 138 (2011) 1852-1862.

[100] N. Taguchi, T. Hatabu, H. Yamaguchi, M. Suzuki, K. Sato, S. Kano, Plasmodium falciparum: selenium-induced cytotoxicity to P. falciparum, Exp Parasitol, 106 (2004) 50-55.

[101] W. Peters, Malaria; in Zak O, Sande MA (eds): Handbook of Animal Models of Infection, San Diego, Academic Press, 1999.

[102] R.R. Soares, J.M. da Silva, B.C. Carlos, C.C. da Fonseca, L.S. de Souza, F.V. Lopes, R.M. de Paula Dias, P.O. Moreira, C. Abramo, G.H. Viana, F. de Pila Varotti, A.D. da Silva, K.K. Scopel, New quinoline derivatives demonstrate a promising antimalarial activity against Plasmodium falciparum in vitro and Plasmodium berghei in vivo, Bioorg Med Chem Lett, 25 (2015) 2308-2313.

[103] A. Gellis, N. Primas, S. Hutter, G. Lanzada, V. Remusat, P. Verhaeghe, P. Vanelle, N. Azas, Looking for new antiplasmodial quinazolines: DMAP-catalyzed synthesis of 4-benzyloxy- and 4-aryloxy-2-trichloromethylquinazolines and their in vitro evaluation toward Plasmodium falciparum, Eur J Med Chem, 119 (2016) 34-44.

[104] R.J. Cohen, J.R. Sachs, D.J. Wicker, M.E. Conrad, Methemoglobinemia provoked by malarial chemoprophylaxis in Vietnam, N Engl J Med, 279 (1968) 1127-1131.

[105] S.-J. Yeo, D.-X. Liu, H.S. Kim, H. Park, Anti-malarial effect of novel chloroquine derivatives as agents for the treatment of malaria, Malaria Journal, 16 (2017) 80.

[106] A. Arora, Drug-induced methaemoglobinaemia, Acute Med, 12 (2013) 181.

[107] E.R. Jaffe, G. Neurmann, A Comparision of the Effect of Menadione, Methylene Blue and Ascorbic Acid on the Reduction of Methemoglobin in Vivo, Nature, 202 (1964) 607-608.

[108] J.P. de Kock, L. Tarassenko, Pulse oximetry: theoretical and experimental models, Med Biol Eng Comput, 31 (1993) 291-300.

[109] E.D. Chan, M.M. Chan, M.M. Chan, Pulse oximetry: understanding its basic principles facilitates appreciation of its limitations, Respir Med, 107 (2013) 789-799.

[110] A. Kim, J.H. Oh, J.M. Park, A.S. Chung, Methylselenol generated from selenomethionine by methioninase downregulates integrin expression and induces caspase-mediated apoptosis of B16F10 melanoma cells, J Cell Physiol, 212 (2007) 386-400.

[111] J.E. Spallholz, V.P. Palace, T.W. Reid, Methioninase and selenomethionine but not Se-methylselenocysteine generate methylselenol and superoxide in an in vitro chemiluminescent assay: implications for the nutritional carcinostatic activity of selenoamino acids, Biochem Pharmacol, 67 (2004) 547-554.

[112] R. Zhao, F.E. Domann, W. Zhong, Apoptosis induced by selenomethionine and methioninase is superoxide mediated and p53 dependent in human prostate cancer cells, Mol Cancer Ther, 5 (2006) 3275-3284.

[113] K. Nath, D.S. Nelson, M.E. Putt, D.B. Leeper, B. Garman, K.L. Nathanson, J.D. Glickson, Comparison of the Lonidamine Potentiated Effect of Nitrogen Mustard Alkylating Agents on the Systemic Treatment of DB-1 Human Melanoma Xenografts in Mice, PLoS One, 11 (2016) e0157125.

[114] F. Chen, G. Xu, X. Qin, X. Jin, S. Gou, Hybrid of DNA-targeting Chlorambucil with Pt(IV) Species to Reverse Drug Resistance, J Pharmacol Exp Ther, 363 (2017) 221-239.

[115] K. Omer, K. Fox, D. Palermo, L. Boyle, C. Youngson, An in vitro evaluation of resonant frequency analysis to measure fixed bridge stability, BDJ Open, 1 (2015) 15001.

[116] D. Garcia-Sanchez, A. San Paulo, M.J. Esplandiu, F. Perez-Murano, L. Forró, A. Aguasca, A. Bachtold, Mechanical Detection of Carbon Nanotube Resonator Vibrations, Physical Review Letters, 99 (2007) 085501.

[117] R.F. Gibson, E.O. Ayorinde, Y.-F. Wen, Vibrations of carbon nanotubes and their composites: A review, Composites Science and Technology, 67 (2007) 1-28.

[118] H. Hayashi, K. Takahashi, T. Ikuta, T. Nishiyama, Y. Takata, X. Zhang, Direct evaluation of ballistic phonon transport in a multi-walled carbon nanotube, Applied Physics Letters, 104 (2014) 113112-1131125.

[119] C.J. Gannon, P. Cherukuri, B.I. Yakobson, L. Cognet, J.S. Kanzius, C. Kittrell, R.B. Weisman, M. Pasquali, H.K. Schmidt, R.E. Smalley, S.A. Curley, Carbon nanotube-enhanced thermal destruction of cancer cells in a noninvasive radiofrequency field, Cancer, 110 (2007) 2654-2665.

[120] D.M. Pozar, Microwave engineering, Fourth edition. Hoboken, NJ : Wiley, [2012] ©20122012.

[121] S. Iijima, Helical microtubules of graphitic carbon, Nature, 354 (1991) 56.

[122] A. Dimarco, L. Valentine, B.M. Scarpinato, T. Dasdia, M. Soldati, M. Gaetani, P. Orezzi, R. Silvestrini, Daunomycin New Antibiotic of Rhodomycin Group, Nature, 201 (1964) 706-+.

[123] C. Tan, H. Tasaka, K.P. Yu, M.L. Murphy, D.A. Karnofsky, Daunomycin an Antitumor Antibiotic in Treatmentt of Neoplastic Disease - Clinical Evaluation with Special Reference to Childhood Leukemia, Cancer, 20 (1967) 333-+.

[124] H. Ali-Boucetta, K. Al-Jamal, D. McCarthy, M. Prato, A. Bianco, K. Kostarelos, Multiwalled carbon nanotube–doxorubicin supramolecular complexes for cancer therapeutics, Chemical Communications, 2008 (2008) 459-461.

[125] X. Zhang, L. Meng, Q. Lu, Z. Fei, P. Dyson, Targeted delivery and controlled release of doxorubicin to cancer cells using modified single wall carbon nanotubes, Biomaterials, 30 (2009) 6041-6047.

[126] R.B. Li, R.A. Wu, L.A. Zhao, Z.Y. Hu, S.J. Guo, X.L. Pan, H.F. Zou, Folate and iron difunctionalized multiwall carbon nanotubes as dual-targeted drug nanocarrier to cancer cells, Carbon, 49 (2011) 1797-1805.

[127] Z. Liu, A. Fan, K. Rakhra, S. Sherlock, A. Goodwin, X. Chen, Q. Yang, D. Felsher, H. Dai, Supramolecular Stacking of Doxorubicin on Carbon Nanotubes for in vivo Cancer Therapy, Angewandte Chemie (International ed. in English), (2009).

[128] P. Chaudhuri, S. Soni, S. Sengupta, Single-walled carbon nanotube-conjugated chemotherapy exhibits increased therapeutic index in melanoma, Nanotechnology, 21 (2010) 025102.

[129] Z.F. Ji, G.F. Lin, Q.H. Lu, L.J. Meng, X.Z. Shen, L. Dong, C.L. Fu, X.K. Zhang, Targeted therapy of SMMC-7721 liver cancer in vitro and in vivo with carbon nanotubes based drug delivery system, J Colloid Interf Sci, 365 (2012) 143-149.

[130] B. Rosenberg, L. Vancamp, J.E. Trosko, V.H. Mansour, Platinum Compounds - a New Class of Potent Antitumour Agents, Nature, 222 (1969) 385-+.

[131] M. Arlt, D. Haase, S. Hampel, S. Oswald, A. Bachmatiuk, R. Klingeler, R. Schulze, M. Ritschel, A. Leonhardt, S. Fuessel, B. Buchner, K. Kraemer, M.P. Wirth, Delivery of carboplatin by carbon-based nanocontainers mediates increased cancer cell death, Nanotechnology, 21 (2010).

[132] A. Bhirde, V. Patel, J. Gavard, G. Zhang, A. Sousa, A. Masedunskas, R. Leapman, R. Weigert, J. Gutkind, J. Rusling, Targeted killing of cancer cells in vivo and in vitro with EGF-directed carbon nanotube-based drug delivery, (2009).

[133] S. Hampel, D. Kunze, D. Haase, K. Krämer, M. Rauschenbach, M. Ritschel, A. Leonhardt, J. Thomas, S. Oswald, V. Hoffmann, Carbon nanotubes filled with

a chemotherapeutic agent: a nanocarrier mediates inhibition of tumor cell growth, Nanomedicine, 3 (2008) 175-182.

[134] M.C. Wani, H.L. Taylor, M.E. Wall, P. Coggon, A.T. Mcphail, Plant Antitumor Agents .6. Isolation and Structure of Taxol, a Novel Antileukemic and Antitumor Agent from Taxus-Brevifolia, J Am Chem Soc, 93 (1971) 2325-&.

[135] W.P. Mcguire, E.K. Rowinsky, N.B. Rosenshein, F.C. Grumbine, D.S. Ettinger, D.K. Armstrong, R.C. Donehower, Taxol - a Unique Antineoplastic Agent with Significant Activity in Advanced Ovarian Epithelial Neoplasms, Ann Intern Med, 111 (1989) 273-279.

[136] J.A. Yared, K.H.R. Tkaczuk, Update on taxane development: new analogs and new formulations, Drug Des Dev Ther, 6 (2012) 371-384.

[137] J. Chen, S. Chen, X. Zhao, L. Kuznetsova, S. Wong, I. Ojima, Functionalized Single-Walled Carbon Nanotubes as Rationally Designed Vehicles for Tumor-Targeted Drug Delivery, J. Am. Chem. Soc, 130 (2008) 16778-16785.

[138] Z. Liu, K. Chen, C. Davis, S. Sherlock, Q. Cao, X. Chen, H. Dai, Drug delivery with carbon nanotubes for in vivo cancer treatment, Cancer Res, 68 (2008) 6652.

[139] C. Lay, H. Liu, H. Tan, Y. Liu, Delivery of paclitaxel by physically loading onto poly (ethylene glycol)(PEG)-graft-carbon nanotubes for potent cancer therapeutics, Nanotechnology, 21 (2010) 065101.

[140] B. Sharma, S.S. Kanwar, Phosphatidylserine: A cancer cell targeting biomarker, Semin Cancer Biol, (2017).

[141] H. Kenis, C. Reutelingsperger, Targeting phosphatidylserine in anti-cancer therapy, Curr Pharm Des, 15 (2009) 2719-2723.

[142] S. Ran, P.E. Thorpe, Phosphatidylserine is a marker of tumor vasculature and a potential target for cancer imaging and therapy, Int J Radiat Oncol Biol Phys, 54 (2002) 1479-1484.

[143] J.I. Fletcher, M. Haber, M.J. Henderson, M.D. Norris, ABC transporters in cancer: more than just drug efflux pumps, Nature Reviews Cancer, 10 (2010) 147.

[144] A. Pohl, P.F. Devaux, A. Herrmann, Function of prokaryotic and eukaryotic ABC proteins in lipid transport, Biochim Biophys Acta, 1733 (2005) 29-52.

[145] A. Dlugosz, A. Janecka, ABC Transporters in the Development of Multidrug Resistance in Cancer Therapy, Curr Pharm Des, 22 (2016) 4705-4716.

[146] J.I. Fletcher, R.T. Williams, M.J. Henderson, M.D. Norris, M. Haber, ABC transporters as mediators of drug resistance and contributors to cancer cell biology, Drug Resist Updat, 26 (2016) 1-9.

[147] T. Ishikawa, H. Saito, H. Hirano, Y. Inoue, Y. Ikegami, Human ABC transporter ABCG2 in cancer chemotherapy: drug molecular design to circumvent multidrug resistance, Methods Mol Biol, 910 (2012) 267-278.

[148] R.J. Kathawala, P. Gupta, C.R. Ashby, Jr., Z.S. Chen, The modulation of ABC transporter-mediated multidrug resistance in cancer: a review of the past decade, Drug Resist Updat, 18 (2015) 1-17.

[149] N. Hisamoto, A. Tsuge, S.I. Pastuhov, T. Shimizu, H. Hanafusa, K. Matsumoto, Phosphatidylserine exposure mediated by ABC transporter activates

the integrin signaling pathway promoting axon regeneration, Nat Commun, 9 (2018) 3099.

[150] J. Campos-Salinas, D. Leon-Guerrero, E. Gonzalez-Rey, M. Delgado, S. Castanys, J.M. Perez-Victoria, F. Gamarro, LABCG2, a new ABC transporter implicated in phosphatidylserine exposure, is involved in the infectivity and pathogenicity of Leishmania, PLoS Negl Trop Dis, 7 (2013) e2179.

[151] F. Toti, V. Schindler, J.F. Riou, G. Lombard-Platet, E. Fressinaud, D. Meyer, A. Uzan, J.B. Le Pecq, J.L. Mandel, J.M. Freyssinet, Another link between phospholipid transmembrane migration and ABC transporter gene family, inferred from a rare inherited disorder of phosphatidylserine externalization, Biochem Biophys Res Commun, 241 (1997) 548-552.

[152] H. Woehlecke, A. Pohl, N. Alder-Baerens, H. Lage, A. Herrmann, Enhanced exposure of phosphatidylserine in human gastric carcinoma cells overexpressing the half-size ABC transporter BCRP (ABCG2), Biochem J, 376 (2003) 489-495.

[153] D. Cerezo, M. Lencina, A.J. Ruiz-Alcaraz, J.A. Ferragut, M. Saceda, M. Sanchez, M. Canovas, P. Garcia-Penarrubia, E. Martin-Orozco, Acquisition of MDR phenotype by leukemic cells is associated with increased caspase-3 activity and a collateral sensitivity to cold stress, J Cell Biochem, 113 (2012) 1416-1425.

[154] Z. Sulova, J. Orlicky, R. Fiala, I. Dovinova, B. Uhrik, M. Seres, L. Gibalova, A. Breier, Expression of P-glycoprotein in L1210 cells is linked with rise in sensitivity to Ca2+, Biochem Biophys Res Commun, 335 (2005) 777-784.

[155] W.J. Jusko, Fluorometric analysis of ampicillin in biological fluids, J Pharm Sci, 60 (1971) 728-732.

[156] G. Poje, R.J. Redfield, General methods for culturing Haemophilus influenzae, Methods Mol Med, 71 (2003) 51-56.

[157] C.R. Raetz, Phosphatidylserine synthetase mutants of Escherichia coli. Genetic mapping and membrane phospholipid composition, J Biol Chem, 251 (1976) 3242-3249.

[158] K.E. Langley, E. Hawrot, E.P. Kennedy, Membrane assembly: movement of phosphatidylserine between the cytoplasmic and outer membranes of Escherichia coli, J Bacteriol, 152 (1982) 1033-1041.

[159] V.V. Berezhinskaia, G.V. Dolgova, G.G. Egorenko, T.P. Svinogeeva, L.A. Shtegel'man, T.V. Smolkina, A.V. Nikitin, [Study of general toxic and organotropic properties of ampicillin combined with sulbactam], Antibiot Khimioter, 37 (1992) 25-28.

[160] H. Soori, A. Rabbani-Chadegani, J. Davoodi, Exploring binding affinity of oxaliplatin and carboplatin, to nucleoprotein structure of chromatin: spectroscopic study and histone proteins as a target, Eur J Med Chem, 89 (2015) 844-850.

Appendix A: Antimalarial Supplemental Data

Protocols

Candle Jar Method

The Candle Jar Method described by Jensen et al in 1977 is the first method of culturing malaria parasites in vitro [95]. Malaria parasites are sensitive to atmospheric concentrations of oxygen. This method of culturing parasites takes advantage of several common pieces of laboratory equipment to create a suitable atmosphere for the culture of the parasites. In an airtight chamber, typically a candlejar, a sample of blood infected with malaria is placed along with a candle. The candle is lit, and the airtight jar sealed. The candle will deplete the oxygen in the jar and extinguish. The oxygen depleted atmosphere within the jar is suitable for the culture of parasites.

Mouse Model

Adult mice of an age ranging between 6 to 8 weeks old, will be inoculated with P. berghei ANKA parasites. They will be inoculated either intravenously (i.v.) via a lateral tail vein with 10^5 parasitized erythrocytes (pRBC), or alternatively through an intraperitoneal injection of 10^6 pRBC. The percent of infected -

erythrocytes out of all erythrocytes (% parasitemia) will rise over the next several weeks. As parasite numbers increase the mice will begin to become ill. At approximately 5 days post infection (p.i.) mice will begin to exhibit minor symptoms of infection including lethargy, ruffled fur and hunching. Within 48 hours after the initial display of symptoms, mice will begin to display more severe neurological symptoms such as convulsions, limb paralysis and coma. Mice that survive the 6 to 10 day window of severe neurological symptoms will die ~20 days p.i. from hyperparasitemia and anemia.

Infection of C57BL/6J with PbA

1. PbA stabilate (approximately 0.2–0.5 mL with 1–5 % parasitemia, when frozen down) will be kept in liquid nitrogen until required. This preparation will contain pRBC in a glycerol-rich (15 % v/v) buffered, serum-free medium.
2. Immediately prior to inculcation the vial of PbA stabilate will be defrosted.
3. Stabilate will be loaded into a 1 mL syringe capped with a 26 or 27G needle. Stabilate volume will not exceeding 200 μL and will contain 10^5 to 10^6 pRBC. The stabilate will be injected intraperitoneally into a 6-8 week old C57BL/6J mouse.

4. Mice will then be monitored daily as per the “Monitoring Infected Mice” section of the animal models of disease manual[101].

Determination of Peripheral Blood parasitemia

1. Using a sterile scalpel, <1 mm of the tail will be removed.
2. Gently running both thumb, and index finger along the left and right lateral vein of the tail will milk a small drop of blood from the mouse.
3. Parasites will be enumerated via blood smear or flow cytometry.
    - A) In the case of blood smear, a single drop of blood will be collected on a glass slide, dried and then sterilized and fixed in methanol for 2 minutes. The slide will then be stained with giemsa and parasites will be counted via light microscopy.
    - B) In the case of flow cytometry, a single drop of blood will be collected into a polystyrene microcentrifuge tube. Blood cells will be isolated by centrifugication, and then sterilized and fixed in 4% paraformaldehyde for 10 minutes. Fixed cells will then be enumerated by flow cytometry

Monitoring Infected Mice

1. Mice will be visually assessed twice daily starting 5 p.i. , or when parasitemia exceeds 4%.
2. Mice will be assigned clinical scores corresponding the severity of their symptoms.
    A) Each of the following symptoms is assigned a score of 1: ruffled fur, hunching, wobbly gait, limb paralysis, convulsions, and coma.
    B) When the cumulative score equals or exceeds 4, the animal shall be euthanized by C02 asphyxiation, followed by cervical dislocation. Following euthanasia records shall be updated to show a score of '5' indicating euthanasia.

Preparation of pRBC Aliquots for future Inoculation

1. Infected mice of 1-4% parasitemia will be euthanized by C02 asphyxiation followed by cervical dislocation.
2. Infected blood will be collected by cardiac puncture in a tuberculin syringe.
3. Blood will be diluted in cell growth media, enumerated, and aliquoted for either immediate use or for cryopreservation.
    A) Blood for immediate use will be inoculated into mice as per the "Infection of C57BL/6J with PbA" section.

B) Blood to be preserved via cryopreservation will be aliquoted into glycerol rich media and frozen under liquid N2

Euthanasia Criteria

1. Mice will be euthanized when their cumulative symptom score equals or exceeds 4 (See recommended euthanasia guide IACUC).
2. Mice will be euthanized if they lose greater than 10% of their study start weight.
3. Mice will be euthanized regardless of cumulative symptom score if they display convulsions, and or coma.
4. Mice will be euthanized if in any way demonstrate obvious pain or stress not detailed in this protocol.

Production of Annexin

Protein Expression & Purification of AV

- Day before starting, autoclave the following items:
- 1 liter LB medium
- 4 1 liter Erlenmeyer flask (with aluminum foil on top)
- 125 ml Erlenmeyer flask (with aluminum foil on top)
- 100 ml beaker (with aluminum foil on top)
- All size tips
- 1.5 ml centrifuge tubes (like 100)
- 1 liter DI water

Protein Expression

<u>Day 1: 2100</u>

1. Culture 5 µlof E. coliBL21(DE3) harboring pET303CT with the fusion gene AV in10 ml of LB medium containing 35 mg/ml kanamycin in a 125 ml Erlenmeyer flask overnight at 37oC with shaking at 200 rpm.

- LB medium: 1 liter DI H2O + 10 g Tryptone + 5 g Yeast Extract + 5 g NaCl.

- Add 35 mg kanamycin to the 1 L of LB medium before taking out the 10 ml for the initial culture.
- Incubate overnight.

Day 2: 900

2. Add 10 ml of the cell culture to 1 liter of fresh culture medium+ kanamycin and incubate at 37oC with shaking (200 rpm). Take 1.5 mL of medium before adding the bacteria, as a blank. This cell culture was grown to mid-log phase => OD600 = 0.5.

- Transfer 10 mL of bacteria to 1 L LB medium.
- Transfer entire volume of medium to four 1 L flasks.
- Put in shaker at 37o C at 200 rpm.
- After 1.5 h of shaking, measure optical density at 600 nm (absorbance). When OD600nm = 0.5 (between .5 and .8 is good), then proceed to next step.

Day 2: 1445

3. Addisopropyl □-D-thiogalactopyranoside (IPTG - stored @ -20ºC top shelf) to a final concentration of 0.4 mM(96 mg IPTG total – 24 mg per

flask)to solutions in four 1 L flasksand incubate at 30oC with shaking (180 rpm) for 5 h to induce protein expression.

- Take 750 ml sample of solution before adding IPTG. Label it 'BI.'
- Add 24 mg IPTG to each flask.
- Put back in shaker at 30oC for 5 hours.

\- IPTG stimulates the production of fusion protein. (IPTG activates the promoter in the plasmid that will start the transcription of the gene that follows the promoter =>Annexin A5 gene.)

Day 2: 1945

4. Harvest the cells by centrifugation for 10 min at 1000 x g, at 4ºC.
   - Take 750 ml sample before centrifuge. Label sample 'BC.'
   - Centrifuge at 1000xg = ~3000 rpm (centrifuge uses rpm – consult table on machine). Only 4 – 50 ml centrifuge tubes at a time, temp 4ºC, 10 mins.
   - After first centrifuge, pour out supernatant, add more culture to same 4 tubes. Bacteria will be stuck to side of tubes so inverting to pour out is not a problem.
   - Place the 4 tubes in -20ºC freezer for overnight storage.

Day 3 1000

5. Resuspendthe cell pellet in 40 ml of sonication buffer.
   - Add ~10 ml to each of the 4 centrifuge tubes.
   - Vortex to resuspend cell pellets.
   - Pour contents of the 4 tubes back into the 100 ml beaker.
   - Sonication Buffer Recipe
     - TPC -0.704 mg.
     - PMSF -6.968 mg.
     - HPLC EtOH - 400 µl.
     - β-mercaptoethanol - 4 µl.
     - sodium phosphate dibasic – 113.6 mg.
     - 40 mL DI H_2O
     - Dissolve TPC and PMSF in EtOH
     - Mix remaining ingredients in a beaker
     - Correct solution to pH 7.4 – using HCl
6. Lyse the cells by sonication on ice for 30 sec at 5 watts then allow it to cool for 30 sec on ice. Repeat this cycle 4 more times.
7. Centrifuge the lysate obtained at 12,000 x g for 30 min to remove the cell debris and take the supernatant.

Protein Purification

Day 3: 1200

8. Add to lysed cells:
    - imidazole - 0.0817 g
    - NaCl - 1.168 g
9. Equilibrate a 5 ml HisTrap chromatography column with Wash Buffer 1.
    - WASH BUFFER 1 Recipe
        - 500 mL of diH_2O
        - sodium phosphate dibasic - 1.42 g
        - imidazole - 1.362 g
        - 500 mMNaCl - 14.61 g
        - Correct this to pH 7.4
10. Feed the soluble protein fraction into the column.
11. Remove endotoxin with 350 mL of Wash buffer 2
    - WASH BUFFER 2 (300 mL)
        - sodium phosphate dibasic - 0.8517 g
        - imidazole - 0.817 g
        - NaCl - 8.766 g
        - Trition X-114 - 3 ml
        - Correct this to pH 7.4

12. Remove wash buffer 2 with 100 mL of Wash buffer 1.
    - Wash buffer 2 interferes with Bradford reagent
13. Elute the protein using elution buffer and collect the elution.
    - ELUTION BUFFER (300 mL)
        - sodium phosphate dibasic - 0.8517 g
        - imidazole - 10.212 g
        - NaCl - 8.766 g
        - Correct this to pH 7
14. Dialyze eluted protein for 3 hours against 2 liters of dialysis buffer
    - DIALYSIS BUFFER
        - 2 L of diH_2O
        - sodium phosphate dibasic =>5.678 g
        - Adjust to pH 7.4
15. Regenerate the Column with 25 mL each of:
    - KCl (14.91 g in 200 mL diH_2O)
    - NaOH (8.0 g in 200 mL of diH_2O)
    - diH_2O
    - HPLC Grade EtOH (1.46 mL EtOH in 23.5 mL diH_2O)
16. Measure the concentration of protein
17. Cleave the C-terminal His-tag

Day 4 1000

18. Equilibrate the HisTrap column with Wash Buffer 1.

19. Add imidazole (40 mM) and NaCl (500 mM) to the cleaved protein solution

20. Feed the solution to theHisTrap column.

- The protein is in the flow through of this stage.

21. Feed Wash Buffer 1 into column to pull out all cleaved protein before proceeding forward.

22. Elute uncleaved protein with elution buffer.

23. Dialyze purified protein for 3 hours against 2 liters of dialysis buffer.

- DIALYSIS 2 BUFFER
  - sodium phosphate dibasic - 5.5678 g
  - NaCl - 11.688 g
  - Adjust to pH 7.4

24. Regenerate the column as above.

25. Sterile filter the protein with a 0.22 uM filter

27. Aliquot purified protein into cryovials

28. Perform Bradford concentration, annexin binding, SDS-page size, and mCGL activity confirmation assays

Hemoglobin Oxidation

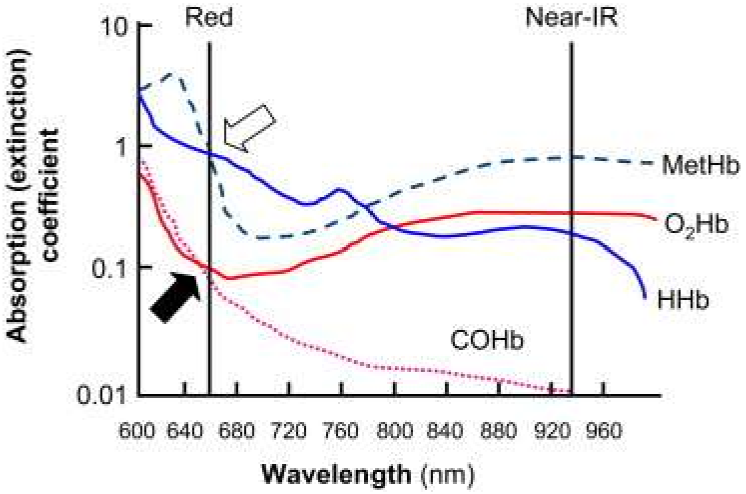

Figure 71: Spectroscopic Analysis Blood [109].
The relative oxidation state of hemoglobin can be determined by comparative absorbance spectroscopy at 660 and 940 nm.

Parasite Gating Scheme

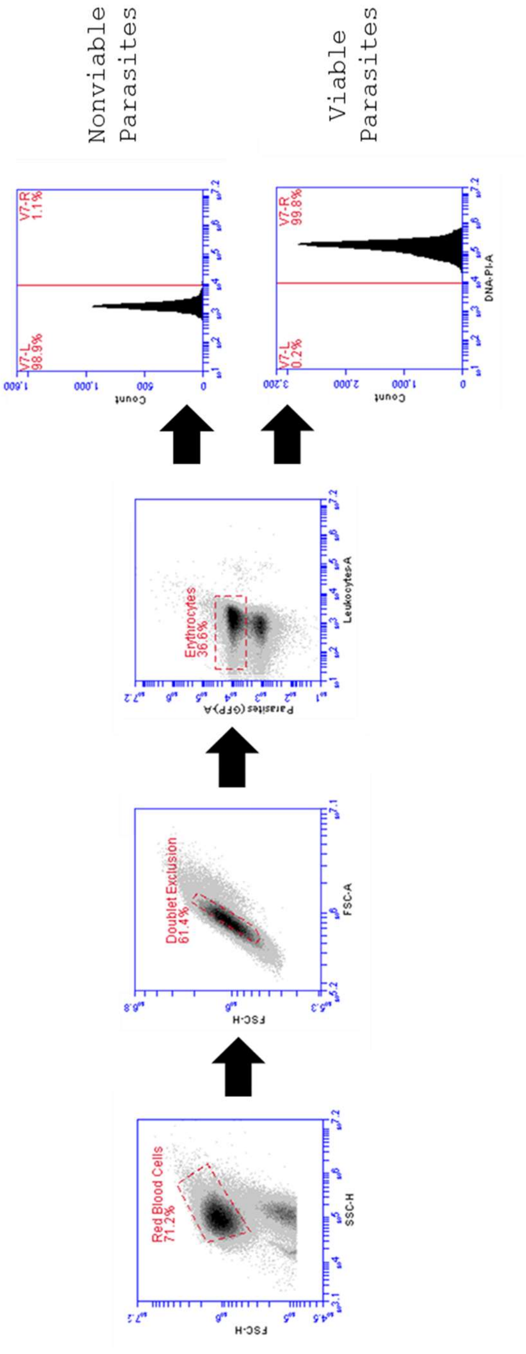

Erythrocyte Damage Flow Scheme

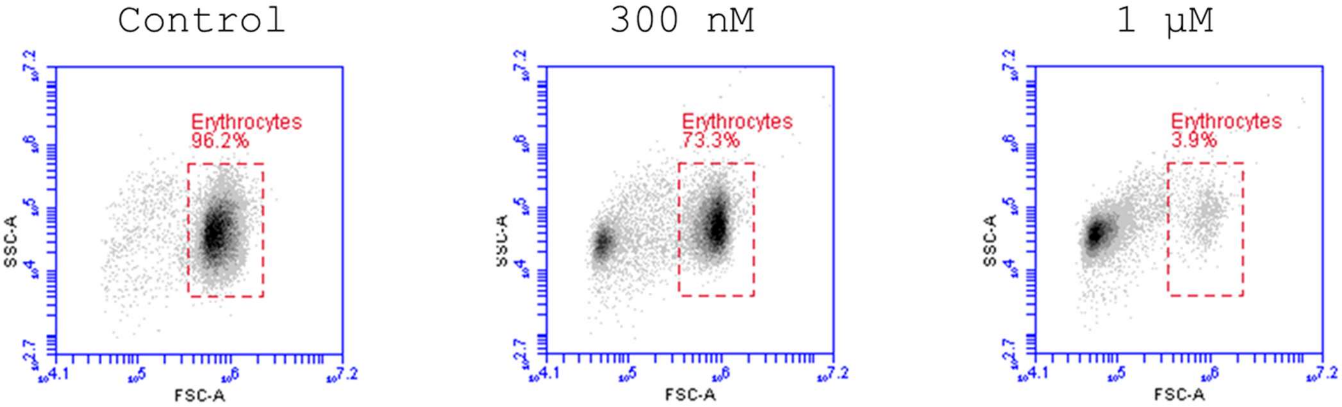

Giemsa Stain Protocol

1) Fix slides in ice cold 100% methanol for ~30” and rinse off in tap water.
2) Make up a fresh solution of 10% Giemsa stain in distilled water.
3) Stain samples for ~30 – 45 minutes, and observe color development to determine rate of stain uptake.
4) Rinse off slide in tap water and dry thoroughly using bibulous paper to dab.

Estimation of Parasitemia

5) View slide under oil immersion with a 100x objective.
6) Estimate parasitemia by counting the number of infected cells. A 10x10 grid square in the eyepiece of the microscope facilitates the procedure as an even blood smear yields ~100 erythrocytes per 10x10 grid. Thus for example, 8 infected blood cells in a 10x10 grid is ~8% parasitemia. Several fields (~10) should be counted and the average taken to obtain a representative estimate of the total parasitemia.

Stability of the Fusion Protein

The enzyme activity of fusion protein (mCGL-ANXA5) was monitored over a period of one month. The activity of samples stored at several temperature conditions (4, 25 and 37 °C) was ascertained by colormetric assay. Colormetric production of α-ketobutrate with 3-Methyl-2-benzo-thiazolinone hydrazone hydrochloride hydrate was quantified and compared to controls of fresh enzyme to determine activity (%). Stability of the enzyme was found to decrease rapidly under all storage conditions, with the exception of flash frozen samples which maintained all activity.

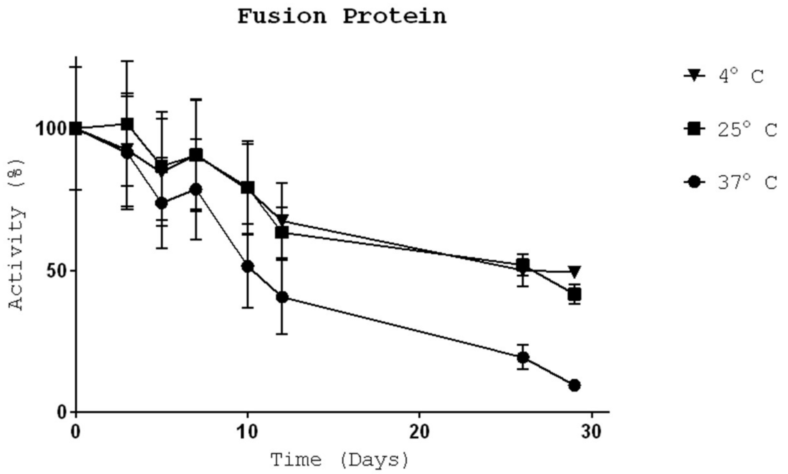

Figure 72: Fusion protein enzymatic stability.
The enzyme activity of fusion protein (mCGL-AV) was monitored over a period of one month. The activity of samples stored at several temperature conditions (4, 25 and 37 °C) was ascertained by colormetric assay. Colormetric detection of α-ketobutrate with 3-Methyl-2-benzo-thiazolinone hydrazone hydrochloride hydrate was quantified and compared to controls of fresh enzyme to determine activity (%).

PP3 Cofactor

The activity of the fusion protein (mCGL-ANXA5) is highly dependent on the cofactor pyridoxal-3-phosphate (PP3). PP3 or PLP otherwise known as vitamin B6, catalyzes the activity rate of the apoenzyme by several order of magnitude. The activity of the haloenzyme can also be increased by 100% with excess (28 mM) PP3.

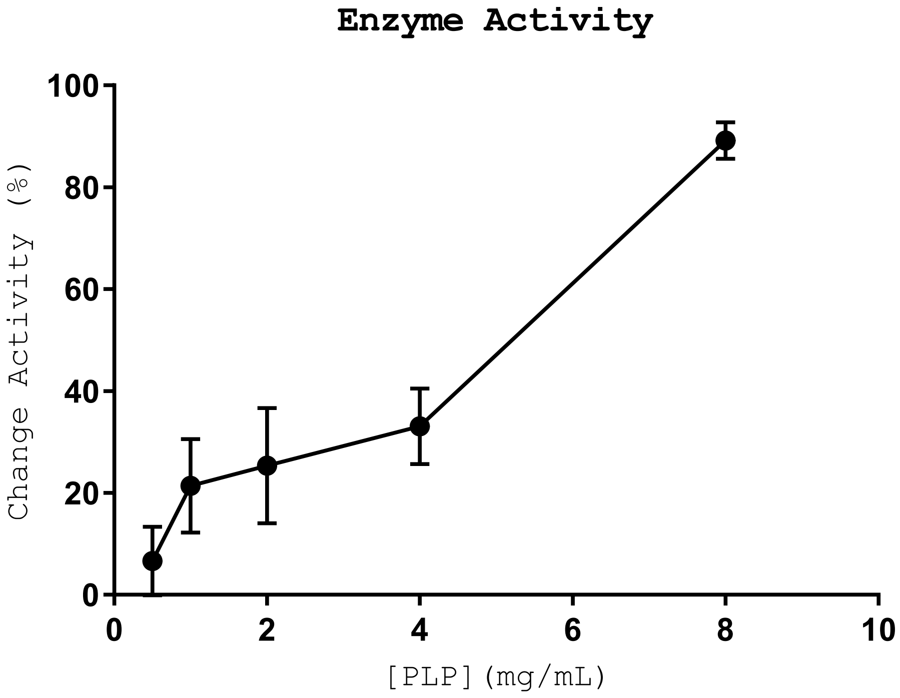

Figure 73: Cofactor dependent activity.
The activity of the fusion protein (mCGL-ANXA5) is dependent on the cofactor PP3.Significant changes in activity were observed in samples (n = 3) of mCGL-ANXA5 incubated with PP3.

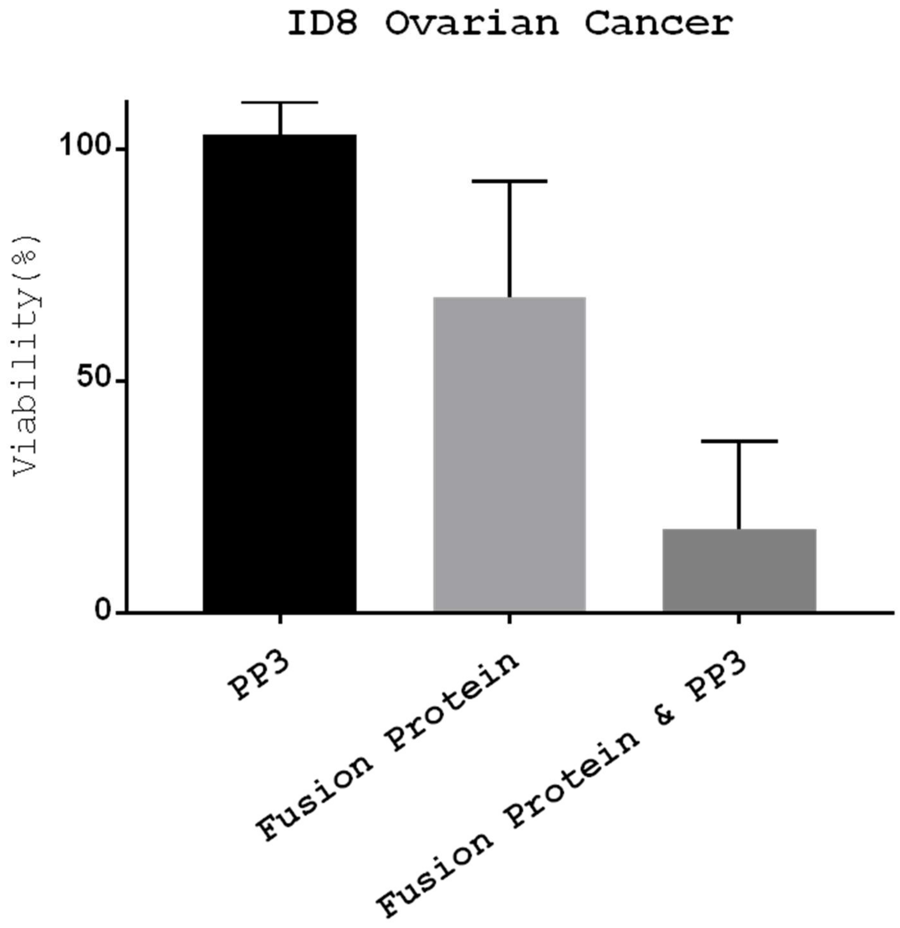

Figure 74: Cofactor dependent cytotoxicity.
The cytostatic activity of the fusion protein (mCGL-ANXA5) can be increased in vitro with supplemental PP3. Ovarian cells were incubated for 48 hours with 3,500 nM PP3 or 500 nM of fusion protein supplemented with excess PP3. While PP3 has no effect on cells by itself, it catalyzes the cystathionine-γ-lyase activity of the fusion protein increasing cell death compared to fusion protein alone.

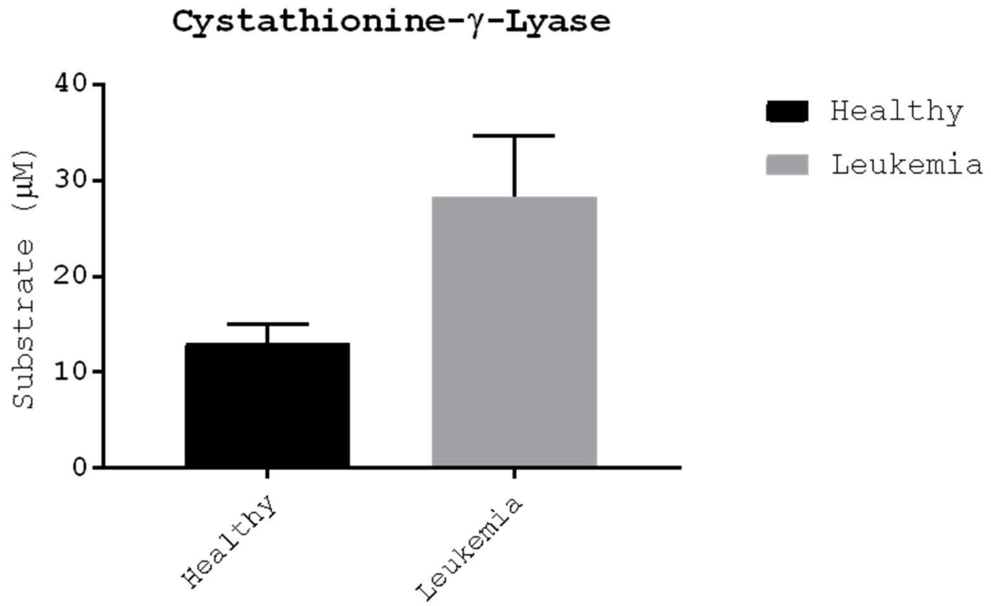

Figure 75: Increased cysthathionine-γ-lyase substrate can be detected in blood from mice inoculated with L1210 leukemia.
The colorimetric detection of products of mCGL enzyme activity in mice with leukemia hints at possible uses of ANXA5-mCGL in diseases other than malaria.

Parasite Isolation

- Prepare 90% (vol/vol) Percoll (200 ml) by mixing 20 ml of 10× PBS with 180 ml of Percoll.
- Prepare 65% (vol/vol) Percoll by combining 6.5 ml of 90% Percoll with 2.5 ml of incomplete culture medium

- Prepare 35% (vol/vol) Percoll by combining 3.5 ml of 90% Percoll with 5.5 ml of incomplete culture medium.
- Mix well and sterilize by filtration through a 0.22-µm filter. The sterile 90, 65 and 35% Percoll solutions are stored at 4 °C for up to 1 year.

Percol Gradient Casting:

To cast a step Percoll gradient, use a 3-ml plastic pipette to load 35% (vol/vol) Percoll on top of 65% (vol/vol) Percoll (2 ml of each concentration). Hold the pipette so that the end is against the inner wall of the 15-ml Falcon tube. Slowly release the 35% (vol/vol) Percoll on to the 65% (vol/vol) Percoll layer so that a sharp interface forms between the two Percoll layers.

Isolation of of Parasitized RBCs

1) Transfer the parasite culture from the 25-cm^2 flask to a 15-ml disposable Falcon tube. Centrifuge at 2,000 r.p.m. (~500g) for 5 min at room temperature. Discard the supernatant. Resuspend the cells with incomplete culture medium to 10% hematocrit (total ~2.5 ml).
2) Slowly layer cell suspension on top of the freshly prepared Percoll gradient
3) Centrifuge in a swing-out rotor at 1,500g at room temperature for 15 min, without braking
4) Recover parasites from the 35/65% Percoll interface and transfer it to a 15-ml disposable Falcon tube.
5) Add 10 volumes of incomplete culture medium drop by drop to the recovered parasites, gently shaking after each addition.
6) Centrifuge cells at 2,000 r.p.m. (~500g) for 5 min at room temperature and discard the supernatant.
7) Wash once more with 10 volumes of incomplete culture medium by centrifugation at 2,000 r.p.m. (~500g) for 5 min at room temperature and remove the supernatant.
8) Resuspend parasitized RBCs with 1 ml of complete culture medium.

Culture Conditions of Isolated Parasites

- 5% hematocrit and < 5 % parasitemia
- RPMI Media with 10 % FBS and no antibiotics
- 25 mm^2 petri dishes
- O_2 depleted candlejar
- 37 °C and 100 % humidity

Appendix B: Chlorambucil-Annexin Conjugate

Cytotoxicity Assay

MTT Cytotoxicity Assay (P388 or L1210 Cell Lines)

MTT is a yellow tetrazolium dye that turns purple when it is reduced to an insoluble formazan. This reduction is carried out by oxidoreductase enzymes that are dependent on NADH or NADPH inside cells. The level of active oxidoreductase enzymes is reflective of the cellular metabolic activity. Assays of cellular metabolic activity can be used to assay cell health. After solubilizing the formazan produced from a cell, the absorbance can be measured and compared to the absorbance of formazan in a control solution to determine if cellular metabolic activity has increased or decreased. The MTT assay is influenced by the growth phase of the cells and variation of metabolic activity amongst different cell types. Cell count should be taken during log phase. This protocol is for use with 24 or 96-well plates.

Protocol

1) Harvest 5 million cells from culture and dilute to a total of 25 mL with media.
2) Seed each well of a 24 well plate with 1 mL of media containing 200,000 cells

3) Allow cells to rest for at least 1-2 hours.

4) Treat groups according to experimental protocol.

5) In this experiment you will add 100 uL of the Chlorambucil-DMSO per well

6) Incubate cells with chosen treatment for 20 hours.

7) Add 100 uL of MTT solution to each well

8) Incubate cells with MTT for 2-4 hours to allow dye uptake.

9) Transfer contents each well to a microcentrifuge tube.

10) Centrifuge cells at 1000 RCF (not RPM) for 5 minutes

11) Discard supernatant in sink by gently flicking vials

12) Add 1 mL of DMSO to each vial lysing cells and solubilizing the MTT.

13) Transfer 100 uL of solution from each well to a clear 96 well plate.

14) Read the absorbance immediately at 540nm.

Supplies

- 5 million cells
- DMEM with 10% horse Serum and 1 % Anti/Anti
- DMSO
- MTT Stock Solution (62.5 mg of MTT:25 mL of PBS)
- 24 well plate
- Chlorambucil Dissolved in DMSO

Synthesis of ANXA5-CMB

1) Dissolve 100 µg of chlorambucil in 50 µL of 12 M HCL*(Chlorambucil is insoluble at neutral pH, but dissolves readily at pHs below 5. However, chlorambucil is unstable in acidic solutions and should not be stored for long periods of time in acidic solutions.)*

2) Dilute the mixture in 1 mL of phosphate buffer*(This provides a larger working volume of chlorambucil to continue downstream production.)*

3) Add 10 mg of EDC*(The EDC will bind the carboxylic groups of chlorambucil increasing their chemical reactivity towards primary amines.)*

4) Add 7 mg of suflo-NHS *(Sulfo-NHS stabilizes the EDC activated carboxylic groups, increasing the efficiency of the chlorambucil-annexin reaction.)*

5) Stir vigorously for 15 minutes

6) Add 2 µL of β-mercaptoethanol *(B-mercaptoethanol neutralizes the excess EDC and NHS preventing their interference in downstream reactions.)*

7) Immediately titrate the solution to a pH of 7.4 *(Raising the pH stabilizes the sensitive chlorambucil functional groups.)*

8) Add 2.33 mL of a 1 mg/ml solution of annexin in phosphate buffer *(The annexin is kept at a low concentration to prevent precipitation and crosslinking. The dilute mixture also serves to further neutralize some of the acid from step.)*

9) Stir gently for 12 hours

10) Centrifuge for 10 minutes at 7,000 rcf*(Chlorambucil is not stable in neutral pH solutions and will precipitate. The precipitate is easily removed by centrifugation.*

11) Retain the supernatant and discard the pellet

12) Dialyze the supernatant against 2 L of phosphate buffered saline for 8 hours. *(This step removes the rest of the unbound chlorambucil as well as other upstream contaminants such as β-mercaptoethanol.)*

13) Filter the dialysate using a 0.2 µm filter

14) Immediately flash freeze under liquid nitrogen and store at -80 °C until immediately before use.

Spectroscopy CMB

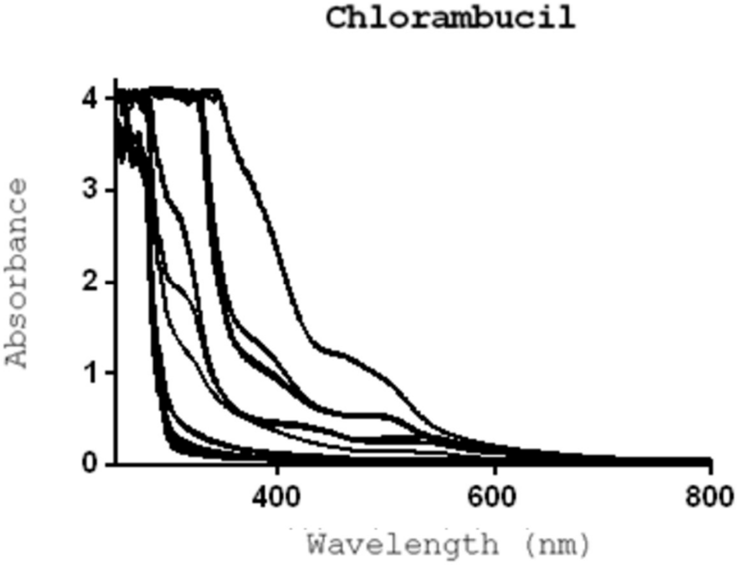

Figure 76: Chlorambucil absorbance.
Chlorambucil has strong absorbance at UV wavelengths. Pictured above are the spectra for serial dilutions of chlorambucil. ([Chlorambucil]$_{\text{starting}}$ = 10 mg/ml; serial dilutions by half).

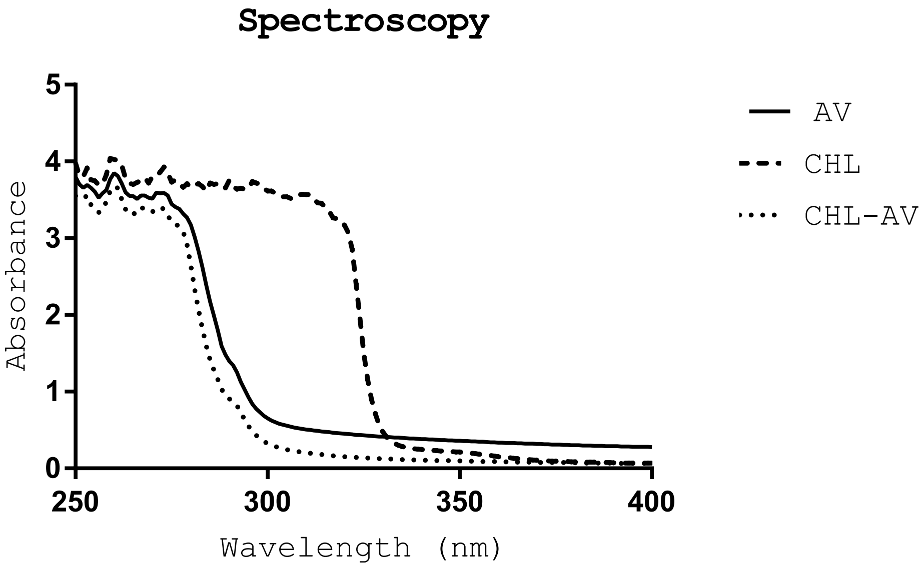

Figure 77: Absorption spectroscopic detection of CHMB.
Despite strong absorbance peaks in the UV range, an unknown concentration of chlorambucil can not be determined with absorbance spectroscopy in samples containing protein. When chlorambucil is in the presence of protein the absorption spectra of the chlorambucil – protein conjugate is dominated by that of the aromatic amino acids of the protein (λ:280).

Appendix C: Photothermal Therapy Combined with Checkpoint Inhibition

Tumor Treatment Timelines

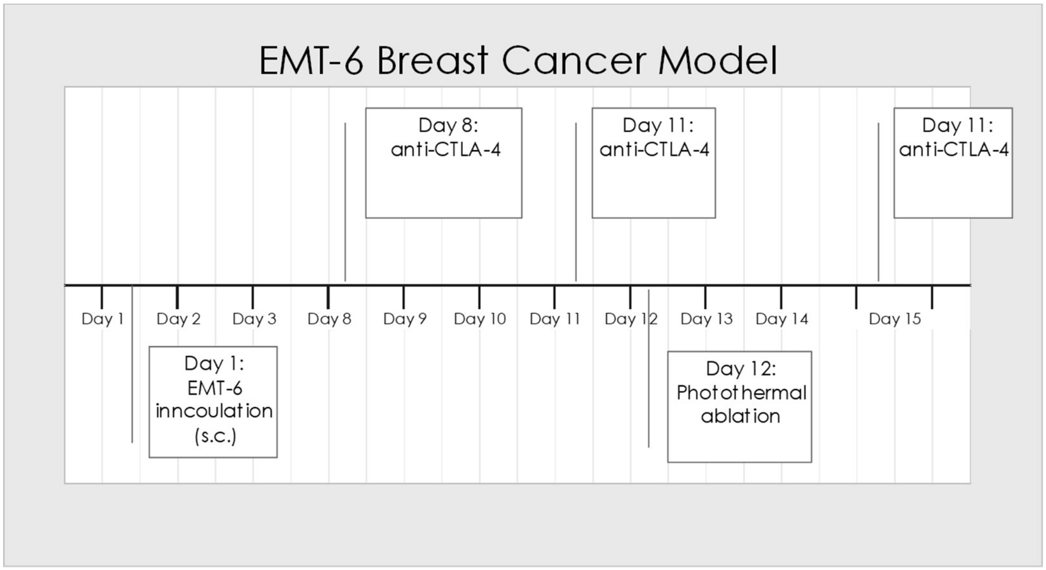

Figure 78: EMT6 breast cancer model timeline.

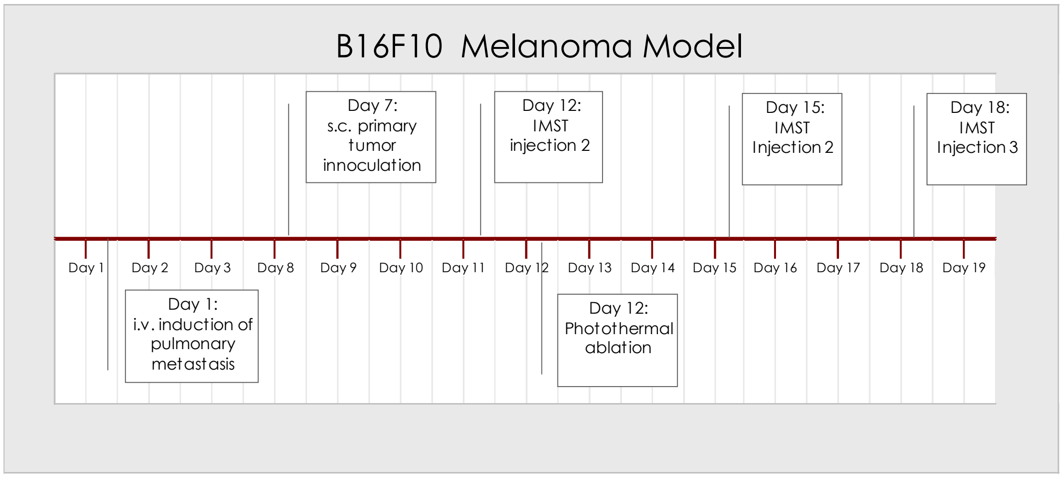

Figure 79: B16F10 Melanoma model timeline.

SWCNT Standard

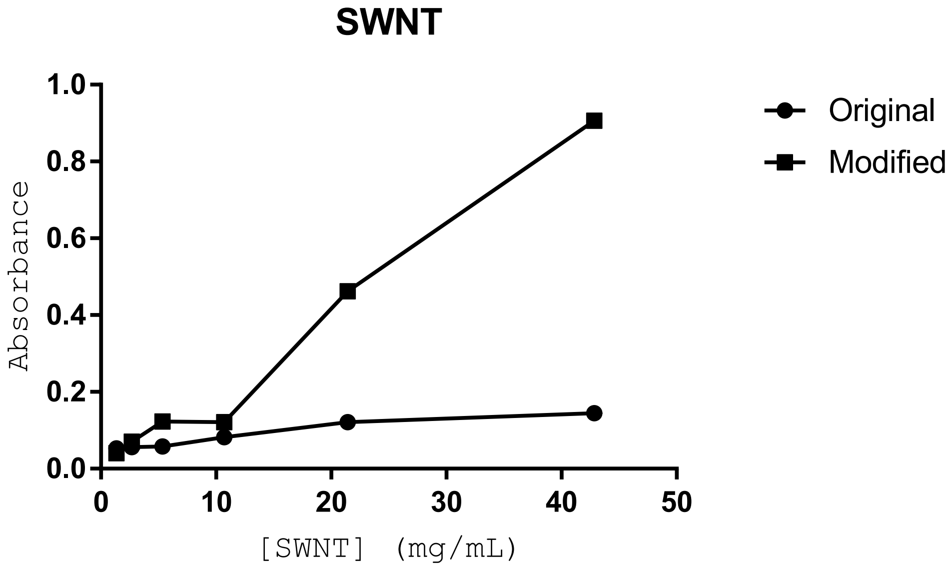

Figure 80: The quantification of SWCNT during the synthesis of SWCNT-ANXA5.
We observed that additional sonication resulted in unbundling of SWCNT aggregates in solutions increasing absorbance. A modified procedure resulted in an updated SWCNT standard.

B16F10 Tumor Model

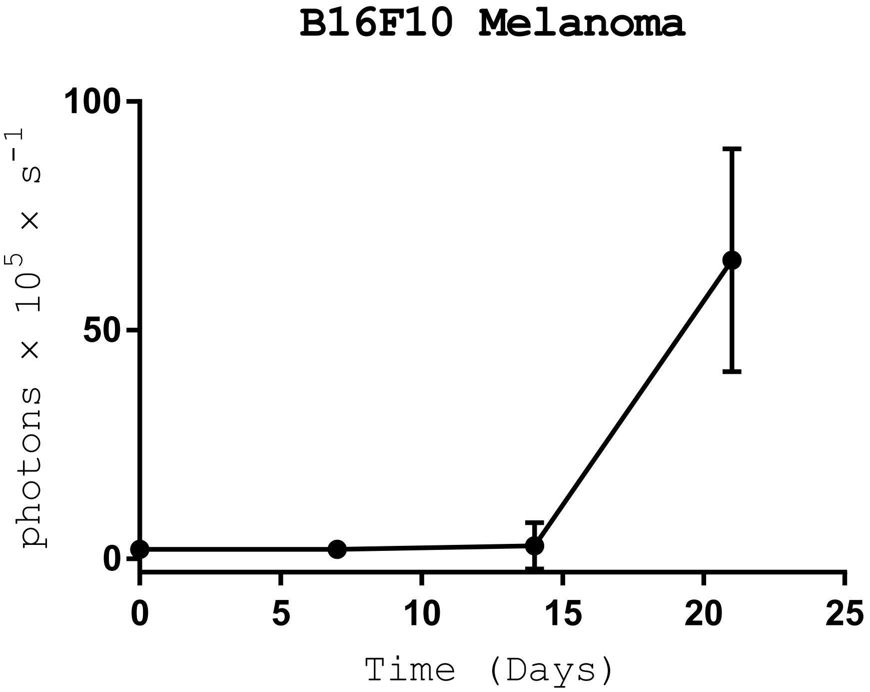

Figure 81: In Vivo detection of B16F10 tumor metastasis by luciferase assay following i.v. induction of lung metastasis in C57 mice (n = 3).

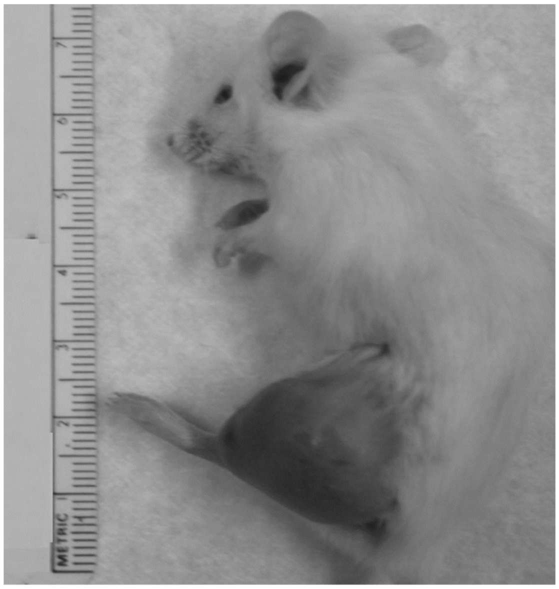

Figure 82: Balb/cj mouse bearing a B16F10 tumor 16 days following a s.c. inoculation.

Survey of Immunostimulants in B16F10

We investigated the interaction between photothermal therapy and tumor metastasis. Using fluorescent B16F10-luceferase we artificially induced lung metastases by i.v. inoculation with 10^6 tumor cells. The growth of lung metastases was tracked by 2D optical tomography imaging (Figure 93).

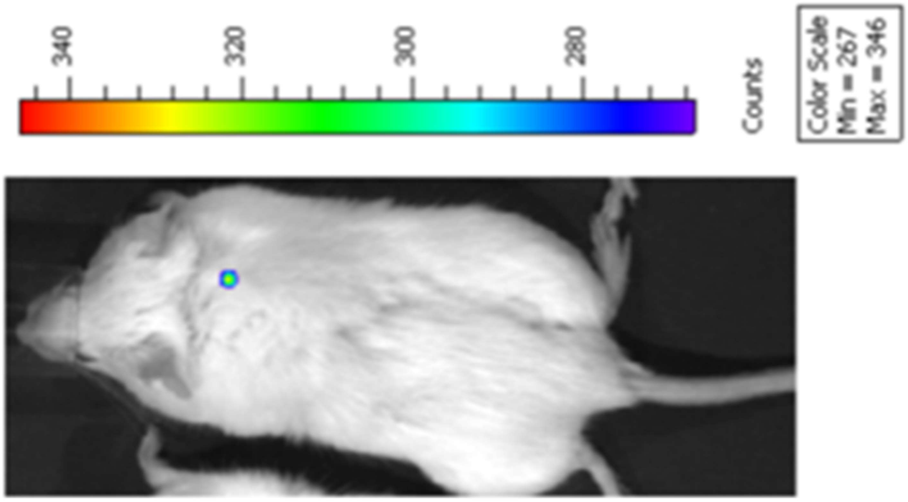

Figure 83: The metastatic B16F10-lucerferase lung tumor burden of mice was measured with 2D optical tomography imaging.

We monitored lung tumor burden and survival in mice in mice (n = 5) following SWCNT-ANXA5 targeted photothermal ablation. Surprisingly, we observed no increase in survival when mice received photothermal ablation or anti-CTLA-4 checkpoint inhibition (Figure 84).

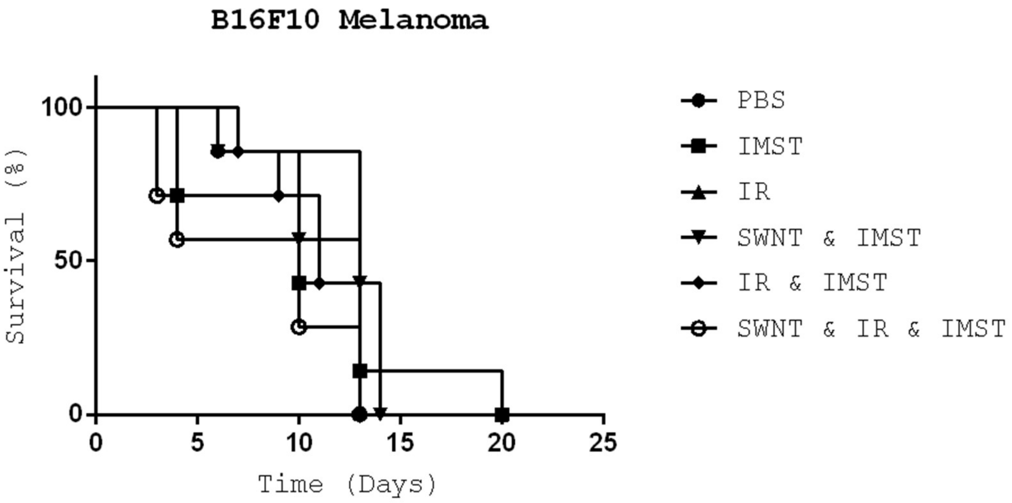

Figure 84: Survival of B16F10 tumor bearing mice.

Examination of the lung tumor burden of select groups by 2D optical tomography imaging 3 weeks following the induction of pulmonary metastasis revealed that both photothermal therapy and anti-CTLA-4 blockade increased relative lung tumor burden.

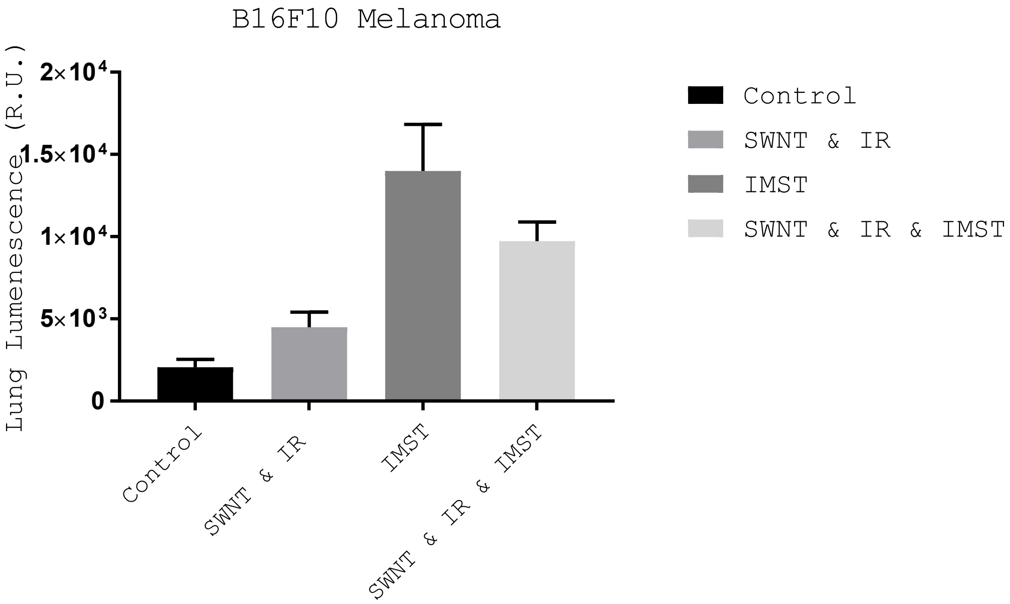

Figure 85: The relative tumor burden of mice bearing B16F10 metastatic lung tumors was determined by 2D optical tomography imaging. Data is presented as the mean ± SE (n = 5).

Further efforts employing alternative immunostimulants such as cyclophosphamide, anti-PD-1, or anti-CD-73 failed to substantially inhibit tumor growth as assayed by mouse weight, fluorescent lung tumor burden or survival (Figure 86, 87, and 88). We hypothesize that the rapid onset of mortality in the B16F10 modal hampered the effect of immunostimulation.

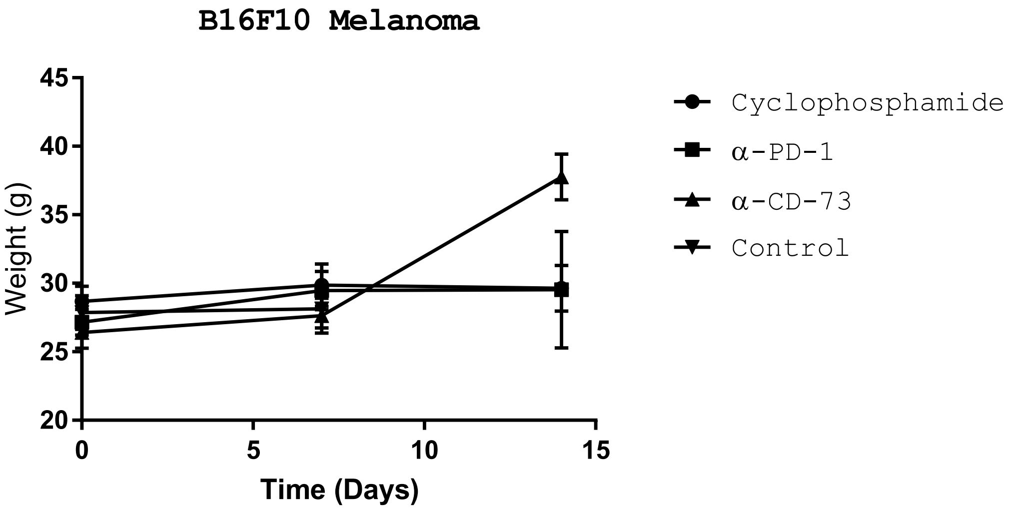

Figure 86: Mouse weight Data is presented as the mean ± SE (n = 7).

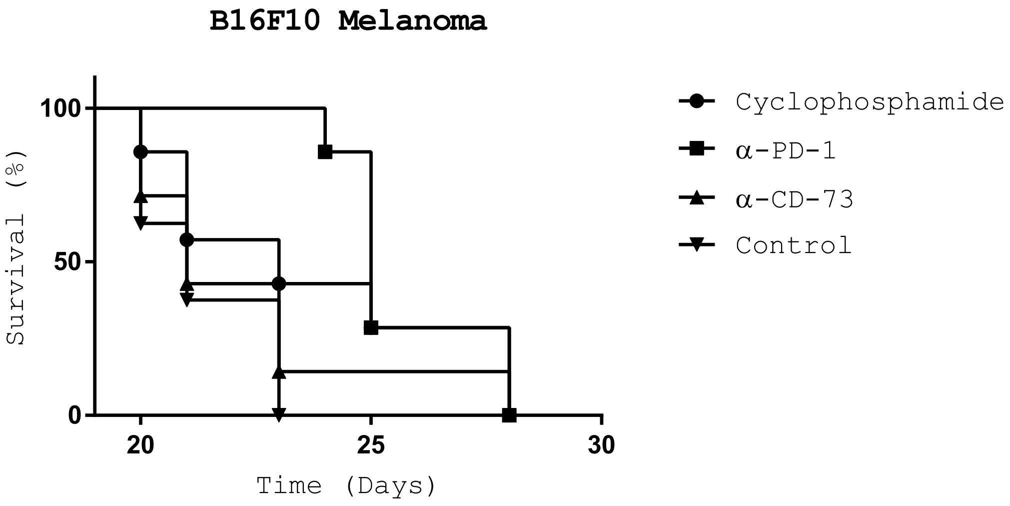

Figure 87: Survival of B16F10 tumor bearing mice. Data is presented as the mean ± SE (n = 7).

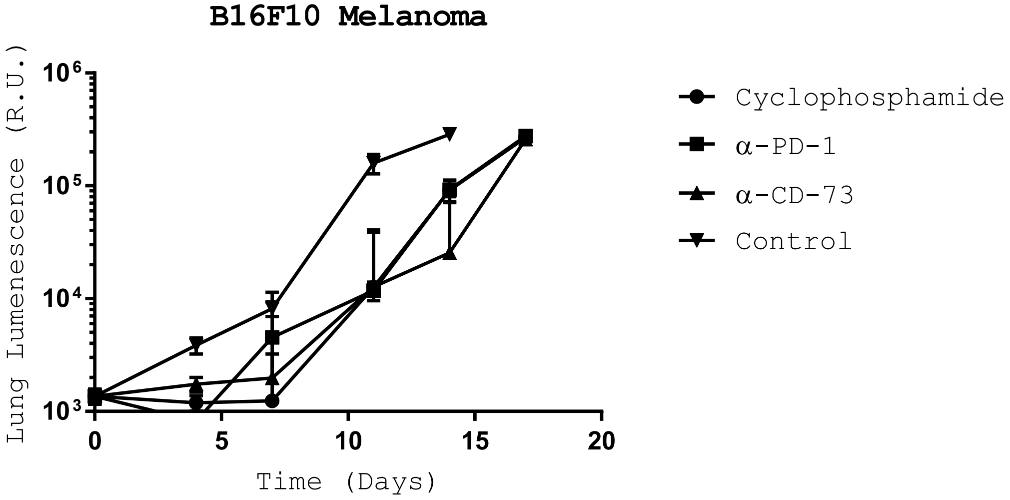

Figure 88: Lung tumor burden. Data is presented as the mean ± SE (n = 7).

Biodistribution Calculation

$$\% ID = AUC_{Fl_{758}}\ x\ \frac{1 \frac{mg}{L} SWCNT}{4.62\ FL_{758}} * \frac{\left[M_{Sample}\ x\ \frac{1\ mL}{1.045\ g}\ x\ \frac{1\ L}{1000\ mL}\right]}{30\ x\ 10^{-3}\ mg\ SWCNT}\ x\ \frac{1}{Dilution\ Factor}\ x\ 100$$

Conjugation of DSPE-PEG-Maleimide linker to Annexin A5 Protein

Purpose: Use DSPE-PEG-Maleimide linker to functionalize SWCNTs with Annexin V protein

1. Prepare 1% SDS solution.
    a. Prepare 1% SDS stock.
        i. .5g SDS in 50mL DI water.
2. Prepare SWCNT suspensions.(2 hours and 45 minutes→store in the fridge)
    a. Sonicate the SWCNT solution for 30 minutes. (6mg SWCNT in 5 ml 1% SDS)
        a. Use SG65i from 5/13/2013.

b. Make solution in a glass vial.
c. Sonicate a maximum. (difficulty turning on/make sure probe does not touch the glass vial)
d. Place vial in water bath to prevent it from overheating.

b. Centrifuge the SWCNT solution for 30min at 13000rpm.
   a. Store supernatant.
   b. Aggregates will drop to the bottom of solution.

c. Transfer SWCNTs supernatant solution to new tube and repeat steps a and b.

3. Dissolve DSPE-PEG-Maleimide linker (MW 4368 Da) at 1.5 mg/ml in 1% SDS.
   a. Dissolve 1.5mg of linker in 1mL 1% SDS.
   b. Store linker at -20˚C under nitrogen.
4. Add 1 ml of linker to 5 ml of SWCNT suspension.
5. Mix at RT for 30 min with gentle shaking on shaker with stir bar.
6. Dialyze SWCNT-linker for 8 hr against 2 L of DI water. Change the dialysate after 4 hr. Use a 2 kD dialysis membrane.
   a. Use green dialysis clips.
7. Reconstitute 5 mg of annexin a protein with 1 ml of DI water.
   a. Conduct a Bradford Assay to confirm protein concentration.
      i. Mix 5uL of protein and 250uL of Bradford reagent in 96-well plate with clear bottom. Run blank well with DI water. (use aliquot)
      ii. Shake for 30 seconds and incubate at room temperature for 10 minutes.
      iii. Read absorbance at 595nm. Absorbance should be between 0.3-1.
      iv. Use standard curve equation to determine concentration.
8. Take 2 ml of SWCNT-linker suspension and add 5mg of annexin A5 to it. (annexin:linker molar ratio= 1.05:1)
9. Mix the SWCNT-linker and annexin A5 at RT for 2 hr with gentle shaking on shaker (3 ml total volume).
10. Block unreacted linker sites with 0.166 mg of L-cysteine and mix at RT for 1 hr with gentle shaking. (The molar ration of L-cys:linker is 4:1) For ease, add 33.2µl of a 5 mg/ml solution of L-Cysteine.

11. Dialyze the SWCNT-annexin A5 conjugate for 8 hr against 2 L of 20 mM sodium phosphate buffer at pH 7.4 (5.678 g of sodium phosphate/2L DI water). Change the dialysate after 4 hr. Use a 100kD dialysis membrane. Do not allow this dialysis to go to long—change the dialysate at 3:45 and remove from dialysis at 7:30.
12. Centrifuge the resulting SWCNT-annexin A5 conjugate at 15,680g for 1 hr to remove aggregates.
    a. Keep supernatant.
13. Measure the SWCNT and protein concentrations.
    a. Run Bradford assay for protein concentration.
    b. Measure SWCNT absorbance at 800nm of spec.
14. Store conjugate at 4˚C.

Flow Cytometry Staining

Tissue Collection:

1. Euthanize animal with CO2 inhalation.

2. Collect blood and place in heparin tube. Spin tube to separate plasma from blood and store at -20°C.

3. Collect lymph node and spleen and place in 5 ml of cold RPMI-1640 medium. Place samples on ice and transport to Norman.

4. Collect remaining tissue (liver, kidney, heart, lungs, intestine, and tumor) place in 10% NBF.

Flow Cytomery Buffer Preparation:

1. Flow Cytometry Staining Buffer (SB): 1X PBS + 0.5% BSA + 0.05% Sodium Azide.
2. Foxp3 Fixation/Permeabilization working solution: Dilute the Fixation/Permeabilization Concentrate (1 part) with Fixation/Permeabilization Diluent (3 parts). You will need 1 mL of the Fixation/Permeabilization working solution for each sample, if staining in tubes.
3. Permeabilization Buffer: Dilute the 10X concentrate with distilled water prior to use. All following procedures with cells should be conducted on ice.

Flow Cytometry Sample Preparation:

1. Tease apart tissue (lymph node and spleen) into a single-cell suspension by pressing with the plunger of a 3-mL syringe with 1 ml of SB into a petri dish. Wash plunger 2X with 1 ml SB each time.
2. Place a cell strainer on top of a 50-ml conical tube. Pass cells from the petri culture dish through the cell strainer to eliminate clumps and debris. Wash petri dish and stainer 2X with 1 ml SB each time.
3. Centrifuge cell suspension at 300-400g for 4-5 min at 2-8°C. Discard the supernatant.

4. Resuspend the cell pellet in a 1 ml volume of SB and perform a cell count and viability analysis. a. Add 10 µl of typan blue + 10 µl of diluted cell suspension (1:100 dilution) and count live and total cells.

5. Centrifuge cells as in Step 3 and resuspend in appropriate volume of SB so that the final cell concentration is 1 x 107 cells ml-1.

Flow Cytometry Staining

1. Add 100 µL of cell stock to a 2 mL microvial.
2. Spin primary antibody tubes to pull solution to bottom of vial.
3. Stock antibody cocktail
4. Add stock antibody cocktail (Table 1) and bring final volume to 50 µl with SB.
5. Incubate for at least 60 minutes at 2-8°C or on ice. Protect from light.
6. Wash the cells by adding Flow Cytometry Staining Buffer. Use 2 ml tube-1. Centrifuge at 400-600g for 5 min at room temperature. Discard supernatant.
7. Repeat previous wash step.
8. Add 1 ml of Fixation/Permeabilization working solution to each tube and pulse vortex.
9. Incubate for 60 min at room temperature. Protect samples from light.
10. Wash the cells by adding 1X Permeabilization Buffer to each tube. Use 1 ml tube-1. Centrifuge at 400-600g for 5 min at room temperature. Discard

supernatant.

11. Repeat previous wash step.

12. Resuspend pellet in 100 µl of 1X Permeabilization Buffer. This is typically the residual volume after decanting.

13. Block with 2% BSA by adding 2 µl directly to the cells.

14. Incubate for 15 min at room temperature.

15. Without washing, add either 2.5 µL of PE-Foxp3 antibody or SB (Table 1) to cells.

16. Incubate for at least 30 minutes at room temperature. Protect samples from light.

17. Wash the cells by adding 1X Permeabilization Buffer to each tube. Use 1 ml tube-1. Centrifuge at 400-600g for 5 min at room temperature. Discard supernatant.

18. Repeat previous wash step.

19. Resuspend cells in an appropriate volume of Flow Cytometry Staining Buffer.

20. Analyze samples by flow cytometry.

Flow Cytometry Repeat Study

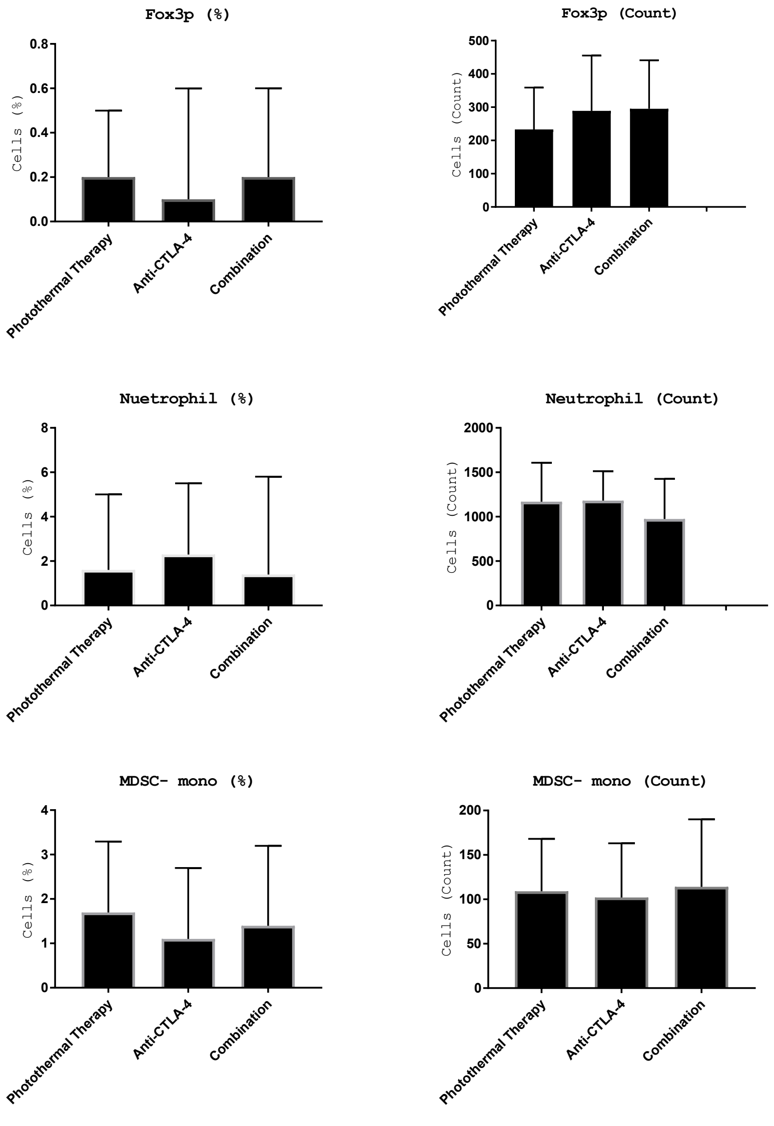

Figure 89: Repeat Flow Cytometry Experiments. Data is presented as the mean ± SE (n = 3).

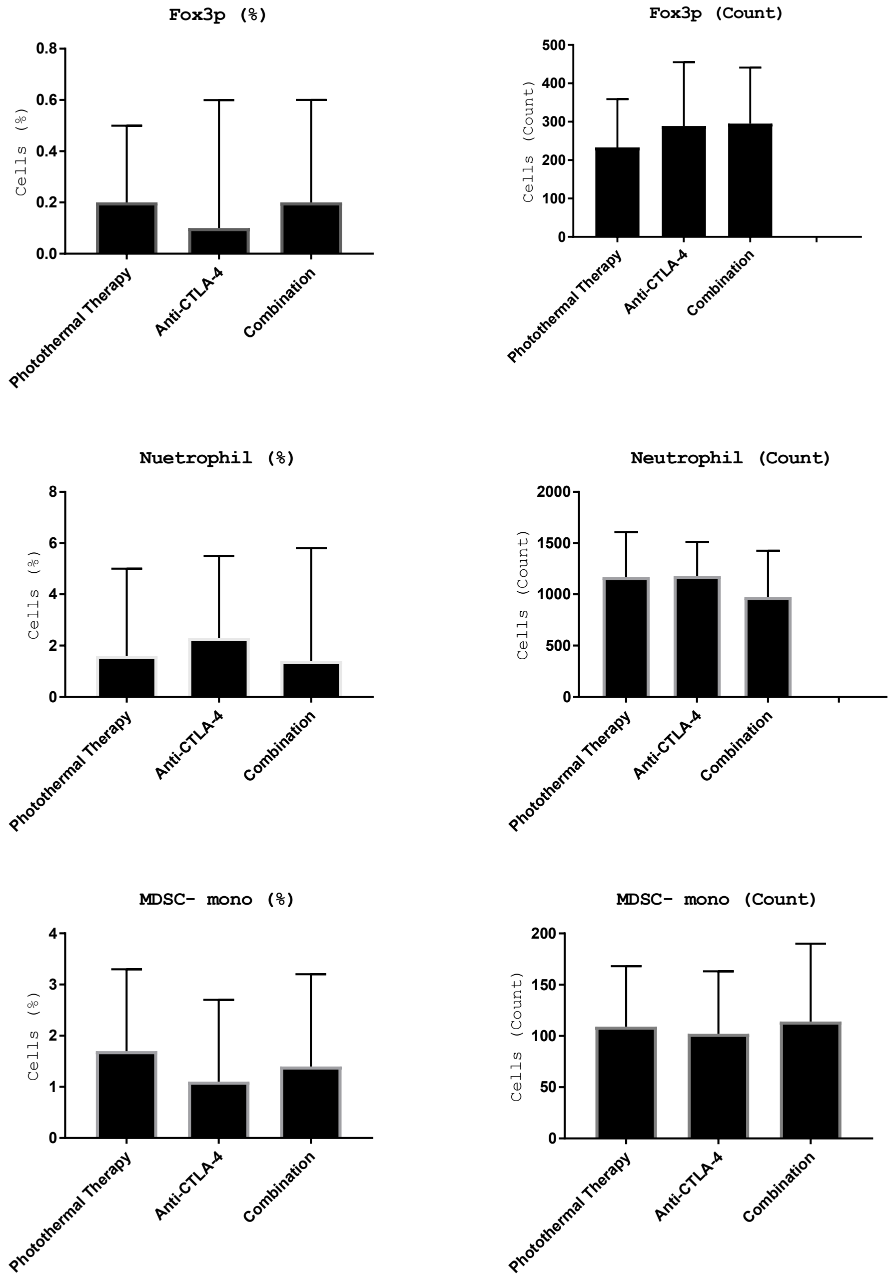

Fox3p (%)

Fox3p (Count)

Nuetrophil (%)

Neutrophil (Count)

MDSC- mono (%)

MDSC- mono (Count)

Figure 90: Repeat flow cytometry experiments. Data is presented as the mean ± SE (n = 3).

Appendix D: Characterization of SWCNTs

Fluorescent Spectroscopy

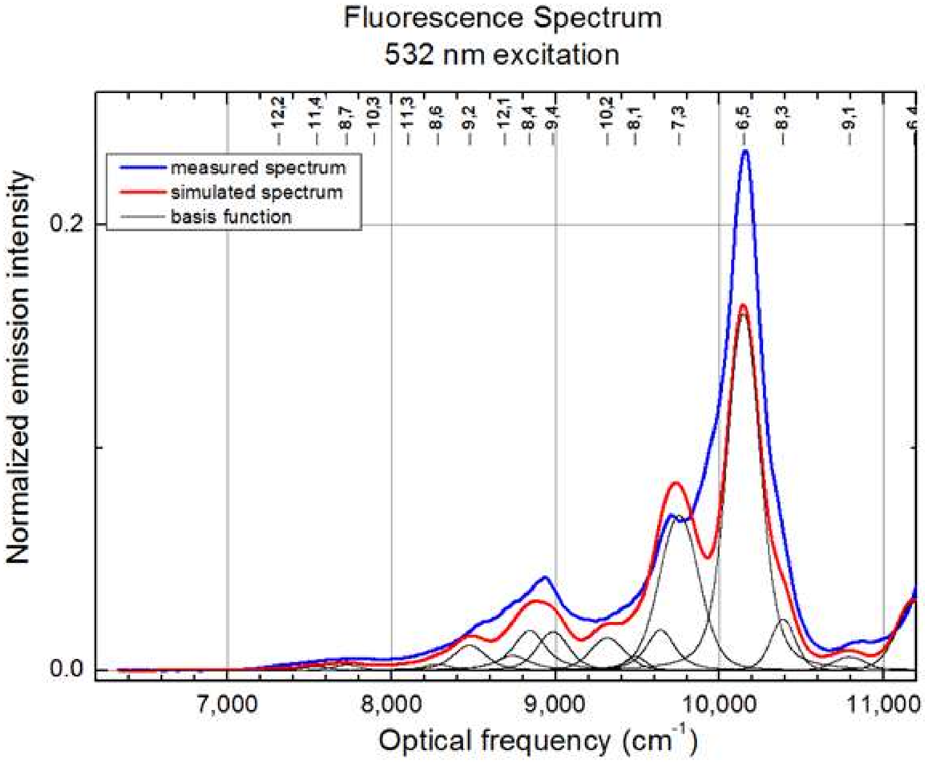

Figure 91: The emission spectra of SG65i at 532 nm showing the chiral specific peaks (basis function) and their respective chirality.

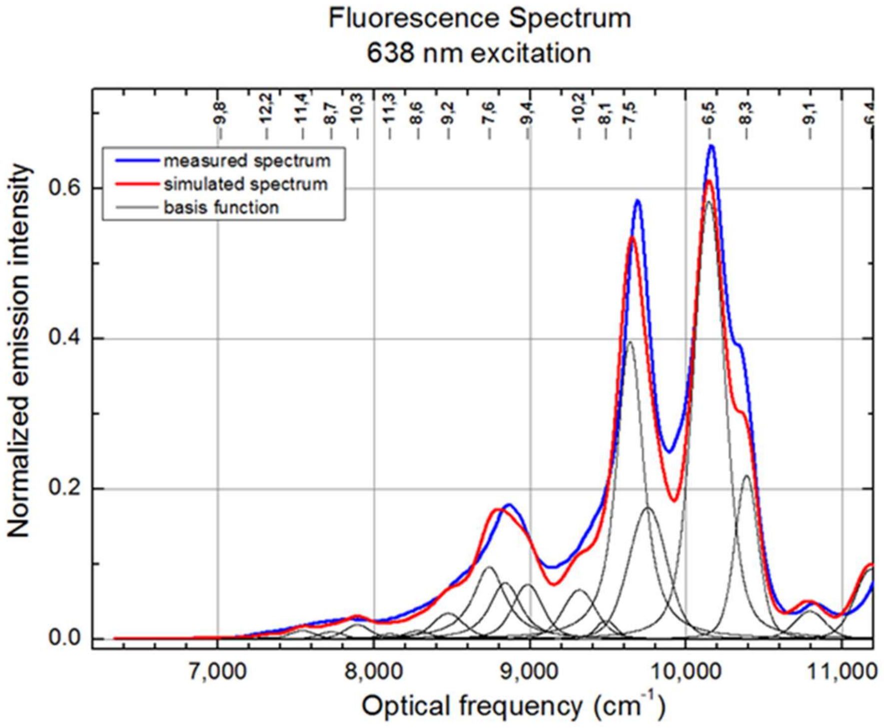

Figure 92: The emission spectra of SG65i at 638 nm showing the chiral specific peaks (basis function) and their respective chirality.

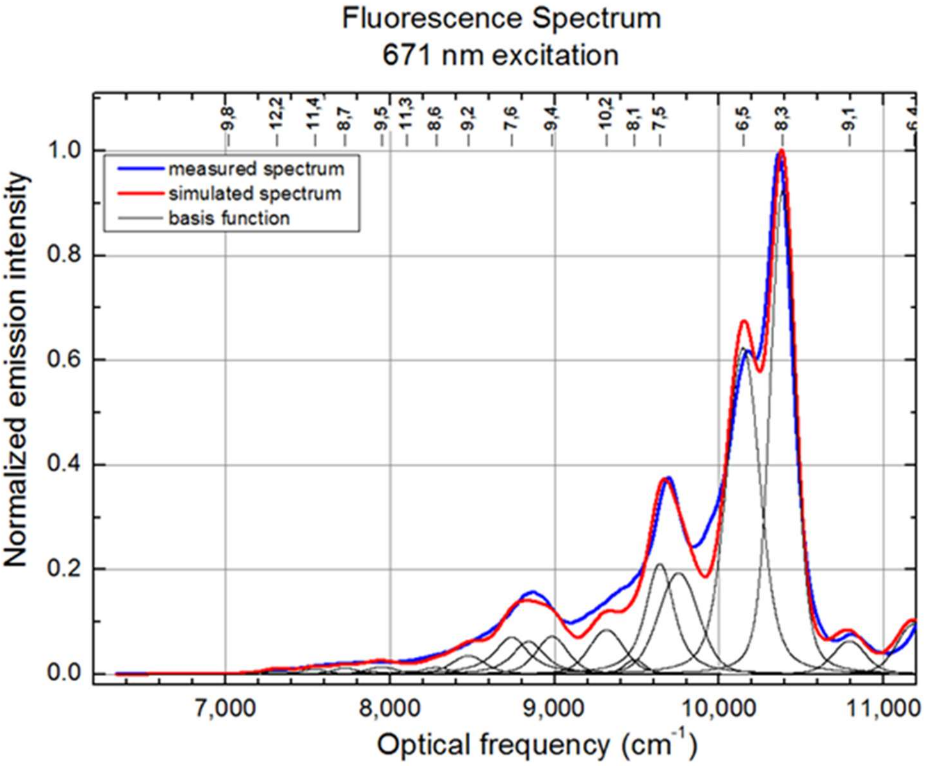

Figure 93: The emission spectra of SG65i at 671 nm showing the chiral specific peaks (basis function) and their respective chirality.

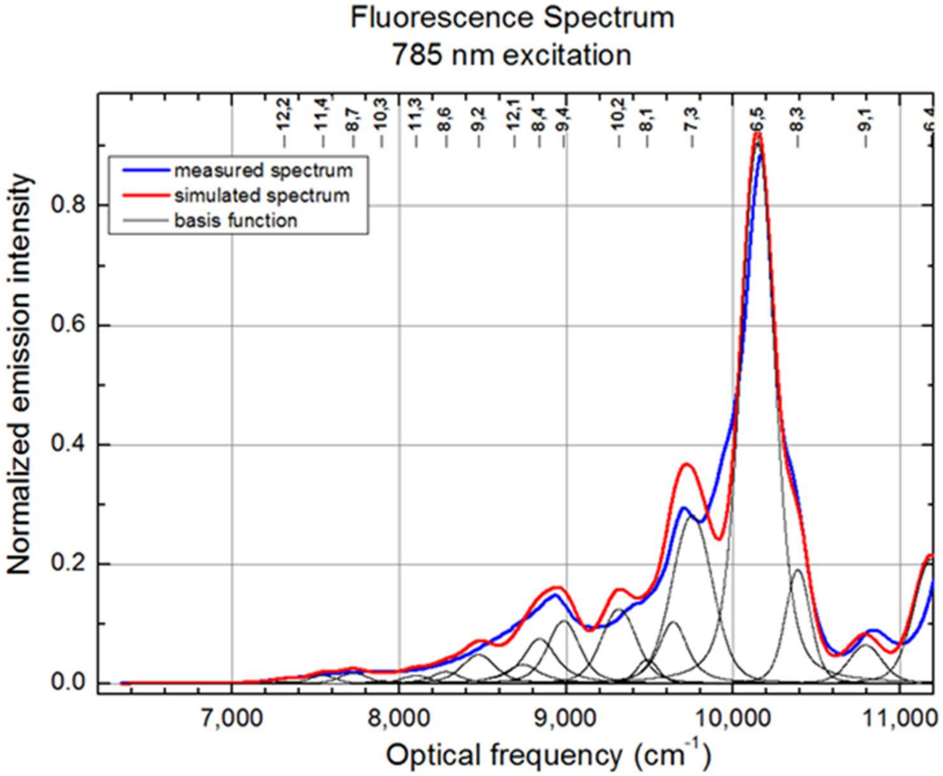

Figure 94: The emission spectra of SG65i at 785 nm showing the chiral specific peaks (basis function) and their respective chirality.

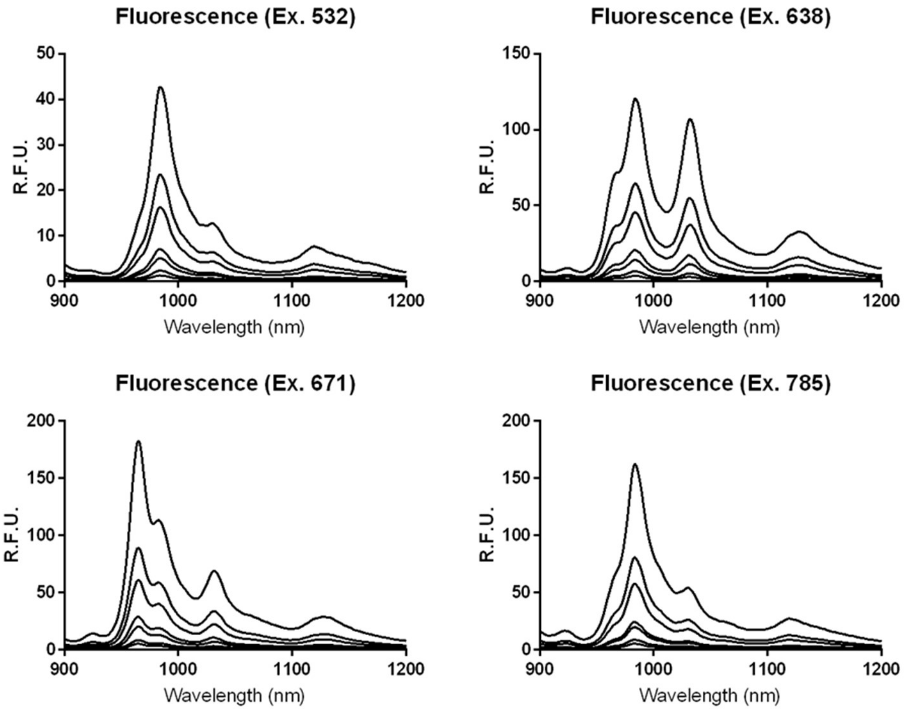

Figure 95: The emission spectra and standards of SG65i under different excitation conditions.

Fluorescent Standards

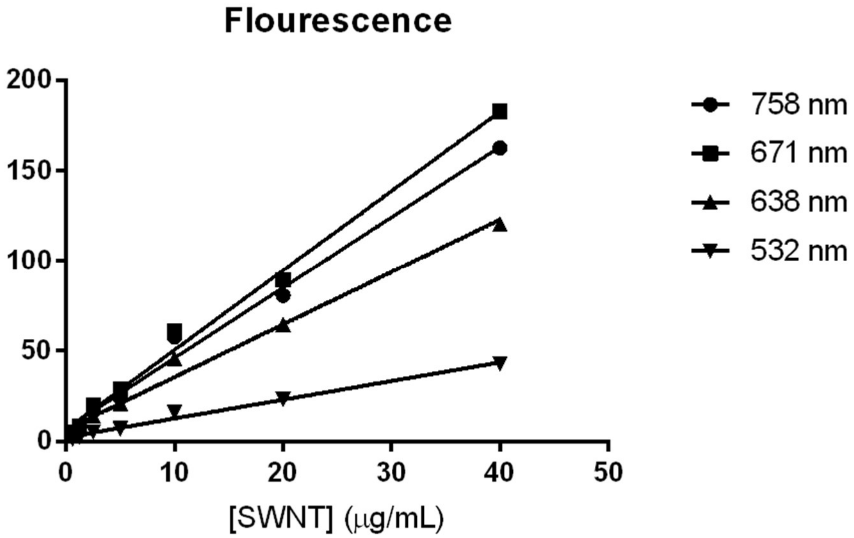

Figure 96: SWCNT fluorescent standards of samples measured at different excitation frequencies. All sample fluorescent measurements correspond to SWCNT 6,5 chirality emission with the exception of 671 and 638 nm which correspond to 8,3-SWCNT and 7,5-SWCNT chiral nanotubes respectively.

Absorption Spectroscopy

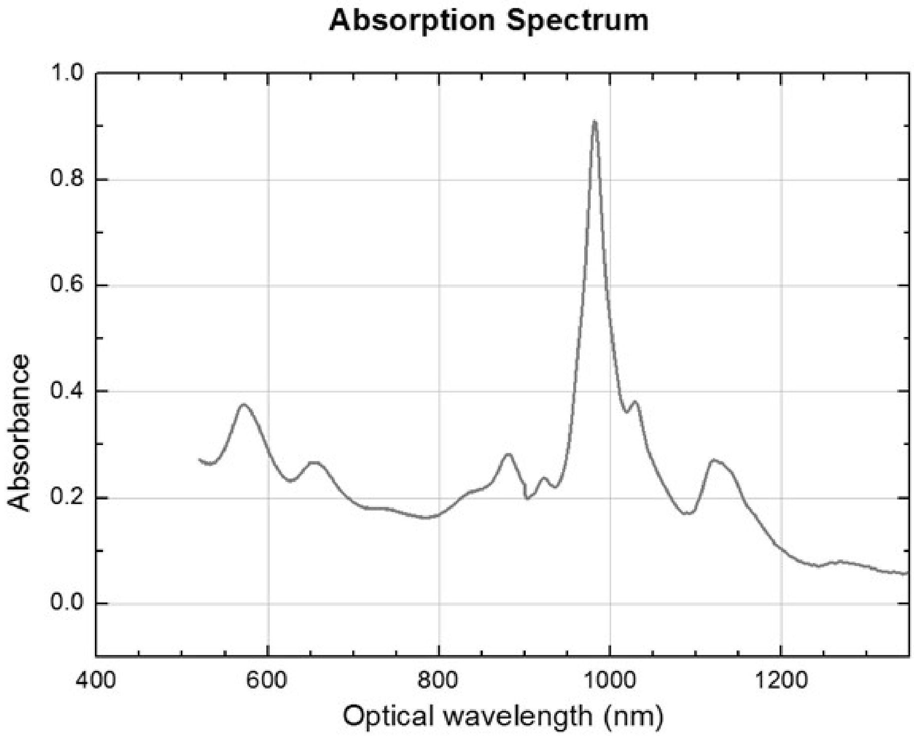

Figure 97: In non-biological samples the presence of SG65i SWCNT can be determined by absorbance spectroscopy.

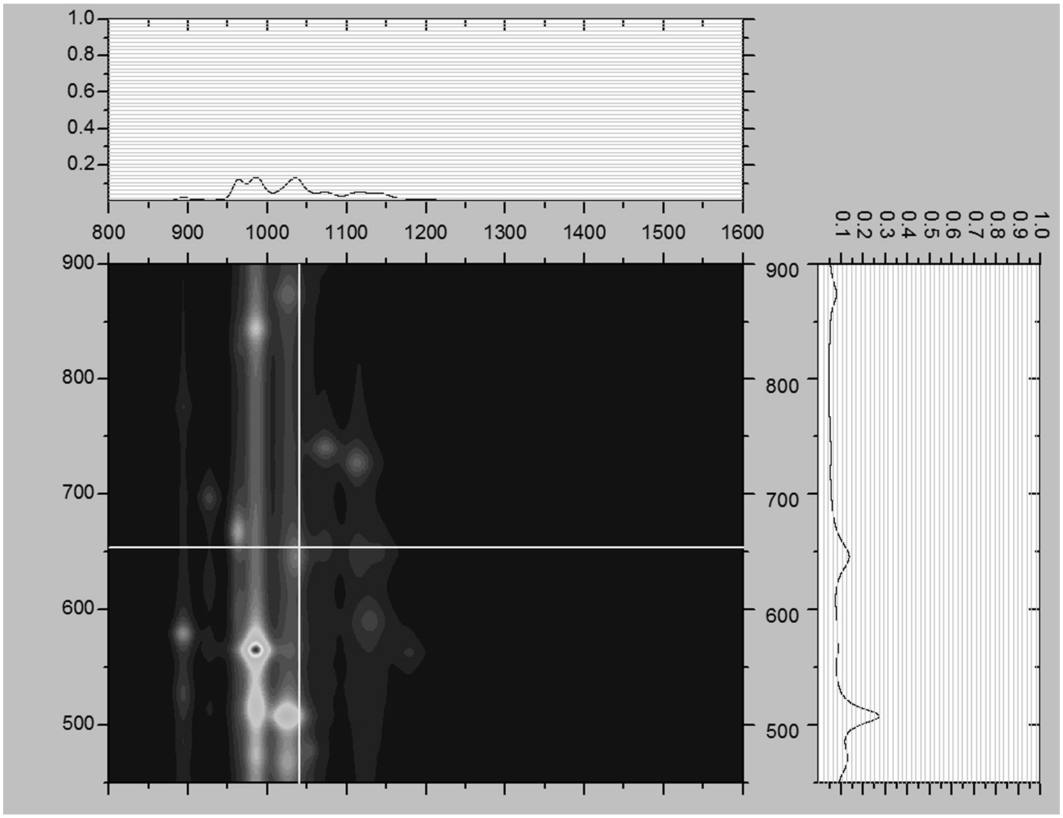

Figure 98: The fluorescent emission spectra of SG65i SWCNT showing characteristic patches of specific nanotube chirality.

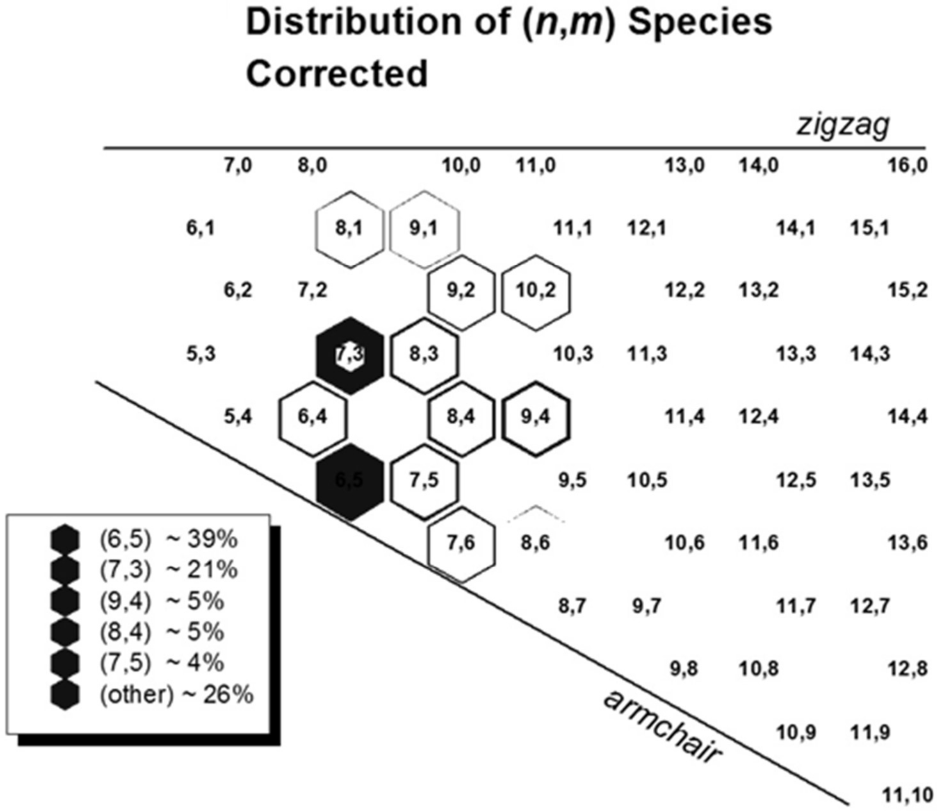

Figure 99: The chirality distribution of SG65i SWCNT as a function of (n,m) organization.

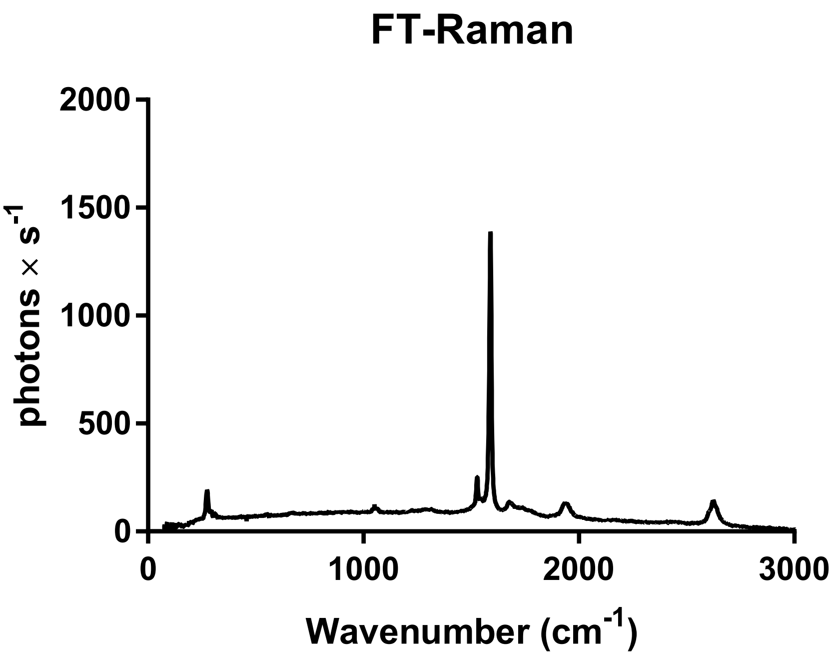

Figure 100: SWCNT (1590 cm^{-1}) can be detected in non-biological samples with FT-raman spectroscopy.

Size Distribution

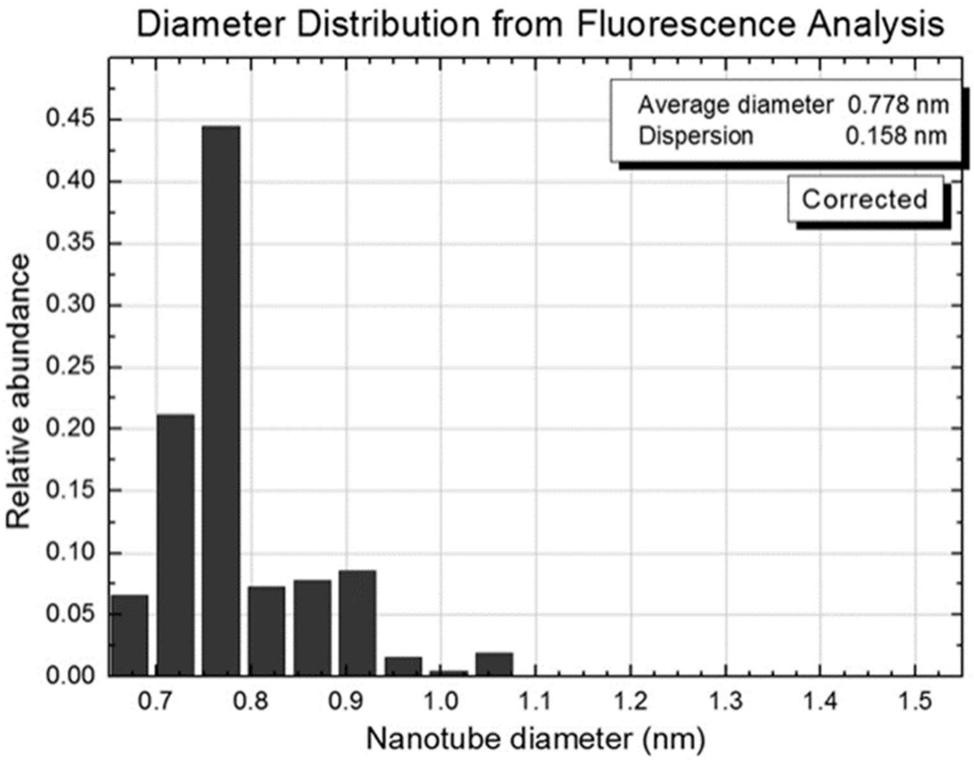

Figure 101: The diameter distribution of SG65i SWCNT was determined by comparative NIR-fluorescent spectroscopy.

TGMS-Composition

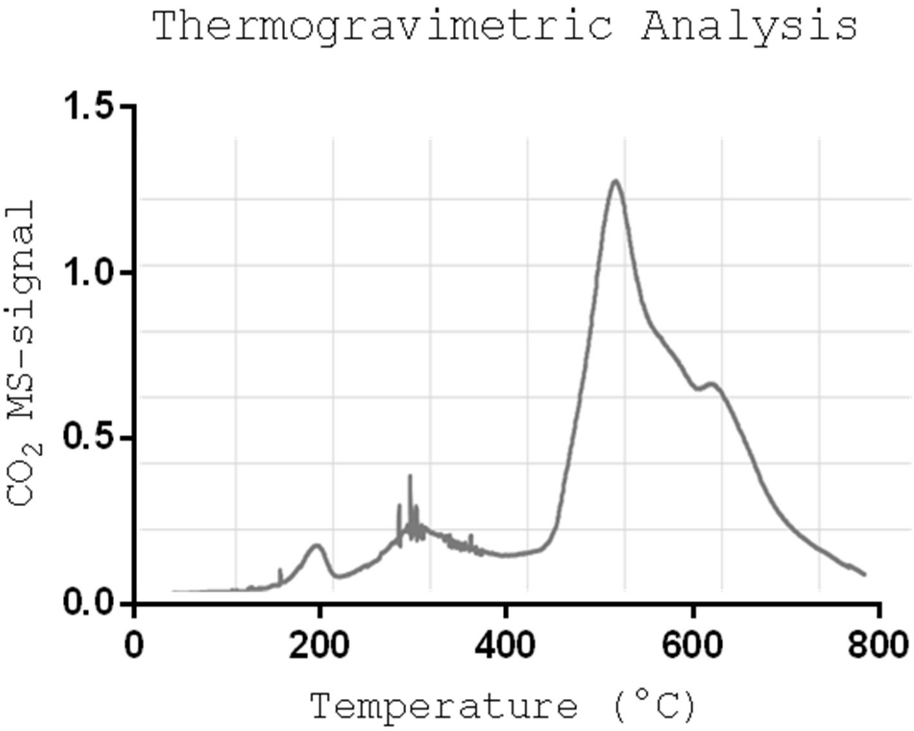

Figure 102: SWCNT can be detected in biological samples using thermogravimetric analysis. Samples of liver (100 mg) doped with SWCNT (10 µg) showed clear CO_2 emission peaks (500-600 °C) indicative of SWCNT.

on a microtiter plate reader (n = 3) between 230-260 was measured (Figure 60).

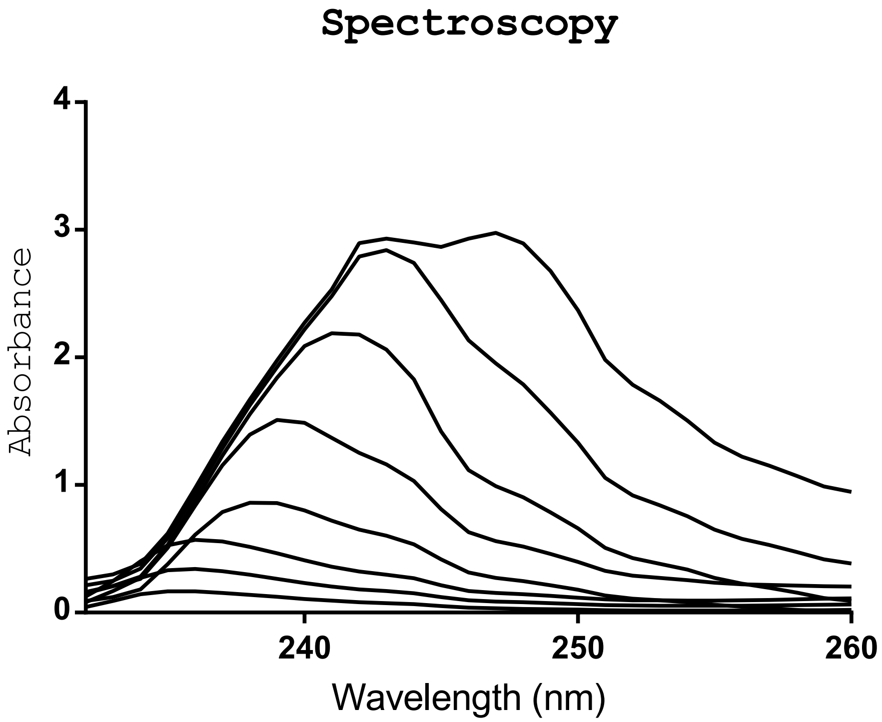

Figure 103: Carboplatin Absorbance. The absorbance spectra of carboplatin serial-half dilutions varies linearly with concentration. [Carboplatin]starting: 4.5 mg/mL)

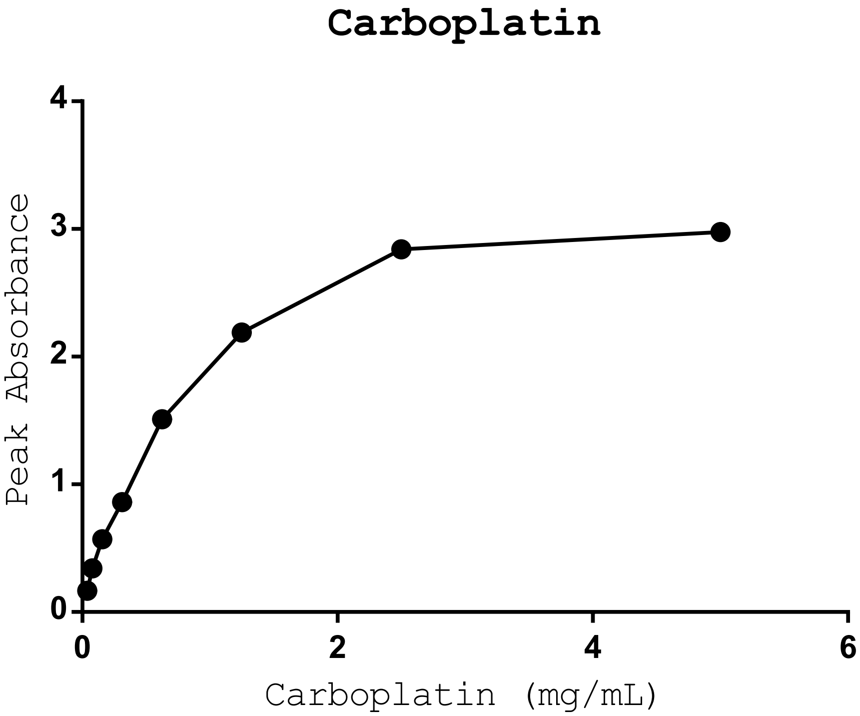

Figure 104: Carboplatin Standard.

Appendix G: SWCNT-DTX Conjugate Characterization

Detection of DTX from DTX-SWCNT

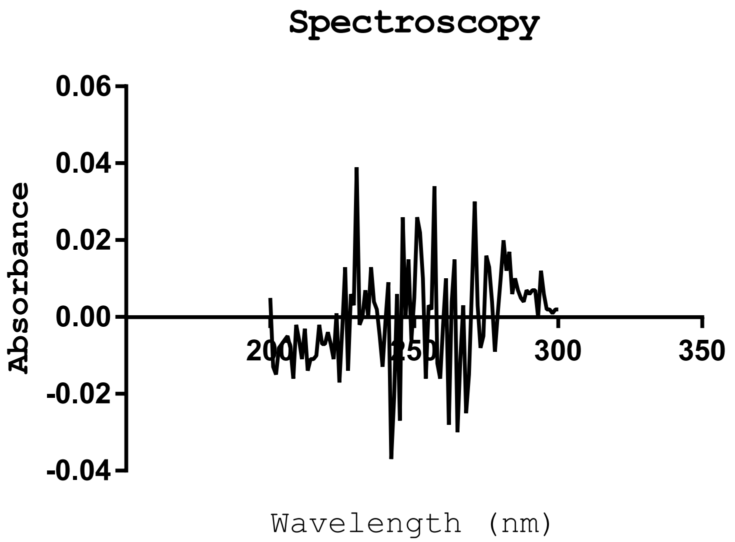

Figure 105: DTX as part of a DTX-SWCNT complex was not detected by absorbance spectroscopy.

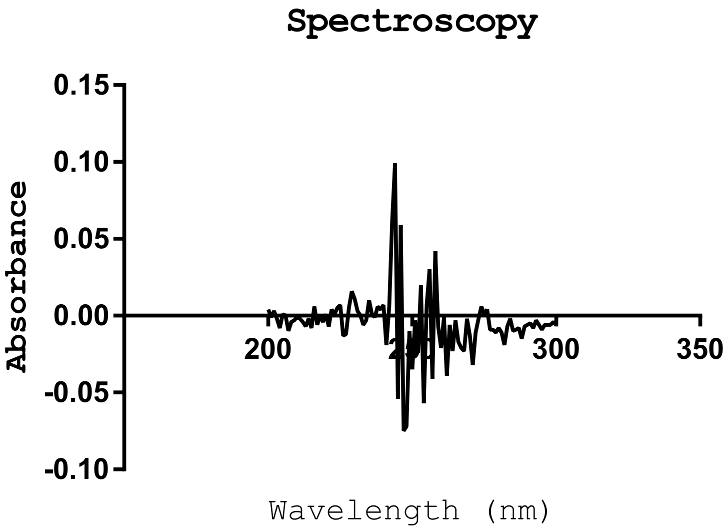

Figure 106: Acetonitrile isolation of DTX from DTX-SWCNT.

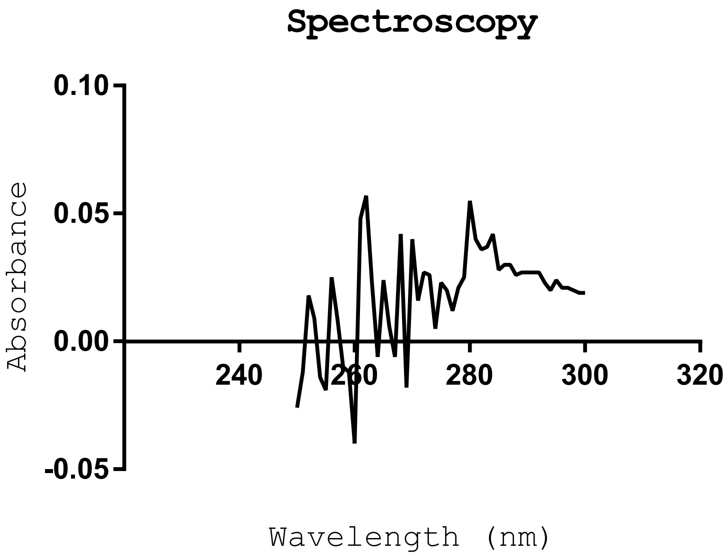

Figure 107: Ethanol isolation of DTX from DTX-ANXA5-SWCNT.

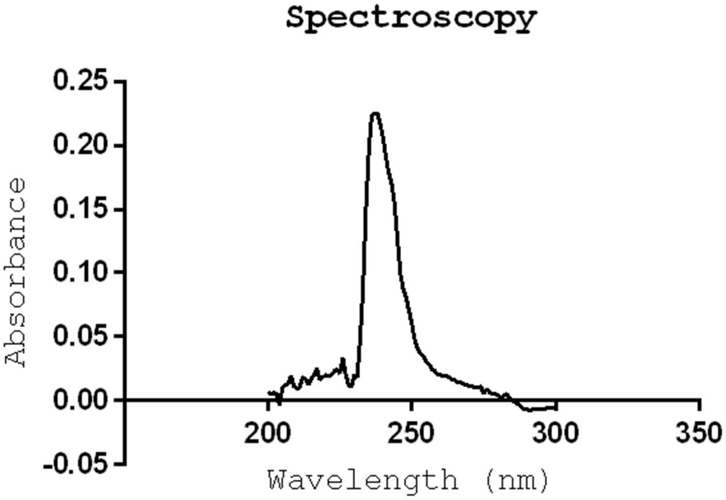

Figure 108: Methylene chloride extraction of DTX from DTX-SWCNT.

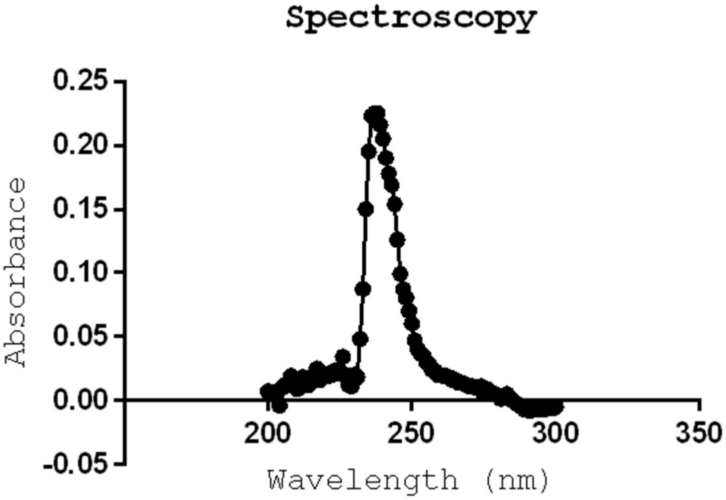

Figure 109: Extraction of DTX from DTX-SWCNT-ANXA5.

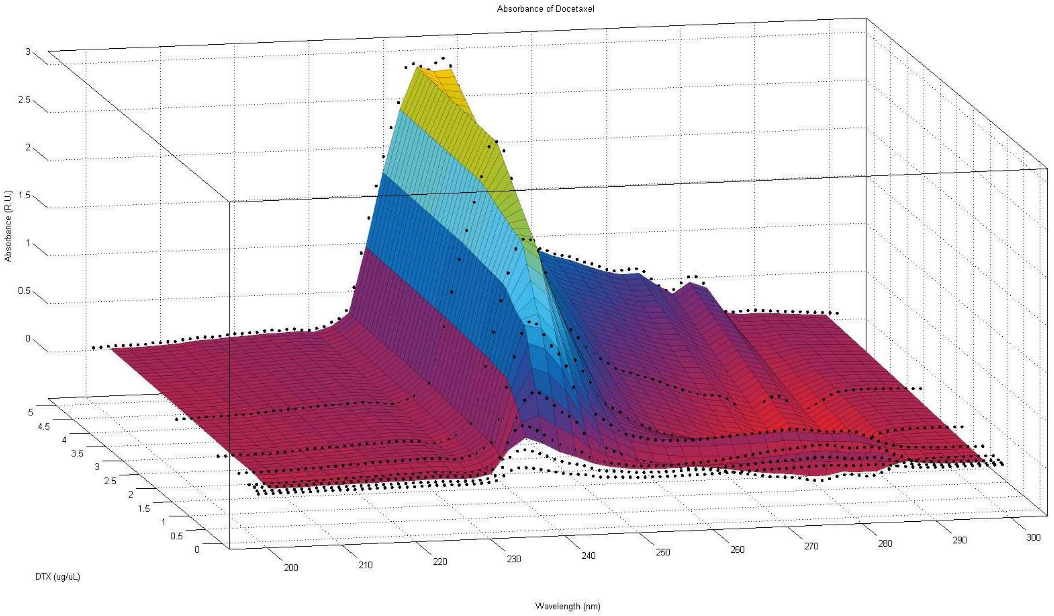

Figure 110: DTXs characteristic UV-absorption peak shifts with increasing concentration

The use of phosphate buffer as an antisolvent (new synthesis) significantly increased DTX: SWCNT loading compared to the use of only EtOH (original synthesis) (Figure 111).

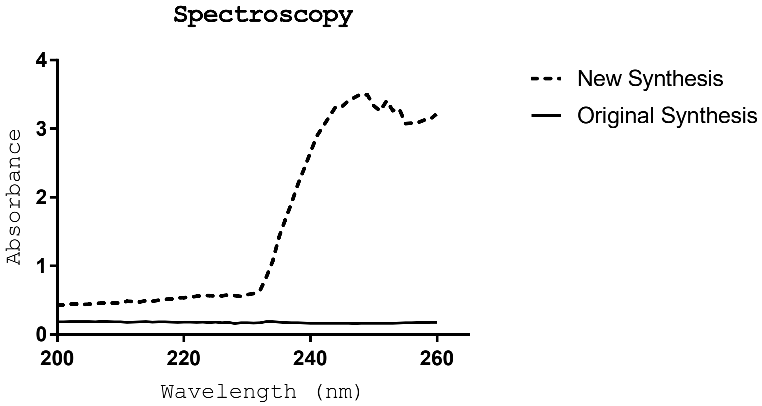

Figure 111: Increased DTX loading observed following methylene chloride extraction of an antisolvent precipitation synthesis. In the original synthesis SWCNTs and DTX were suspended in solution and mixed to encourage association. In the new synthesis, phosphate buffered saline was dropwise added to a suspension of DTX and SWCNT initiating the precipitation of DTX.

The amount of DTX within the SWCNT-DTX conjugate can be quantified using absorbance spectroscopy. Unknown DTX concentrations were determined in the organic phase of a methylene chloride extraction from aqueous standards. Standards were generated by measuring the max absorbance between 200-200 nm and plotting this versus docetaxel concentration (Figure 112).

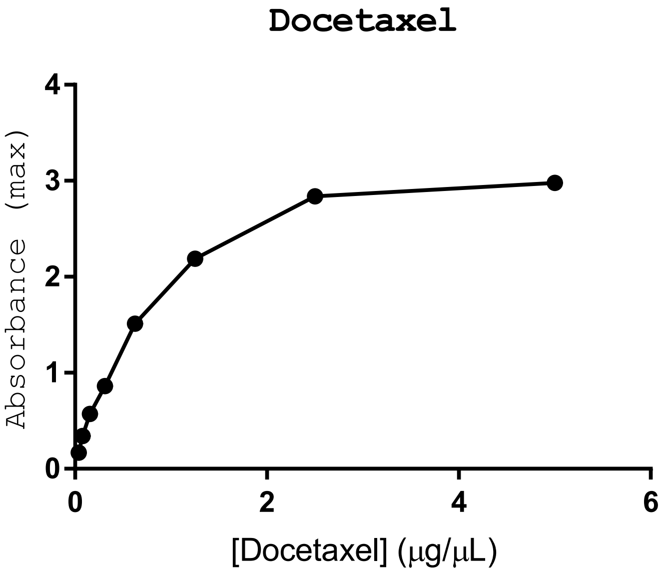

Figure 112: Absorbance standard following methylene chloride extraction.

The degree of DTX loading within the DTX-SWCNT conjugate can be precisely controlled. A methylene chloride extraction of SWCNT-DTX conjugate prepared using different starting concentrations of DTX demonstrates the increasing loading of DTX (Figure 113).

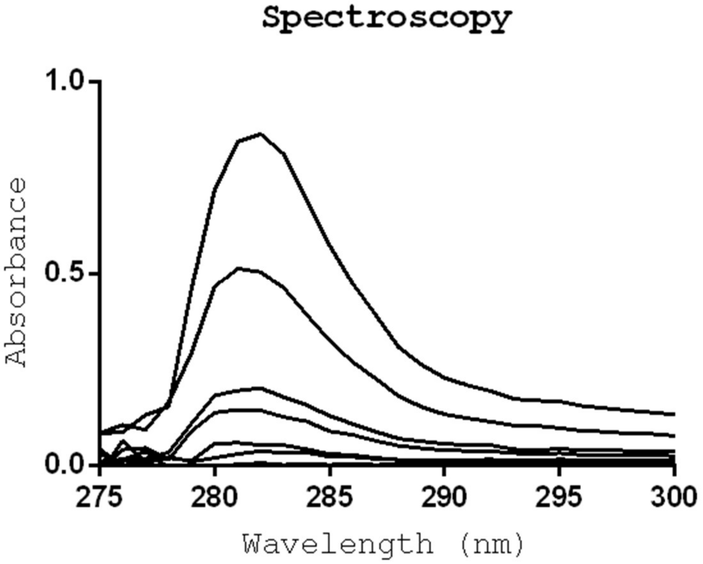

Figure 113: Increasing DTX loading on SWCNT. The absorbance spectra of docetaxel following methylene chloride extractions was assayed after the synthesis of SWCNT-DTX with 2-fold decreasing initial concentrations of DTX. $[DTX]_{starting}$: 4 mg/mL)

Appendix H: Antibacterial Assay

Intracellular Infection

1) Cells will be incubated with NTHi for 2 hours.
    - 10 µL of 1-5 x 109 cfu/ml (OD@600 nm=0.65)
    - This should yield 2 x 105 cfu per well, or about 0.1% uptake
2) Cells will be washed 3 times in PBS to remove excess NTHi
3) All cells will be incubated in 10 ug/L gentamicin for 3 hours.

4) Select samples shall receive excess ANXA5-mCGL (120 nM) and be incubated for 3 h.
5) Wash all wells 3x in dPBS to remove excess ANXA5-mCGL.
6) Mammalian cells will be passaged by trypsin, and whole cells will be lysed by briefly sonicating sample with glass beads.
7) Samples will then be serially diluted in BHI and plated on chocolate agar plates.
8) The number of Bacteria shall be assayed after 36 hours by microscopy.

Antibacterial Activity ANXA5-mCGL

Elaborating on previous work targeting intracellular pathogens (Chapter 1: Antimalrial Fusion Protein) the antibacterial activity of fusion protein (ANXA5-mCGL) was ascertained in an in vitro model of intracellular infection. Mouse derived mesenchymal stem cells were seeded into a 96-well microtiter plate at a density of 5 x 10^5 cell per well and allowed to rest for 24 hours. Cell samples were then inoculated with 10^6 CFU of pathogenic Haemophilus influenzae. Intracellular uptake of bacteria was encouraged by centrifuging samples at 1000 g for 10 minutes at 4 °C. Excess extracellular bacteria were removed by thorough washing with HBSS. Samples were then incubated with 75 µg/mL of cell impermeable gentamicin for 3 hours to destroy any remaining extracellular bacteria. The resulting bacterially infected cells were then used as a model of intracellular infection.

The antibacterial activity of ANXA5-mCGL was then assayed in this model. Cultures were treated with 500 µM of fusion protein or a saline control for 36 hours in antibiotic free medium. After treatment, cells were harvested using 0.25 % trypsin-EDTA and lysed to release bacteria. Bacteria were then plated on chocolate agar plates (Figure 114). Cultures of untreated samples (top, left) were almost immediately overgrown. Treated samples (top, right) plated fewer colonies. Quantitative analysis of CFU following treatment (bottom) revealed that cultures treated with ANXA5-mCGL has significantly fewer viable NTHi colonies ($n \leq 0.05$).

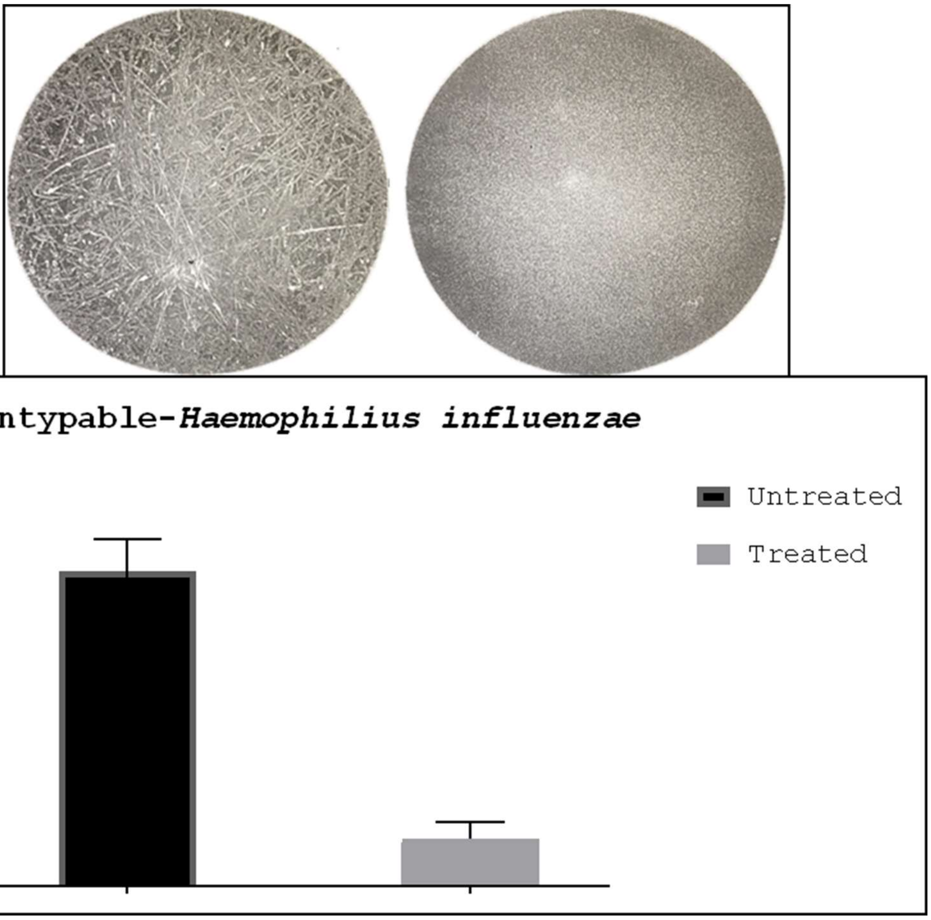

Figure 114: Antibacterial activity of ANXA5-mCGL. Infected cultures of mamillian cells treated with fusion protein plated fewer colonies of bacteria then controls. Data is presented as the mean ± SE (n = 3)